FUNCTIONAL RELEVANCE OF HOMEOSTATIC INTRINSIC PLASTICITY IN NEURONS AND NETWORKS

YANN SWEENEY

Doctor of Philosophy (School of Informatics, University of Edinburgh)
PhD in Computer Science (School of Computer Science and Communication,
KTH Royal Institute of Technology)
2016

Yann Sweeney:
Functional relevance of homeostatic intrinsic
plasticity in neurons and networks
Doctor of Philosophy (School of Informatics, University of Edinburgh)
PhD in Computer Science (School of Computer Science and Communication,
KTH Royal Institute of Technology), 2016

SUPERVISORS:
Matthias Hennig (University of Edinburgh)
Jeanette Hellgren Kotaleski (KTH Royal Institute of Technology)

ENGLISH ABSTRACT

Maintaining the intrinsic excitability of neurons is crucial for stable brain activity. This can be achieved by the homeostatic regulation of membrane ion channel conductances, although it is not well understood how these processes influence broader aspects of neuron and network function. One of the many mechanisms which contribute towards this task is the modulation of potassium channel conductances by activity-dependent nitric oxide signalling. Here, we first investigate this mechanism in a conductance-based neuron model. By fitting the model to experimental data we find that nitric oxide signalling improves synaptic transmission fidelity at high firing rates, but that there is an increase in the metabolic cost of action potentials associated with this improvement. Although the improvement in function had been observed previously in experiment, the metabolic constraint was unknown. This additional constraint provides a plausible explanation for the selective activation of nitric oxide signalling only at high firing rates.

In addition to mediating homeostatic control of intrinsic excitability, nitric oxide can diffuse freely across cell membranes, providing a unique mechanism for neurons to communicate within a network, independent of synaptic connectivity. We next conduct a theoretical investigation of the distinguishing roles of diffusive homeostasis mediated by nitric oxide in comparison with canonical non-diffusive homeostasis in cortical networks. We find that both forms of homeostasis robustly maintain stable activity. However, the resulting networks differ, with diffusive homeostasis maintaining substantial heterogeneity in activity levels of individual neurons, a feature disrupted in networks with non-diffusive homeostasis. This results in networks capable of representing input heterogeneity, and linearly responding over a broader range of inputs than those undergoing non-diffusive homeostasis. We further show that diffusive homeostasis interferes less than non-diffusive homeostasis in the synaptic weight dynamics of networks undergoing Hebbian plasticity. Overall, these results suggest a novel homeostatic mechanism for maintaining stable network activity while simultaneously minimising metabolic cost and conserving network functionality.

SVENSKT ABSTRAKT

Det är viktigt att ha en stabil aktivitetsnivå i hjärnan och ett nödvändigt kriterium för detta är att nervcellernas retbarhet eller excitabilitet upprätthålls. Detta kan ske genom en homeostatisk reglering av konduktansen i de jonkanaler som sitter i cellmembranet i de enskilda nervcellerna. Man vet dock inte vad en sådan homeostas har för generell påverkan på närliggande neuron eller på andra aspekter av nätverkets funktion. En av flera mekanismer som bidrar till homeostas är aktivitetsberoende modulering av kaliumkanaler via kväveoxid signalering. I denna avhandling undersöker vi denna mekanism med hjälp av en konduktansbaserad neuronmodell. Modellen, som vi anpassar till experimentella data, används för att göra prediktioner. Ett exempel på prediktion är att kväveoxidsignaleringen verkar kunna förbättra synapstransmissionen vid hög nätverksaktivitet, dock följer en ökad metabol kostnad med denna förbättring. även om denna funktionella förbättring har observerats tidigare så var de metabola konsekvenserna okända. Detta kan förklara att man ser en selektiv aktivering av kväveoxid endast vid höga aktivitetsnivåer i nätverket.

Förutom att mediera en homeostatisk kontroll av excitabiliteten, diffunderar kväveoxid fritt genom cellmembranen och utgör därmed en unik mekanism för nervceller att påverka varann inom nätverket, oberoende av den synaptiska konnektiviteten. Vi utförde en teoretisk studie av diffusiv homeostas medierad av kväveoxid och jämförde med den mer kanoniska formen av icke-diffusiv homeostas i kortikala nätverk. Vi fann att båda formerna av homeostas kan upprätthålla en stabil aktivitesnivå i nätverket. De resulterande nätverken skiljer sig dock åt på så sätt att diffusiv homeostas bevarar en signifikant heterogenitet vad gäller aktivitetsnivån hos de enskilda nervcellerna, till skillnad från nätverk med en icke-diffusiv homeostas. Diffusiv homeostas resulterar i nätverk som kan representera heterogenitet och därmed förmedla signaler över ett större intervall än de nätverk som har icke-diffusiv homeostas. Vi visar dessutom att diffusiv homeostas interfererar mindre med den synaptiska dynamiken i nätverk med Hebbs plasticitet. Sammantaget tyder dessa resultat på att vi identifierat en ny homeostatisk mekanism som kan upprätthålla en stabil nätverksaktivitet samtidigt som den metaboliska kostnaden minimeras och nätverksfunktionen bevaras.

ACKNOWLEDGEMENTS

First of all, I wish to gratefully thank my supervisors, Matthias Hennig and Jeanette Hellgren Kotaleski, for their wonderful guidance and support throughout this thesis. It was a pleasure to work with such enthusiastic and encouraging scientists.

I would like to thank my experimental collaborators from the lab of Ian Forsythe for the opportunity to work with some real data. Thanks also to organisers of the EuroSPIN PhD programme, particularly Mark van Rossum and Jeanette Hellgren Kotaleski, for making this endeavour possible, and to the funders; the EuroSPIN Erasmus Mundus Programme and the EPSRC Neuroinformatics DTC.

I am very grateful to my family for their constant support, and to Alex for her encouragement and advice. Finally, a big thank you to all my office mates, lunch mates, and pub mates who brightened any dull moments that emerged over the years.

DECLARATION

I declare that this thesis was composed by myself, that the work contained herein is my own except where explicitly stated otherwise in the text, and that this work has not been submitted for any other degree or professional qualification except as specified.

Edinburgh, 2016

Yann Sweeney, 25th May
2016

CONTENTS

ABBREVIATIONS

AHP	Afterhyperolarisation
AIS	Axon initial segment
AP	Action potential
ATP	Adenosine triphosphate
cGMP	Cyclic guanosine monophosphate
EPSC	Excitatory postsynaptic current
HIP	Homeostatic intrinsic plasticity
ISI	Inter-spike interval
LSO	Lateral superior olive
LTD	Long-term depression
LTP	Long-term potentiation
mEPSC	Miniature excitatory postsynaptic current
MNTB	Medial nucleus of the trapezoid body
Na^+/K^+-ATPase	Sodium-potassium adenosine triphosphatase
NO	Nitric oxide
sGC	Soluble guanylyl cyclase
SNR	Signal-to-noise ratio
SPON	Superior paraolivary nucleus
STDP	Spike-timing-dependent plasticity
STG	Stomatogastric ganglion

1

INTRODUCTION

This work will investigate models of homeostatic intrinsic plasticity in single neurons and in networks of neurons. In particular, the interplay between homeostatic constraints and functional capability will be discussed.

1.1 NEURONAL HOMEOSTASIS

The term homeostasis, from the Greek *homœos* (similar) and *stasis* (standing still), was originally coined by Walter Cannon (Cannon, 1926). It describes the ability of a system to maintain a stable internal physiological state (or 'milieu intérieur' (Bernard, 1878)) despite environmental perturbations (Williams et al., 2013). A prototypical example of this concept is the ability of the human body to maintain a relatively constant temperature across a wide range of external temperatures. This is achieved by shivering when the temperature is too low in order to produce heat, and sweating when the temperature is too high in order to lose excess heat.

1.1.1 *The necessity of firing rate homeostasis*

Considering the vastly complex and dynamic range of behaviours exhibited by neurons in the brain, electrical activity remains remarkably stable across many stages of development, environmental stimuli, and brain states. As such, it has long been presumed that the activity of neurons are under some form of homeostatic control (Turrigiano and Nelson, 2004).

Hebbian plasticity, an expression of the doctrine that 'cells that fire together, wire together', has been postulated to form the basis of learning and memory in the brain (Hebb, 1949; Schatz, 1992). In this theory, if the firing of neuron A persistently elicits the firing of neuron B, then a process occurs in which the synapse connecting these two neurons is strengthened, in effect increasing the efficiency of neuron A in causing neuron B to fire. Since this increase in synaptic efficacy would lead to an increase in electrical activity, which in turn would lead to a further increase in synaptic efficacy, theoretical arguments require the existence of a stabilising form of plasticity which could counteract this possibility of runaway excitation caused by Hebbian plasticity (Miller, 1996).

Similar arguments propose that the gain, or excitability, of neurons within a feed-forward network needs to be tightly regulated in order to prevent either saturation of neural firing rates (leading to information loss) or failure to propagate activity through feed-forward structures (see Figure 1.1). These network effects, which may arise due to the failure of homeostatic mechanisms to keep neural activity within a physiologically reasonable level, are hypothesised to be the origin of epileptic seizures (Artinian et al., 2015). However, firing rate homeostasis is not necessary in situations when synchronous spiking may serve a computational role (Nowotny and Huerta, 2003).

There is now a wide range of experimental evidence for multiple and diverse homeostatic mechanisms which regulate neural activity at synaptic, cellular, and network-wide levels (Turrigiano and Nelson, 2004; Turrigiano, 2011). As in the above examples, homeostasis is typically thought to occur either through plasticity of synaptic weights, or through plasticity of intrinsic factors mediating neural excitability (Williams et al., 2013).

1.1.2 *Homeostatic 'set points' and the tradeoff between conflicting constraints*

As will be discussed throughout this thesis, homeostatic mechanisms are typically described in terms of a 'set point' to which the distance must be minimised; for neurons this 'set point' is typically thought to be a defined target firing rate. This is implicitly based on the assumption that neurons operate optimally at a certain average firing rate, where changes in input are best represented by corresponding changes in output. For example, in Figure 1.1, the optimal regime for feedforward propagation of information is for neurons to have a gain of 1, and so their I-O curves could be homeostatically maintained at this level (Turrigiano and Nelson, 2004). This assumes however that there is a single constraint which determines the action of a homeostatic mechanism, whereas in reality it is likely that the action of regulatory mechanisms are dependent on multiple constraints. For conflicting constraints, there must necessarily be a tradeoff between them.

Specifically, here we investigate the hypothesis that in addition to optimal functionality, the metabolic cost of neural activity may be an important further constraint. Mammalian brains consume around 20% of the metabolic resources available to the organism, so it is likely that selection for metabolic efficacy takes place (Attwell and Laughlin, 2001; Hasenstaub et al., 2010). In this case, there may be a tradeoff between a neuron's ability to maintain a desired level of activity, and the rate of depletion of metabolic resources. We aim to investigate homeostatic mechanisms which can mediate a tradeoff between multiple constraints, as such diverging from the conventional view of a unique homeostatic 'set point'. This will be investigated at the single neuron level, where it is possible to evaluate metabolic cost of neural activity rather precisely.

A second factor that will be investigated is the relationship between optimal function and the physiology of homeostatic set-points. As explained, often a certain average firing rate is viewed as optimal for neurons as it enables them to respond well to a range of inputs without response saturation. However, in terms of neural coding this may not be optimal. For instance, Stemmler and Koch (1999) proposed a model of ion channel regulation where homeostatic control not only changed the average activity of a neuron, but also the gain (the slope of its I-O curve) to best match the variance in the input of a neuron. More generally, the relationship between optimal function and homeostatic set-points is at best complex, and currently not well understood. In networks this issue becomes even more complicated as the overall network state, which cannot be directly sensed by local homeostatic mechanisms in neurons, has direct functional implications.

Before discussing these tradeoffs in detail we will provide a brief overview of known homeostatic mechanisms from experimental studies, and attempts to describe these mechanisms theoretically. For commentary on the concept of 'set points' and their relevance when describing regulatory physiological processes, see (Sterling and Eyer, 1988; Berntson and Cacioppo, 2007; O'Leary and Wyllie, 2011; Sterling, 2012).

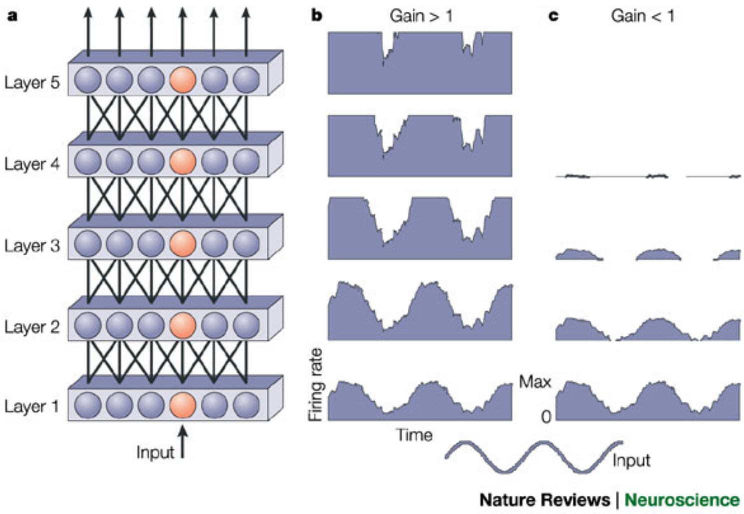

Figure 1.1: The propagation of activity in a feedforward network (a). If neurons in each layer represent the previous layers' output but with a slightly higher firing rate, there is a saturation of firing rates in the higher layers and information about the original input is lost (b). Conversely, if neurons in each layer represent the previous layers' output but with a slightly lower firing then by the final layer there will be no neural activity at all (c). Diagram from Turrigiano and Nelson (2004).

1.1.3 *Synaptic scaling*

One of the first mechanisms implicated in homeostatic control of neural activity is synaptic scaling, originally described by Turrigiano et al. (1998). Long-term blockade of neural activity in cortical cultures was found to cause an increase in the amplitudes of miniature excitatory postsynaptic currents (mEPSCs), which are the currents from individual incoming synapses that contribute to excitation in the postsynaptic neuron. This increase gradually restored firing rates to physiological levels over a 48 hour period. The changes in amplitude were multiplicative in nature, meaning that the total synaptic drive to a neuron is increased while preserving the relative strength between synapses. An equal and opposite effect occurred when neural activity is increased by blocking inhibition (Turrigiano et al., 1998). Synaptic scaling has also been observed *in vivo* in response to prolonged visual deprivation (Desai et al., 2002; Chandrasekaran et al., 2007).

1.1.4 *Synaptic metaplasticity*

Another form of homeostasis at the synaptic level is synaptic metaplasticity. Theoretical models of Hebbian plasticity such as the Bienenstock, Cooper and Munro (BCM) model generally have a threshold which determines whether postsynaptic activity leads to either long-term depression (LTD) or long-term potentiation (LTP) of synaptic weights (Bienenstock et al., 1982). If there are low levels of postsynaptic activity while synaptic inputs are active, these synapses would undergo LTD. However, if postsynaptic activity is above a certain threshold, these synapses would undergo LTP. This threshold can be regulated such that neither LTP or LTD is overly dominant, therefore providing a homeostatic mechanism which prevents runaway potentiation or depression of synaptic inputs. The modulation, or plasticity, of this threshold is known as synaptic metaplasticity (Mockett et al., 2002), and the form proposed by BCM theory was later observed in experiments (Kirkwood et al., 1996). Other forms of synaptic metaplasticity have been observed, which are not homeostatic in their effect. Huang et al. (1992) demonstrated experimentally that inducing LTP transiently raised the threshold for subsequent induction of LTP, while Mockett et al. (2002) demonstrated that stimulus protocols which initially induce LTP can later induce LTD due to a reduction in the threshold for LTD.

1.1.5 *Homeostatic plasticity of intrinsic excitability*

As well as regulating neural activity through forms of synaptic plasticity, there are mechanisms which mediate homeostatic control of activity by regulating the intrinsic excitability of neurons. This is known as homeostatic intrinsic plasticity (HIP) (Desai et al., 1999; Williams et al., 2013). Turrigiano et al. (1994) first demonstrated this effect by isolating single neurons from electrical activity in a culture, and observing that neurons changed from tonic firing to burst firing in response to current injections after 3-4 days of isolation. Desai et al. (1999) also demonstrated this effect by blocking synaptic electrical activity in cultured neurons, and observing that neurons were more excitable in their response to current injections after 48 hours of this deprivation. This effect was later confirmed to be bidirectional; chronic overstimulation of neurons leads to a decrease in intrinsic excitability, showing that it is homeostatic in nature (Brickley et al., 2001).

Plasticity of intrinsic excitability has also been observed in response to the induction of Hebbian synaptic plasticity, although in this case the direction of change in excitability is the same as that of the synapses; postsynaptic neurons whose synapses undergo LTP exhibit an increase in intrinsic excitability, whereas LTD causes a decrease in intrinsic excitability (Daoudal et al., 2002; Debanne and Poo, 2010) . Theoretical studies have proposed that this form of intrinsic plasticity, which is anti-homeostatic, can act synergistically with Hebbian synaptic plasticity, by providing a neural memory trace, or by improving the ability of an associative network to perform memory recall (Janowitz and Van Rossum, 2006; Savin et al., 2014).

1.1.6 *Regulation of ion channel conductances*

Plasticity of intrinsic excitability is often achieved by regulation of membrane ion channel conductances. In the experiments described above which first characterised HIP, the modulation of voltage-dependent sodium currents and voltage-dependent potassium currents were implicated in the change in intrinsic excitability (Turrigiano et al., 1994; Desai et al., 1999; Brickley et al., 2001). Broadly speaking, intrinsic excitability is increased by the upregulation of sodium currents, and decreased by the upregulation of potassium currents.

Seminal work by the lab of Eve Marder has extensively characterised the flexibility with which modulation of ion channel conductances can maintain desired properties of neural activity. Despite highly variable levels of ion channel expression, which are undergoing constant turnover with timescales of minutes to weeks, neurons in the lobster stomatogastric ganglion (STG) can maintain specific bursting firing patterns which are crucial for maintaining a pyloric rhythm that controls muscle movements in the stomach. (Golowasch et al., 2002; Marder and Goaillard, 2006; Selverston, 2008). Similarly, Swensen and Bean (2005) found that burst firing in cultured Purkinje neurons was conserved following chronic or acute blockade of sodium currents by a compensatory change in potassium currents. This body of work demonstrates that homeostatic control of neural activity extends not only to maintaining firing rates within a physiological range, but also to maintaining a wide range of desired neural activity.

Although there exists a rich repertoire of neuromodulatory pathways which regulate ion channel conductances (Williams et al., 2013; Turrigiano, 2011), we will discuss below the nitric oxide signalling pathway as an example, which will form the basis of models of HIP throughout this thesis.

1.1.7 *Modulation of potassium conductances by nitric oxide signalling*

Nitric oxide is a neurotransmitter produced endogenously in the brain, which has been implicated in a variety of neural functions including learning and memory, control of cell fate, and vasodilation (Son et al., 1996; Blaise et al., 2005; Nikonenko et al., 2013; Tamagnini et al., 2013; Lourenço et al., 2014). The source of nitric oxide synthesis is a protein called nitric oxide synthase (NOS), which comes in three isoforms; inducible (iNOS), endothelial (eNOS), and neuronal (nNOS) (Garthwaite, 2008). Nitric oxide is synthesised intracellularly by nNOS, in neurons which express this protein (Garthwaite, 2008). This nNOS is activated by Ca^{2+} influx through synaptic NMDA receptors, therefore linking sustained excitatory synaptic activity with NO synthesis (Garthwaite, 2008; Steinert et al., 2008).

Experiments conducted in the lab of Ian Forsythe at the University of Leicester have investigated the effect of NO signalling in the medial nucleus of the trapezoid body (MNTB), finding that it modulates numerous ion channel conductances (Steinert et al., 2008, 2011; Tozer et al., 2012). The MNTB is a region in the auditory brainstem which serves as an ideal model system for studying pre- and post-synaptic transmission, and will be discussed in more detail in chapter 2. Soluble guanylyl cyclase (sGC) is a receptor which is rapidly activated by NO signalling, causing it to generate cyclic guanosine monophosphate (cGMP) (Garthwaite, 2008). This intracellular NO-cGMP signalling pathway alters the phosphorylation levels of potassium ion channels in the MNTB, in effect increasing their conductances (Steinert et al., 2008). As will be discussed further in chapter 2, this increase in potassium currents enables MNTB neurons to maintain spiking frequencies of up to 800 Hz, although it also reduces neural excitability. In this sense, NO modulation can be thought of as a form of HIP, as it decreases the intrinsic excitability of a neuron in response to prolonged synaptic stimulation.

1.1.8 *Regulating excitability through axon initial segment properties*

Although the modulation of ion channel conductances is the most studied mechanism implicated in the regulation of intrinsic excitability, there are other mechanisms which also play a role (Turrigiano, 2011). Notably, both the distance of the axon initial segment (AIS) from the soma, and the length of the AIS, can change in response to perturbations in activity (Grubb and Burrone, 2010; Kuba et al., 2010). These modifications homeostatically regulate the intrinsic excitability of that neuron, as the AIS is primarily responsible for action potential generation (Bender and Trussell, 2012).

1.2 COMPUTATIONAL MODELS OF NEURONAL HOMEOSTASIS

The vast majority of theoretical work on modelling neuronal homeostasis is conducted using two approaches; conductance-based biophysical neuron models, or more abstract integrate-and-fire point neuron models. Both of these approaches are discussed below.

1.2.1 *Hodgkin-Huxley style biophysical models*

Perhaps the most famous model in neuroscience is the Hodgkin-Huxley model of action potential generation in the giant axon of the squid (Hodgkin and Huxley, 1952) [1]. The neuron membrane is represented as a capacitance, with current flow due to the charging of this capacitor, and the flow of ions through ion channels. These different current contributions are illustrated in the circuit diagram in Figure 1.2. Ion channels are represented by a resistor in this diagram, with their conductance inversely proportional to the resistance. Voltage-dependence of ion channels, such as the sodium (g_{Na}) and potassium (g_K) channels in this case, are represented in the diagram by arrows, and their conductances can be expressed by various activation

---

[1] Note that this (somewhat misleadingly) does not refer to the axon of the giant squid, which the sourcing of in 1952 would have been quite a feat in itself.

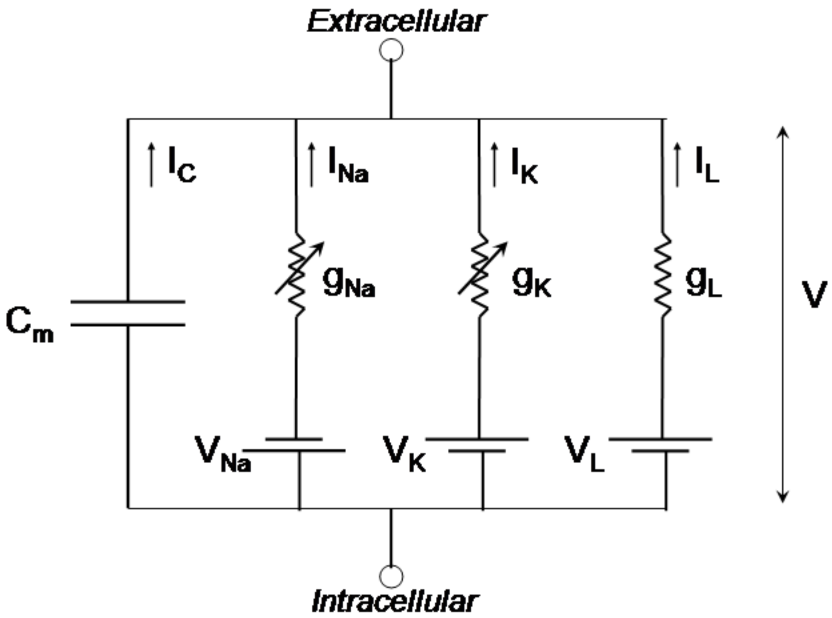

Figure 1.2: A circuit diagram of a simple conductance-based model neuron. Voltage-gated ion channels are represented by conductances (g), and electrochemical gradients represented by voltage sources (V). Diagram from Skinner (2006).

and inactivation gating variables. For example, the sodium channel conductance is given by $g_{Na} = \bar{g}_{Na} m^3 h$, where $\bar{g}_{Na}$ is the maximal conductance, and m and h are variables representing the sodium channel activation and inactivation respectively (Hille et al., 2001; Skinner, 2006). The evolution of activation and inactivation variables are determined by solving a set of ordinary differential equations. We will discuss these equations in more detail in chapter 2. The electrochemical gradients which determine the flow of ions between the intracellular and extracellular volumes are represented by voltage sources (V_{Na}, V_K and V_L in Figure 1.2). These conductances are ion species-specific in the case of g_{Na} and g_K, but not so in the case of g_L.

The simplest conductance-based model represent a neuron as a single isopotential compartment. More detailed models can be comprised of multiple compartments which may represent the neuron morphology. The propagation of electrical signals along these compartments can be solved using cable theory, the application of which was developed by Rall in the late 1950's (Rall, 1959; Niebur, 2008; Rall, 2009). Most multicompartmental models are now solved using specialised simulation packages, such as the Neuron simulator (Carnevale and Hines, 2006).

1.2.2 *Modelling activity-dependent regulation of ion channels*

HIP can be implemented in a conductance-based model by introducing a mechanism which regulates the maximal conductance of the relevant ion channels. Since homeostasis is essentially a form of negative feedback control, any implementation of this requires an electrical activity sensor so that conductances may be regulated in an activity-dependent manner. Intracellular calcium concentration is usually assumed to be a putative activity sensor, as calcium influx occurs during electrical activity, and it is known to mediate many changes in intrinsic neural properties (Alkon, 1984; LeMasson et al., 1993). The role of intracellular calcium concentration in mediating HIP was later confirmed in experiments on the lobster STG (Turrigiano et al., 1994; Golowasch et al., 1999a). LeMasson et al. (1993) developed the first model of HIP in a neuron by setting a target value for intracellular calcium concentration. Maximal conductances in the model were modulated according to time-averaged calcium concentrations. Slow firing, tonic firing, or burst firing could be achieved in the model through setting different targets calcium targets, and it was observed that the same target behaviour could be achieved by models with highly variable underlying conductances (Golowasch et al., 2002; Marder and Taylor, 2011). More recently, O'Leary et al. (2013, 2014) have generalised this framework by developing a model which couples a cell-intrinsic activity readout with ion channel expression rates, finding that such a model explains the correlations in ion channel conductances previously observed in neurons (Schulz et al., 2006; Tobin et al., 2009).

1.2.3 *Integrate-and-fire neuron models*

The integrate-and-fire neuron model was first conceived by Lapique in 1907 (Lapicque, 1907; Abbott, 1999). The most simple model takes the form of an RC circuit in parallel, in which the cell membrane is represented by the capacitor (Figure 1.3). In these types of models, the action potential dynamics aren't specifically computed as in Hodgkin-Huxley style models, but are inserted 'by hand' whenever the membrane potential exceeds a specified threshold. Following a threshold event, the membrane potential is set to a specified 'reset voltage', often after a set time, which is referred to as the refractory period (Burkitt, 2006). There is now a large family of integrate-

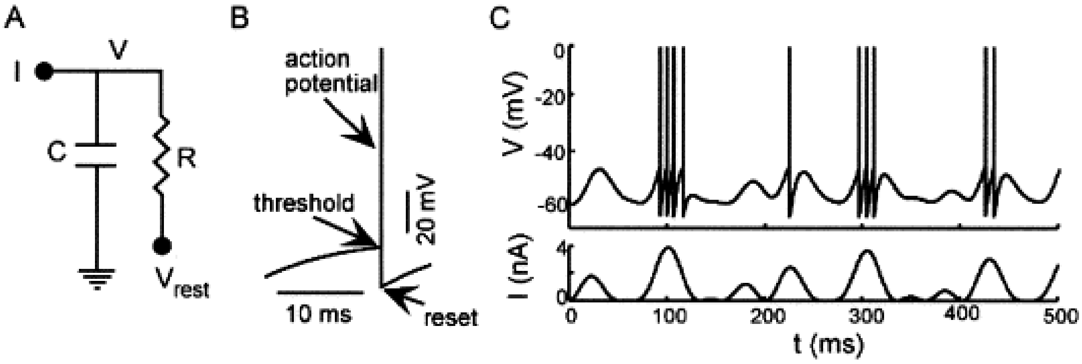

Figure 1.3: A circuit diagram of a simple integrate-and-fire model neuron (A). An action potential occurs when the the membrane voltage passes a threshold, and is reset after a refractory period (B). Diagram from Abbott (1999).

and-fire style models, which have additional features such as spike frequency adaptation, spike bursting and subthreshold oscillations (Fourcaud-Trocmé et al., 2003; Izhikevich et al., 2003; Gerstner and Brette, 2009). Izhikevich (2004) provides a review of the advantages and disadvantages of these different neuron models.

HIP can be implemented in an integrate-and-fire model by a variety of methods. Similarly to the implementation of HIP in Hodgkin-Huxley style models, an activity sensor based on intracellular calcium concentration can be achieved by modelling calcium influx at each threshold event (LeMasson et al., 1993; Giugliano et al., 1999). Intrinsic excitability can be directly regulated by modulating the firing threshold, or by introducing a bias current which may be modulated according to recent activity (Remme and Wadman, 2012; Harnack et al., 2015). The implementation of HIP in an integrate-and-fire neuron model is discussed in chapter 3.

1.2.4 *Homeostasis in networks of model neurons*

Following their implementation of HIP in individual conductance-based neuron models, (Golowasch et al., 1999b) extended their work to investigate the effect of HIP in networks of these neurons, based on the well-characterised circuitry of the lobster STG. They found that regulation of conductances in individual neurons can give rise to stable pyloric rhythms across the circuit (Golowasch et al., 1999b; Günay and Prinz, 2010).

A key advantage of integrate-and-fire neuron models is that they are both computationally efficient to simulate and analytically tractable, making them useful in investigations of the dynamics of networks of neurons (Izhikevich, 2004; Burkitt, 2006). Implementations of homeostasis in these networks of spiking neurons have typically focused on its role in counteracting the destabilising effects of Hebbian plasticity (Remme and Wadman, 2012; Zenke et al., 2013; Harnack et al., 2015). However, recent experimental and theoretical studies have demonstrated the importance of homeostatic mechanisms in regulating more complex measures of network activity, such as the balance of excitatory and inhibitory synaptic currents, or the degree of criticality in network dynamics (Sun et al., 2010; Tetzlaff et al., 2010; Vogels et al., 2011; Naudé et al., 2013). Moreover, studies on both networks of rate-based or spiking neurons demonstrated the synergistic role of distinct types of homeostasis in optimising the performance of networks, in this case when both synaptic scaling and HIP are active (Triesch, 2007; Naudé et al., 2013; Zenke et al., 2015). We will discuss the implementation and outcome of various forms of HIP in recurrent networks in detail in chapter 3.

1.3 HYPOTHESES AND OUTLINE

Although we have mainly discussed how electrical activity is homeostatically regulated so that it remains within a physiologically reasonable range, the principle of homeostatic control can be extended to encompass alternative objectives which neural mechanisms may attempt to optimise. In the MNTB, NO signalling has been shown to improve the fidelity of high frequency post-synaptic transmission. However, there does not seem to be any functional advantages associated with the low levels of NO signalling observed in the basal state, so it is not clear why this mechanism is only activated after prolonged synaptic activity. Many theoretical and experimental studies have demonstrated the importance of the metabolic cost of neural processing as a constraint which is minimised in the brain (Niven et al., 2007; Hasenstaub et al., 2010; Kostal et al., 2013). This raises the possibility that there may be an increased metabolic cost associated with NO signalling, and hence a tradeoff between metabolic efficiency and post-synaptic transmission fidelity. Therefore, in chapter 2 we investigate the hypothesis that NO signalling has a specific role in optimising metabolic aspects of neural signalling.

In chapter 3 and chapter 4 we consider the impact that homeostasis at the single neuron level has on network dynamics. Theoretical studies have demonstrated how activity-dependent regulation of conductances can optimise information content in single neurons and in networks (Stemmler and Koch, 1999; Naudé et al., 2013). Similarly, modelling studies have demonstrated that a broad distribution of firing rates within a population of neurons can optimise the stimulus information encoded by this population (Padmanabhan and Urban, 2010; Tripathy et al., 2013). Recent experiments investigating the response of neuronal cultures to perturbations indicate that network-wide properties such as the distribution of firing rates are under homeostatic control, while the activity of individual neurons within a network may not be so strictly regulated (Slomowitz et al., 2015; Panas et al., 2015).

It is not clear how individual neurons whose firing rates are regulated by a homeostatic mechanism can function within a network in a way which maintains these network-wide properties, without the homeostatic mechanism having access to some form of readout of network-wide statistics. Similarly, although some forms of HIP may act so as to optimise function at the single-neuron level, this would not necessarily guarantee optimal function at a network level (Stemmler and Koch, 1999) without incorporating some measure of network-wide activity. In chapter 3 we investigate the hypothesis that HIP mediated by a diffusive signal, which extends across many neurons, can achieve the observed heterogeneity across a population of neurons while maintaining the flexibility of individual neurons. We further investigate whether this mechanism can improve the function of the network.

Finally, usually different forms of plasticity are active simultaneously during spontaneous or evoked activity (Watt and Desai, 2010; Turrigiano, 2011). However, if homeostasis is successful in ensuring that neurons are always maintained at their target firing rate, then it is likely that it would interfere with the ability of Hebbian plasticity to successfully learn synaptic weights in response to inputs which evoke differing firing rates. We hypothesise that HIP mediated by a diffusive signal may reduce such interference with Hebbian plasticity compared with HIP mediated by a non-diffusive signal. The interaction of these different forms of HIP and Hebbian plasticity will be discussed in chapter 4.

2

MODELLING ACTIVITY-DEPENDENT REGULATION AND METABOLIC EFFICIENCY IN THE MNTB

> *Like the stops on an organ, the diversity of available channels is used to give timbre to the functions played by excitable cells.*
>
> Bertil Hille 2001

CHAPTER SUMMARY

Neurons in the auditory brainstem transmit signals which are used for sound localisation and gap detection. These relay neurons, located in the Medial Nucleus of the Trapezoid Body (MNTB), must sustain precise firing at high frequencies, a physiologically demanding task. Previous studies have identified a low-threshold potassium channel, K_v2, which enables fast action potential repolarisation and is present in the MNTB (Steinert et al., 2011). K_v2 is potentiated by nitric oxide (NO) signalling following sustained activity, improving transmission fidelity at high frequencies. The existence of a signalling pathway to increase K_v2 conductances only at high frequencies is puzzling, as there are no evident disadvantages of this channel also being active at low frequencies.

We investigate the effect of K_v2 modulation in a biophysical model of the MNTB by inferring ion channel conductances during the naive state and the NO-activated state from intracellular recordings. We find that the metabolic efficiency of action potential generation is significantly reduced by the presence of K_v2, when compared with other potassium channels which dominate in the naive state. This is due to the low activation threshold of K_v2, which leads to potassium currents that follow sodium currents more closely during an action potential. This increases the current overlap, often used as a proxy for energy efficiency (Hallermann et al., 2012). This energy constraint is a plausible explanation for the selective activation of K_v2 by nitric oxide signalling at high frequencies.

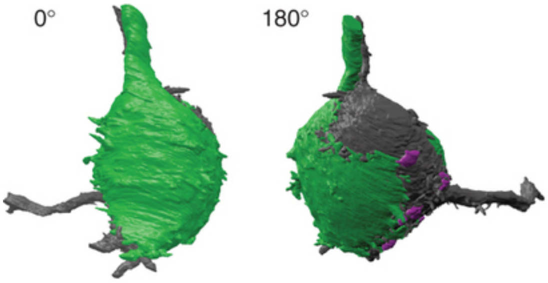

Figure 2.1: Reconstruction of a calyx of Held (green) enveloping a single principal neuron of the MNTB (dark grey), using electron microscopy. Image obtained by Xiao et al. (2013) using scanning electron microscopy.

The model predicts that if ATP production is blocked, action potential generation would fail earlier in neurons with higher K_v2 conductances. We briefly discuss experiments currently underway which attempt to directly test this hypothesis under varying levels of NO activation.

2.1 INTRODUCTION

The medial nucleus of the trapezoid body (MNTB) is a region in the auditory brainstem which contains some of the largest known synapses in the mammalian brain, the calyces of Held (Borst and Soria van Hoeve, 2012). Each calyx targets a single principal neuron of the MNTB (Figure 2.1), and generates atypically large EPSPs (Hennig et al., 2008). Although there are discrepancies between *in vitro* and *in vivo* recordings (Lorteije et al., 2009; Mc Laughlin et al., 2008), a single presynaptic EPSP is sufficient to elicit a postsynaptic action potential (AP), thus forming an extremely reliable relay system (Borst and Soria van Hoeve, 2012).

This relay system receives input predominantly from contralateral globular bushy cells, which in turn receive their input directly from the auditory nerve. Principal neurons of the MNTB send inhibitory projections to auditory nuclei such as the lateral superior olive (LSO) and superior paraolivary nucleus (SPON). Figure 2.2 illustrates this circuitry. Due to short synaptic delays at the calyx of Held, these inputs can be used to detect timing differences between the contralateral and ipsilateral ear. These timing difference can be used by LSO neurons to localise sound sources (Grothe et al., 2010). Similarly, timing information of projections to the SPON from the MNTB can be used to detect gaps in auditory stimuli (Kopp-Scheinpflug et al., 2011b). Projections to

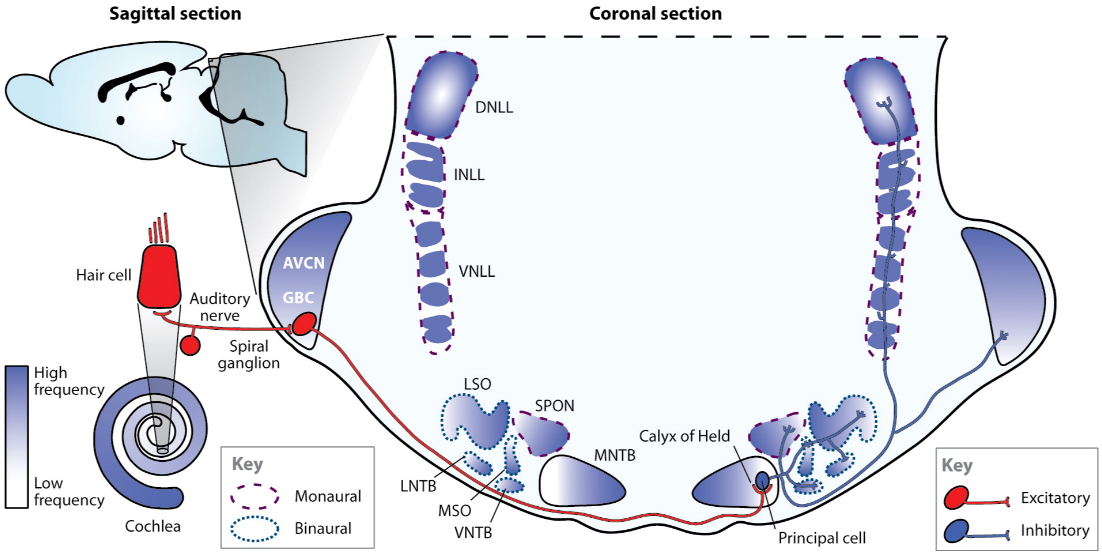

Borst JGG, van Hoeve JS. 2012.
Annu. Rev. Physiol. 74:199–224

Figure 2.2: Connections to and from principal neurons of the MNTB. The MNTB receives large glutamatergic inputs from contralateral auditory nerve via the GBC, and sends inhibitory projections predominantly to the LSO, SPON and MSO. These projections are arranged from low-frequency to high-frequency, forming a tonotopic axis (illustrated by a light-dark gradient inside the nuclei). Figure from Borst and Soria van Hoeve (2012).

and from the MNTB are tonotopic, meaning that inputs representing low-frequency to high-frequency auditory stimuli are arranged along a tonotopic axis (shown by the light-dark gradients in Figure 2.2). Spontaneous firing rates vary along the tonotopic axis, and gradients in potassium channel conductances have also been observed along this axis (Kopp-Scheinpflug et al., 2008; Brew and Forsythe, 2005).

2.1.1 *Voltage-gated ion channels in the MNTB*

The large size of the calyx of Held and its postsynaptic principal MNTB neurons make it a popular model system for electrophysiologists, particularly in studying synaptic transmission. It is accessible *in vitro* and *in vivo*, and paired pre- and post-synaptic intracellular recordings are relatively achievable (Kopp-Scheinpflug et al., 2008; Borst and Soria van Hoeve, 2012). The ion channel and membrane properties of the terminal are therefore well-characterised (Johnston et al., 2010). The MNTB has a particularly rich repertoire of voltage-gated potassium channels, which ensure that firing rates are maintained over long periods and at frequencies of up to 800 Hz (Wu and Kelly, 1993; Brew and Forsythe, 1995; Johnston et al., 2010). K_v1 channels provide precise control of AP firing threshold and timing, due to their low activation voltage and their location at the axon initial segment (AIS) (Dodson et al., 2002; Gittelman and Tempel, 2006). K_v3 channels are active only during an AP, and their rapid kinetics contribute to a fast repolarisation, ensuring that APs are narrow and that high-frequency firing is maintained (Wang et al., 1998). K_v2 channels are also crucial for maintaining high-frequency firing. Their relatively slow inactivation means that they contribute to lengthening the hyperpolarisation phase after an AP, known as the after-hyperpolarisation (AHP). This lowers the inter-spike membrane potential, which in turn leads to faster recovery from Na_v inactivation after a spike, due to the voltage-dependence of Na_v inactivation. Johnston et al. (2008) have previously demonstrated how this enables MNTB neurons with high K_v2 conductances to maintain high-frequency AP firing.

2.1.2 *Experiments investigating NO modulation in the MNTB*

As introduced briefly in chapter 1, nitric oxide (NO) is a neurotransmitter which is synthesised following prolonged synaptic stimulation, and has been shown to modulate ion channel currents in the MNTB (Steinert et al., 2008, 2011; Tozer et al., 2012). These experiments were performed in mouse brain slices, and the conductances of different K+ channels were measured in the presence or absence of NO signalling, either by evoking NO signalling through glutamatergic synaptic signalling, or by using an NO donor. The importance of NO signalling was further demonstrated using nNOS knockout mice, and the contribution of different K+ channels were investigate using a variety of specific pharmacological channel blockers or by using Kv2 knockout mice.

It was shown that the intracellular NO-cGMP signalling pathway alters the phosphorylation levels of K_v2 and K_v3 ion channels in the MNTB, in effect modulating their conductances (Steinert et al., 2008). While NO signalling decreases K_v3 currents by $\sim 50\,\%$, it dramatically increases K_v2 current by a factor of ~ 3, leading to a transition in the dominant repolarising potassium channel from K_v3 to K_v2. This transition from K_v3-mediated to K_v2-mediated AP repolarisation enables MNTB neurons

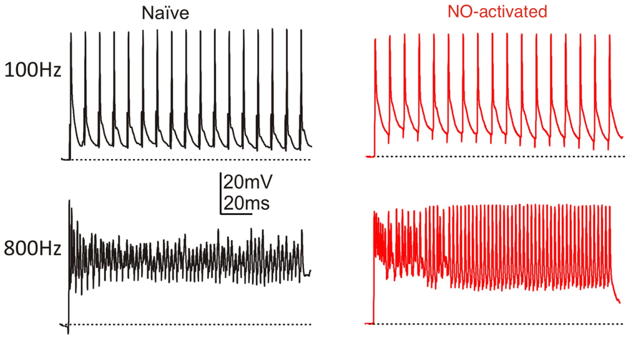

Figure 2.3: MNTB membrane potential traces, showing APs in response to synaptic stimulation at 100 Hz (upper) or 800 Hz (lower) in the naive state (left) and in the NO-activated state (right). Figure from (Steinert et al., 2011).

to sustain AP transmission at frequencies of up to 800 Hz in the NO-activated state, compared with 100 Hz in the naive state (i. e. in the control condition, before NO signalling is triggered by sustained synaptic activity) (Steinert et al., 2011). This is shown in Figure 2.3. The increase in K_V2 current also reduces neural excitability. In this sense, NO modulation can be thought of as a form of homeostatic intrinsic plasticity (HIP), as it decreases the intrinsic excitability of a neuron in response to prolonged electrical activity.

The timescale of NO modulation is in the order of 10-30 minutes (Steinert et al., 2011). This is quite fast compared with other forms of HIP, which occur over multiple days (Desai et al., 1999; O'Leary, 2008). The reason for this difference in timescales is that NO modulation directly phosphorylates potassium channels, while other regulatory mechanisms rely on transcription or trafficking of channels, which require signalling at the cell nucleus (Song et al., 2005a; Mori et al., 1993; Vacher and Trimmer, 2012). In addition to modulating potassium channels, NO signalling has been shown to decrease Na_V currents and increase Ca_V currents in the MNTB (Steinert et al., 2008; Tozer et al., 2012). The latter effect may mostly have a role in regulating presynaptic and intracellular signalling as opposed to action potential generation, as calcium currents are generally quite small compared with other channels (Tozer et al., 2012). NO signalling also affects presynaptic processes through retrograde transmission; the diffusion of NO across the synaptic cleft to the calyx of Held. Synaptic vesicle release is upregulated following NO synthesis, enabling sustained high-frequency synaptic transmission (Eguchi et al., 2012).

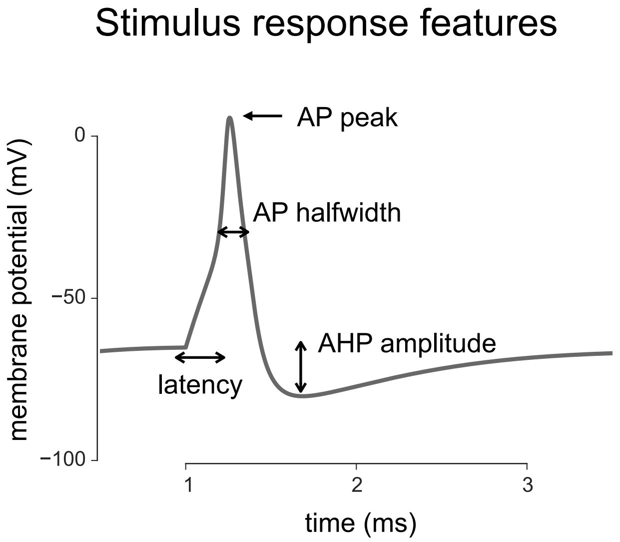

Figure 2.4: Features of an action potential evoked by a stimulus.

2.2 MODELLING THE MNTB

2.2.1 *Biophysical Modelling*

A single neuron model is implemented using the NEURON simulation environment, in conjunction with the pyNEURON interpreter (Carnevale and Hines, 2006). Backward Euler integration (Carnevale and Hines, 2006, Chapter 4) is used with a timestep of 0.0025 ms unless otherwise stated.

A single-compartmental of the MNTB originally developed by Wang et al. (1998); Macica et al. (2003), and later modified by Johnston et al. (2008) is used as the starting point to replicate the observed effects of NO on the electrical properties of an MNTB neuron. This model is composed of a soma containing a voltage-gated sodium channel (Na_v), a hyperpolarisation-activated current (I_h), a leak current (I_L), and three different voltage-gated potassium channels (K_v1,K_v2,K_v3). K_v4 channels, or A-type K^+ currents, are also present in the original model, but are ignored here as they are not important for action potential repolarisation due to their slow kinetics and relatively small conductances (Steinert et al., 2011). A brief description of each channel's electrical properties along with the source of their original implementation is presented in Table 2.1, and the equations used to calculate the total current through the

CHANNEL	DESCRIPTION	SOURCE
Na_v	Inactivating sodium current	Rothman and Manis
I_h	Hyperpolarisation-activated current	Kopp-Scheinpflug et al.
I_L	Non-specific leak current	Johnston et al.
K_v1	Low-voltage activated delayed rectifier	Wang et al.
K_v2	Medium-voltage activated, slow delayed rectifier	Johnston et al.
K_v3	High-voltage activated, fast delayed rectifier	Wang et al.

Table 2.1: Ion channel properties

membrane and the current for each channel are provided below. These equations are solved by NEURON using numerical integration.

$$I_{Total} = iNa_v + iK_v1 + iK_v2 + iK_v3 + I_h + I_L \tag{2.1}$$

$$iNa_v = g_{Na_v}\left(0.97m^3h + 0.025m^3p + 0.005m^3\right)(v - E_{Na}) \tag{2.2}$$

$$m_\infty = \left(1 + e^{\frac{-(v+38)}{7}}\right)^{-1} \tag{2.3}$$

$$h_\infty = p_\infty = \left(1 + e^{\frac{(v+55.4)}{6.3}}\right)^{-1} \tag{2.4}$$

$$m_\tau = \frac{5}{5e^{\frac{v+60}{18}} + 36e^{\frac{-(v+60)}{25}}} + 0.01 \tag{2.5}$$

$$h_\tau = \frac{50}{7e^{\frac{v+60}{11}} + 10e^{\frac{-(v+60)}{25}}} + 0.5 \tag{2.6}$$

$$p_\tau = \frac{50}{7e^{\frac{v+60}{11}} + 10e^{\frac{-(v+60)}{25}}} + 50 \tag{2.7}$$

$$iK_v1 = g_{K_v1}\left(w^3 z\right) \mathrm{GHK}\left(v, [K^+]_{in}, [K^+]_{ex}\right) \tag{2.8}$$

$$w_\infty = \left(1 + e^{\frac{-(v+53)}{6.7}}\right)^{-\frac{1}{3}} \tag{2.9}$$

$$z_\infty = 0.6 + \frac{0.4}{1 + e^{\frac{v+71}{7}}} \tag{2.10}$$

$$w_\tau = \frac{15}{e^{\frac{v+60}{15}} + 18e^{\frac{-(v+60)}{15}}} + 0.5 \tag{2.11}$$

$$z_\tau = \frac{1000}{e^{\frac{v+60}{20}} + e^{\frac{-(v+60)}{8}}} + 50 \tag{2.12}$$

$$iK_v2 = g_{K_v1}\left(wz\right) \mathrm{GHK}\left(v, [K^+]_{in}, [K^+]_{ex}\right) \tag{2.13}$$

$$w_\infty = \left(1 + e^{\frac{-(v+8.99)}{12.3}}\right)^{-1} \tag{2.14}$$

$$z_\infty = \left(1 + e^{\frac{-v-43.9}{-8.29}}\right)^{-1} \tag{2.15}$$

$$w_\tau = \frac{800}{49e^{\frac{v+60.4}{18.2}} + 102e^{\frac{-(v-18.9)}{67}}} + 0.183 \tag{2.16}$$

$$z_\tau = \frac{446}{1.54e^{\frac{v-10.8}{85.3}} + 7.55e^{\frac{-(v+48.4)}{5.63}}} + 334 \tag{2.17}$$

$$iK_v3 = g_{K_v1}\left(n^4\right) \mathrm{GHK}\left(v, [K^+]_{in}, [K^+]_{ex}\right) \tag{2.18}$$

$$n_\infty = \left(1 + e^{\frac{-(v+20)}{9}}\right)^{-0.25} \tag{2.19}$$

$$n_\tau = \frac{50}{11e^{\frac{v+60}{24}} + 21e^{\frac{-(v+60)}{23}}} + 0.1 \tag{2.20}$$

$$I_h = g_h\left(u\right)\left(v - E_h\right) \tag{2.21}$$

$$u_\infty = \left(1 + e^{\frac{v+101}{11}}\right)^{-1} \tag{2.22}$$

$$u_\tau = \frac{10000}{235.55e^{0.0782(\nu+23.76)} + 0.33e^{-0.0614(v+23.76)}} + 154.57 \tag{2.23}$$

$$I_L = g_L \mathrm{GHK}\left(v, [K^+]_{in}, [K^+]_{ex}\right) \tag{2.24}$$

The activation constants for the channels described above; m, h, p, w, z, n and u, are unitless, while their respective time constants (τ_m, etc.) have units of ms. The GHK function in the equations above represent the Goldman-Hodgkin-Katz flux equation, which describe the flux of an ion species across a membrane of a given potential and for given ionic concentrations on either side of the membrane. It is given below, in which F is the Faraday constant, R is the ideal gas constant and T is the absolute temperature (Hille et al., 2001).

$$\mathrm{GHK}\left(v, [K^+]_{in}, [K^+]_{ex}\right) = P\frac{v\,F}{RT}\frac{[K^+]_{in} - [K^+]_{ex}\exp\left(-vF/RT\right)}{1 - \exp\left(-vF/RT\right)} \tag{2.25}$$

The units of conductances for currents which are given by the GHK equation are expressed in the Gaussian unit system (cms^{-1}), while Ohmic currents are expressed in Siemens. Since currents given by the GHK equation are preferable to Ohmic currents in situations where there are extreme gradients between the inner and outer ion concentrations, it would have been sufficient to use only Ohmic currents in this model (Hille et al., 2001). However, as some of the ion channel models which we used were originally described through the GHK equation and fit to experimental data in this form, we have continued with this description (Wang et al., 1998; Johnston et al., 2010). A further consequence of using ion channel models which were inherited from these previous studies is that there seem to be a number of superfluous terms in the equations, which could easily be ignored within the scope of this chapter. Candidates include the $0.005m^3$ term in Equation 2.2 , and the constants of 0.183 and $.01$ in Equation 2.5 and Equation 2.16 respectively. However, as we did not have access to the data used to perform the original fits, we decided to keep these equations in their current form. An improvement to this model could be made by reducing these equations to include only terms that matter in determining the dynamics.

The relative contribution of each of these channels to the stimulus response properties of a neuron are illustrated in Figure 2.5. Following a short current pulse (1500 pA for 0.25 ms), the model neuron typically fires an AP. The AP peak is primarily de-

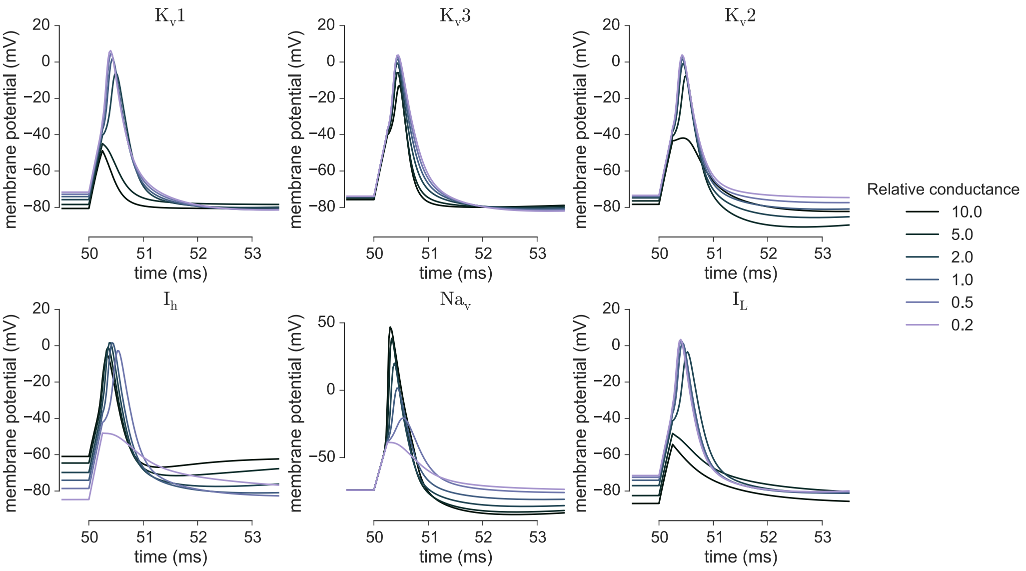

Figure 2.5: Relative contribution of ion channels to electrical properties. Stimulus is a square current pulse of 1500 pA for 0.25 ms, starting at 50 ms. Each conductance is scaled by a range of factors, where the initial value is that used by Johnston et al. (2008).

termined by the Na_v conductance, although increasing K_v1, K_v2 or K_v3 conductances decreases it slightly (see Figure 2.4 for an illustration of the different features of an AP) . The AP threshold is raised by increasing K_v1 conductance. Increasing K_v3 or K_v2 conductances decreases the AP half-width. Additionally, and importantly, K_v2 increases the amplitude of the AHP due to its slow inactivation time constant. Finally, I_h and I_L do not significantly influence AP dynamics, although they determine the resting membrane potential: I_h raises it and I_L lowers it.

2.2.2 *Model neuron morphology and ion channel localisation*

While the original neuron model described in Johnston et al. (2008) is a single-compartment model, Johnston et al. (2010) have identified, using immunohistochemistry experiments, the subcellular localisation of K_v1, K_v2 and Na_v channels in the axon initial segment (AIS). Na_v channels in the AIS play a crucial role in AP initiation, particularly in ensuring a rapid AP onset (McCormick et al., 2007; Kole and Stuart, 2012, although Baranauskas et al. (2010) argue that additional factors are required to explain the speed of AP onset). Since we are investigating the effects of NO modulation on AP dynamics, we have extended the original model to include these differences.

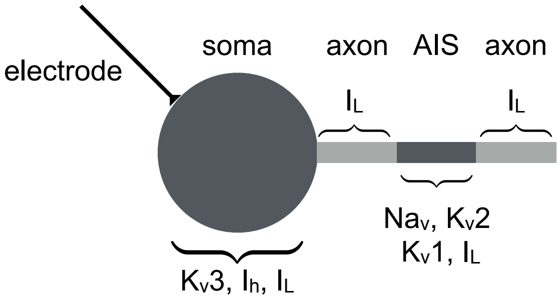

Figure 2.6: Morphology and ion channel location of the AIS neuron model

The morphology and subcellular localisation of ion channels in the multicompartmental model is illustrated in Figure 2.6, and the electrical and biophysical properties of each section are shown in Table 2.2. We have included a section of axon containing only a leak current between the soma and AIS, since Grubb and Burrone (2010) have shown that the AIS location is flexible, and can move distally along the axon in response to prolonged spiking activity. The effect of moving ion channels to the AIS from the soma in the model is shown in Figure 2.7. The channels which have been moved to the AIS have their conductance densities from the original model scaled by the ratio of the soma to AIS surface area in order to conserve the original conductance value. The phase plot of the rate of change of the membrane potential as the membrane potential varies is plotted, showing that a model with Na_v located in the AIS leads to a more rapid AP onset than when it is located in the soma. The maximum slope of the phase plot can be used as a measure of how rapid AP onset is, and is $31.1\,\mathrm{ms}^{-1}$ when the appropriate channels are in AIS, compared with $18.9\,\mathrm{ms}^{-1}$ when these channels are in the soma. The former value is comparable with a value of $28\,\mathrm{ms}^{-1}$ obtained from experimental recordings of cortical pyramidal cells (Yu et al., 2008). Note that the while stimulus currents used in Figure 2.7 may seem large for most neurons, but they are not particularly large for the MNTB principal neuron, as EPSCs from the Calyx of Held can exceed 10 nA (von Gersdorff and Borst, 2002).

Although the majority of Na_v channels are located in the AIS, and Leo et al. (2008) have found no evidence of somatic Na_v expression, in contrast with previous work by Leao et al. (2006), we investigate the effect of having a ratio of Na_v conductance in the soma as well as the AIS. Varying this ratio does not have a significant effect on the AP shape (Figure 2.8), although locating more Na_v in the AIS does increase the

SECTION	LENGTH	DIAMETER	SPECIFIC CAPACITANCE	RESISTIVITY
Soma	17.84 µm	17.84 µm	$1\,\mu\mathrm{F\,cm}^{-2}$	35.4 Ωcm
Axon (proximal)	10 µm	2 µm	$1\,\mu\mathrm{F\,cm}^{-2}$	35.4 Ωcm
AIS	5 µm	2 µm	$1\,\mu\mathrm{F\,cm}^{-2}$	35.4 Ωcm
Axon (distal)	10 µm	2 µm	$1\,\mu\mathrm{F\,cm}^{-2}$	35.4 Ωcm

Table 2.2: Biophysical properties of the multicompartmental MNTB model.

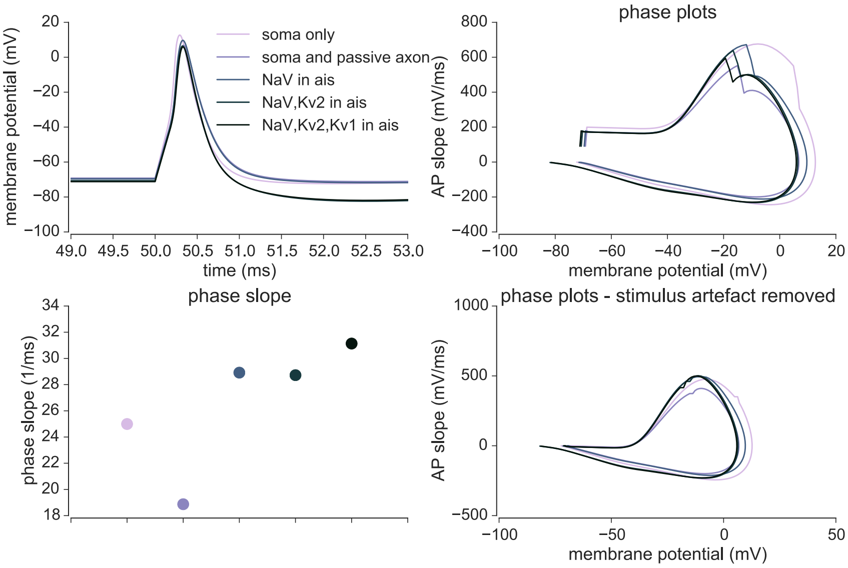

Figure 2.7: Effect of adding axon and AIS to the model, and locating ion channels in the AIS. Stimulus is a square current pulse of 2000 pA for 0.25 ms, starting at 50 ms. The membrane potential over time is shown (top left), as well as a phase plot (top right), which shows the evolution of the rate of change of the membrane potential as the membrane potential varies. The maximum slope of the phase plot is plotted for the different models (bottom left, colours match legend in top left). The square current pulse stimulus leaves an artefact in the phase plot diagram, which is subtracted for ease of visual inspection (bottom right).

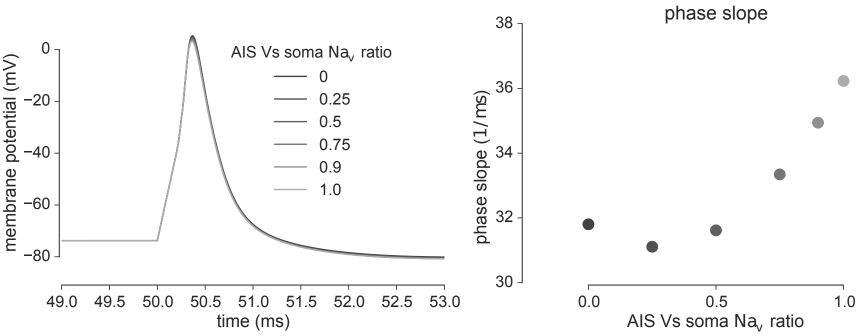

Figure 2.8: Varying the ratio of Na$_v$ in the AIS versus the soma does not significantly affect AP shape, although higher ratios accelerate AP onset. Stimulus is a square current pulse of 2000 pA for 0.25 ms, starting at 50 ms.

speed of AP onset as expected from previous studies (McCormick et al., 2007), and as just shown above.

2.3 FITTING CONDUCTANCES TO DATA

2.3.1 *Membrane voltage fits*

We will now attempt to fit the conductances of existing ion channel models so as to match the behaviour of our MNTB model to experimental observations. The ion channel models are taken from the studies shown in Table 2.1, and their parameters will remain unchanged expect for their conductances. A reasonable initial approach to fitting ion channel conductances with electrophysiological recordings is to minimise the difference between the voltage traces of the model and the data. This difference is usually measured as the root-mean-square (RMS) difference between the two time series (Van Geit et al., 2008). This approach, however, is not very fruitful. Since there are many interdependent parameters to vary, overfitting is encountered, resulting in multiple solutions which lead to similar voltage traces but with wildly different conductance values. The solutions often results in unphysiological values for the ion channel conductances. Additionally, the nature of the fitting algorithm means that a low error can be achieved by fitting certain sections of the voltage traces very well (such as the AP), while the error might be quite high in other section (such as the AHP). Such an example is illustrated in Figure 2.9.

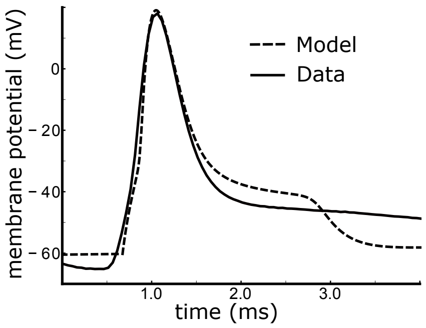

Figure 2.9: An attempt at fitting conductances of the multicompartmental MNTB neuron model to recorded membrane potential traces, obtained by Steinert et al. (2011). The downhill simplex algorithm implemented in SciPy was used (Wright, 1996; Van Der Walt et al., 2011).

It is not desirable to have a perfect fit to a particular recording, but rather a range of parameters which are in a realistic physiological range and can capture many or most of the observed stimulus response properties. The high variability encountered across neurons, and even within the same neuron across a recording, substantiates this objective (Golowasch et al., 2002; Marder and Taylor, 2011).

2.3.2 *Voltage clamp fits*

Voltage clamp is an experimental technique used to quantify the electrical currents of a neuron at a certain voltage (Moore, 2007). The membrane potential of a neuron is clamped at a specific value by injecting a constantly updated current, which is controlled by negative feedback in order to maintain the specified voltage. In this way current can then be recorded across a range of voltages. Steinert et al. (2011) performed voltage clamp recordings of MNTB neurons under naive and NO-activated conditions, and while applying specific channel blockers. By applying TEA, which blocks K_V3, or r-stromatoxin-1, which blocks K_V2 channels, we can tease apart the contributions of each ion channel to the total K^+ current of a neuron in both the naive and NO-activated state. Figure 2.10E shows that K_V3 contributes significantly to the total K^+ current in the naive state, as it is reduced by adding TEA. In the NO-activated state, TEA no longer has a large effect on the total K^+ current, but applying r-stromatoxin-1 blocks a significant portion, implying that K_V2 is now the dominant repolarising channel (Figure 2.10F). By setting each K^+ conductance in the

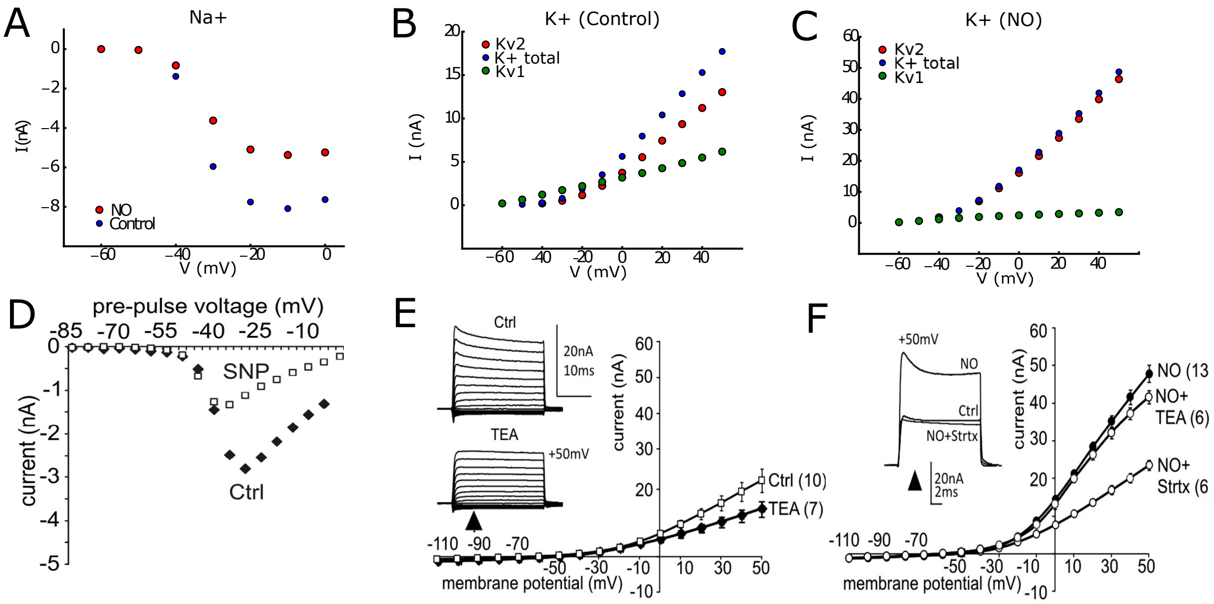

Figure 2.10: IV curves obtained by a voltage clamp in steps of 5 mV for the multicompartmental MNTB model (A-C). The voltage was measured at the steady state, after 100 ms. (D-F) are figures from the experimental study, presented as a comparison of (A-C) respectively. D is from Figure S3 of Steinert et al. (2008). E and F are from Figures 3A and 3D of (Steinert et al., 2011) respectively.

MNTB model so that the current contribution roughly matches those observed from the voltage clamp (Figure 2.10B,C), we can obtain estimates of the conductance for each K^+ channel in both the naive and NO-activated state (see Table 2.3). These estimates can then be used to define a physiologically realistic range of values over which we may explore during fitting.

Steinert et al. (2008) found that NO also suppresses Na_v channels, as shown in IV curves before and after an NO donor (SNP) is added (Figure 2.10D, roughly matched by the MNTB model in Figure 2.10A by reducing Na_v conductance). Similar IV curves of Na_v currents were obtained by Johnston et al. (2008, with a peak value of 6.4 nA) and by Leão et al. (2005, with a peak value of 9.6 nA). From this data we can also define physiologically realistic range of Na_v conductances to explore during parameter fitting.

2.3.3 *Multi-objective optimisation*

Now that we have defined a range of reasonable conductances for the MNTB model, we can attempt to fit model parameters to both the naive and NO-activated states observed in Steinert et al. (2011). Since we wish to capture a wide range of changes in response properties, it is suitable to use multi-objective optimisation. Instead of defining a single error function to be minimised by a fitting algorithm (such as the voltage trace error between the model and data), we define a set of target features which we want our model to exhibit. In this way we can constrain a large, complex set of parameters without overfitting to a particular error function. Druckmann et al. (2007) provide a thorough discussion of the advantages of this approach over the more conventional approach of fitting to voltage traces. Bahl et al. (2012) use a multi-objective optimisation method, although in this case the objectives are multiple voltage traces under different conditions. Hay et al. (2011) use a similar approach to the one outlined here and in Druckmann et al. (2007), in which the AP half-width, AP peak, AHP amplitude, and first spike latency are used as objectives.

The features we wish our model to capture are [1]:

1. **AP peak**

   The maximum absolute value of the membrane potential during an AP.

   The mean AP peak decreases from $4\,\mathrm{mV}$ in the naive state to $-2\,\mathrm{mV}$ in the NO-activated state.

2. **AP half-width**

   The full-width at half-maximum of an action potential, where the half-maximum is defined as the midpoint of the resting membrane potential immediately before the start of the stimulus, and the peak membrane potential during the AP.

   The AP peak half-width decreases from $0.4\,\mathrm{ms}$ in the naive state to $0.3\,\mathrm{ms}$ in the NO-activated state.

3. **AP threshold**

   The minimum current required to evoke an AP during a $100\,\mathrm{ms}$ square current pulse. Individual current steps are injected starting at $0\,\mathrm{pA}$ and increasing in steps of $25\,\mathrm{pA}$ to $600\,\mathrm{pA}$. An evoked AP occurs if the peak voltage during the current pulse occurs at a sufficiently sharp local maximum. This is more reliable than simply defining an absolute voltage threshold over which it is determined that an AP is evoked, as the conductances of ion channels can significantly affect the range of voltages during an AP.

---

[1] See Figure 2.4 for illustration of AP features

The AP threshold increases from 200 pA in the naive state to 400 pA in the NO-activated state.

4. **Transmission ratio**

   This is defined as the ratio of EPSPs which evoke a postsynaptic AP, compared with those that fail to evoke an AP. Single EPSPs are injected as a homogeneous Poisson process. A minimum refractory period is enforced by removing all EPSPs which follow a preceding EPSP after less than 1 ms, as all excitatory EPSPs to individual MNTB neurons generally come from the same calyceal synapse (Borst and Soria van Hoeve, 2012). Noise is also introduced into the model neuron as an injected current which takes the form of an Ornstein-Uhlenbeck process (Longtin, 2010), with a mean of 10 pA, variance of 10 pA, and correlation time of 2 mS. An example of the procedure for obtaining the transmission ratio is shown in Figure 2.11.

   Transmission ratios during a 100 Hz train of evoked synaptic activity with Poisson-distributed ISIs is low in the naive state (0.55) and higher in the NO-activated state (0.85). Since our model tends to have lower transmission ratios than in the data, we will attempt to fit our model to the relative change in transmission ratio across the naive and NO-activated state instead of their absolute value in each state. This corresponds to 0.25 in the naive state and 0.4 in the NO-activated state. Alternatively, some noise could have been introduced in the model in order to reduce the transmission ratio to match those observed in experiments.

5. **Single-spiking**

   MNTB neurons typically fire a single AP in response to an EPSP or current pulse (Borst and Soria van Hoeve, 2012; Steinert et al., 2011). For this reason we exclude regions of parameter space containing neurons that respond to a stimulus with bursts of spikes or with no spike at all.

These features are chosen because their values in naive and NO-activated conditions are well characterised in the original experiments by Steinert et al. (2011), and because they are sensitive to the relevant ion channel conductances in the MNTB model. The target feature values were either stated in Steinert et al. (2011) or extracted from their data using the same procedure as that used for the MNTB model.

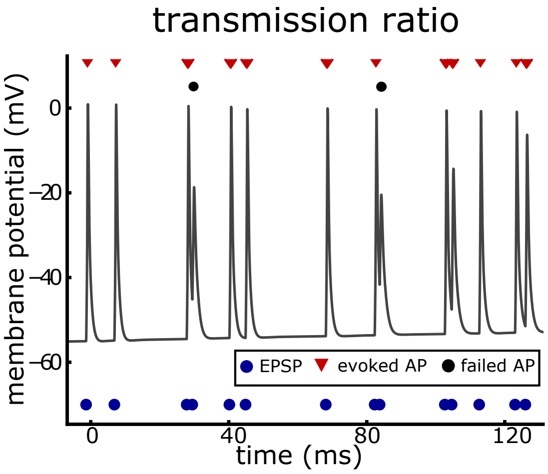

Figure 2.11: Procedure used to obtain the transmission ratio of the MNTB model. The transmission ratio is defined as the fraction of EPSPs (blue circles) which lead to an evoked AP (red triangle), as opposed to a failed AP (black circle).

CHANNEL	MINIMUM	MAXIMUM	RESOLUTION
$g_{\mathrm{Na_v}}$	250 nS	370 nS	25 nS
$g_{\mathrm{K_v2}}$	$0.0 \times 10^{-3}\,\mathrm{cms}^{-1}$	$1.2 \times 10^{-3}\,\mathrm{cms}^{-1}$	$0.1 \times 10^{-3}\,\mathrm{cms}^{-1}$
$g_{\mathrm{K_v3}}$	$0.5 \times 10^{-5}\,\mathrm{cms}^{-1}$	$2.0 \times 10^{-5}\,\mathrm{cms}^{-1}$	$0.25 \times 10^{-5}\,\mathrm{cms}^{-1}$

Table 2.3: Parameter ranges for conductances in brute force sweep.

2.3.4 *Brute force parameter sweep*

Once the extracted features and their targets are defined, we can can choose a fitting algorithm which attempts to minimise the combined error of these features. We will initially perform a brute force approach. That is, we simulate a set of models which span the entire range of possible parameter combinations at a given resolution. This approach has previously been used by Prinz et al. (2003) to characterise the behaviour of a single compartment model of lobster stomatogastric ganglion neurons, containing 8 different ion channels. The parameter space we characterise using this method is shown in Table 2.3. This is the subspace of the conductance range identified through the voltage clamp experiments that lead to single-spiking neurons. Note that the units for potassium conductances, cms^{-1}, are expressed in the Gaussian unit system, as this was their original formulation in the channel models from Wang et al. (1998); Johnston et al. (2010).

2.4 SIMULATING NO MODULATION

Before we characterise the entire range of parameters, we will first attempt to simulate the effect of NO by modulating ion channel conductances in the same manner that NO has been shown to by Steinert et al. (2011) (That is; increasing K_v2, and decreasing K_v3 and Na_v). This is to test whether our model is in principle detailed enough to capture the effects of NO modulation which we are interested in. The initial conductances in the model, which represent the naive state, are: $g_{K_v2} = 1.0 \times 10^{-3}\,\mathrm{cms}^{-1}$, $g_{K_v3} = 5.0 \times 10^{-5}\,\mathrm{cms}^{-1}$, $g_{Na_v} = 250\,\mathrm{nS}$. Their NO-activated values are $g_{K_v2} = 5.0 \times 10^{-3}\,\mathrm{cms}^{-1}$, $g_{K_v3} = 3.0 \times 10^{-5}\,\mathrm{cms}^{-1}$, $g_{Na_v} = 200\,\mathrm{nS}$. Note that changes in conductance are not necessarily proportional to changes in the observed current active during an AP.

2.4.1 *Effect of NO modulation on AP shape*

Figure 2.12 shows the effect of simulating NO modulation in a model MNTB neuron. As expected from Figure 2.5, increasing g_{K_v2} decreases the AP half-width. However, this effect is partially counteracted by the decrease in g_{K_v3} which also occurs through NO modulation. Increasing g_{K_v2} decreases the AP peak, which is again partially counteracted by decreasing g_{K_v3}. Decreasing g_{Na_v} causes the AP peak to decrease further. Note that the initial membrane potential was the same as that used in experiments, in order to facilitate comparison. As such, after the AP the membrane potential goes towards its resting potential, which is lower than the initial membrane potential. Also of note is that increasing g_{K_v2} causes a large increase in the AHP depth, whereas modulating other conductances has little effect on the AHP. This is an important feature of NO modulation, and has been shown to contribute to the ability of MNTB neurons to sustain high-frequency transmission (Johnston et al., 2008; Steinert et al., 2011).

The effects of varying each conductance on the AP shape are robust across our defined range of parameters, as shown in Figure 2.13. Varying g_{K_v3} has a relatively small effect on AP shape across the defined range compared with varying g_{K_v2} and g_{Na_v}.

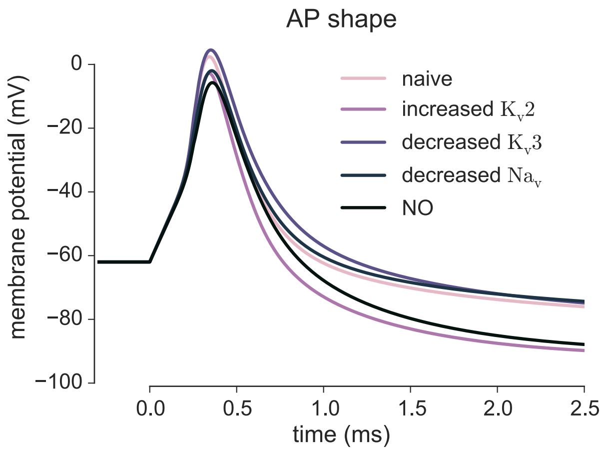

Figure 2.12: The effect on AP shape of simulating NO modulation. Stimulus is a square current pulse of 1500 pA for 0.25 ms, starting at 0 ms. The naive and NO-activated states are shown, as well as the effect of modulating each conductance individually from the naive to the NO-activated state while keeping the rest fixed. This is done for illustrative purposes.

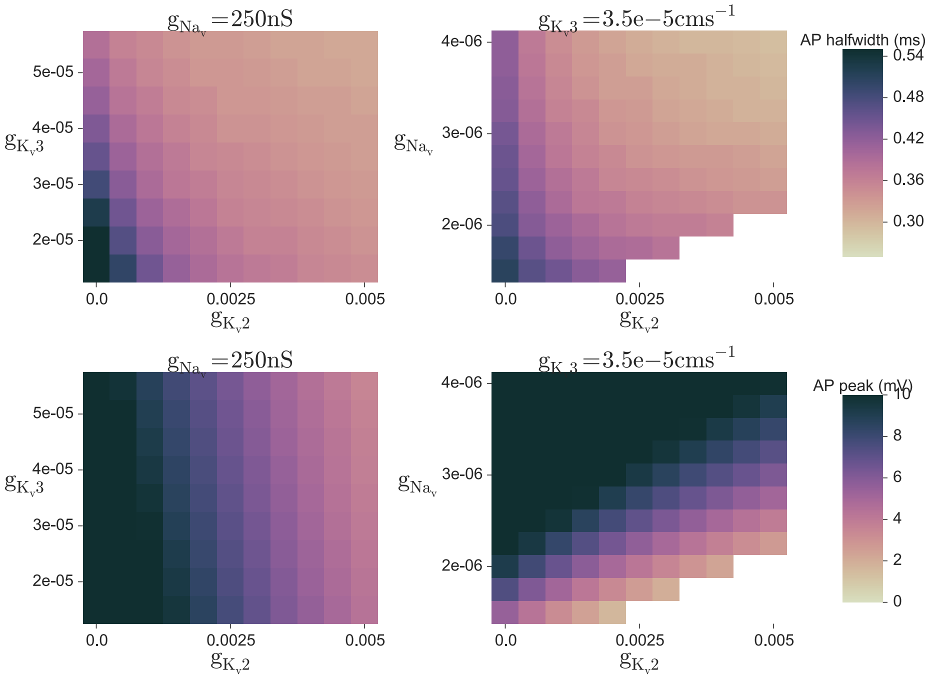

Figure 2.13: AP halfwidth (top row) and AP peak (bottom row) across the entire range of conductances, as either g_{K_v3} is varied against g_{K_v2} (left column), or g_{Na_v} is varied against g_{K_v2} (right column). Representative values of g_{Na_v} or g_{K_v3} are fixed as the remaining conductances are varied while generating the respective heatmaps. Areas filled in white correspond to conductance values which do not fulfill the single-spiking objective (either by not spiking or by spiking multiple times).

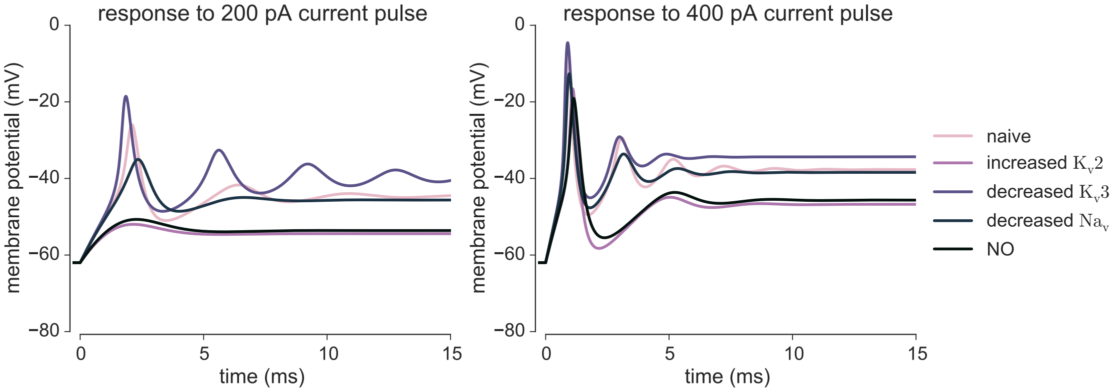

Figure 2.14: The effect on AP threshold of simulating NO modulation. Stimulus is a square current pulse of 200 pA (left) or 400 pA (right) for 15 ms, starting at 0 ms. The naive and NO-activated states are shown, as well as the effect of modulating each conductance individually from the naive to the NO-activated state while keeping the rest fixed. This is done for illustrative purposes.

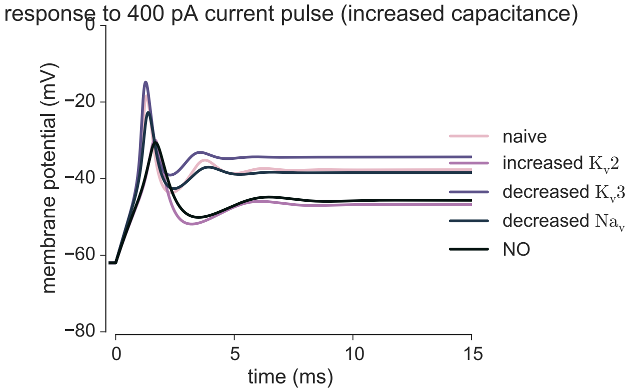

Figure 2.15: Increasing membrane capacitance removes oscillatory behaviour. Stimulus is a square current pulse of 400 pA for 15 ms, starting at 0 ms.

2.4.2 *Effect of NO on AP threshold*

The effect of simulating the change from the naive to the NO-activated state also increases the AP threshold during a current pulse, as expected from experimental observations by Steinert et al. (2011), and shown in Figure 2.14. In this case, both increasing g_{K_v2} and decreasing g_{Na_v} cause an increase in the AP threshold, while decreasing g_{K_v3} causes a decrease in the AP threshold.

The oscillatory behaviour observed after the AP in some cases can be reduced by increasing the membrane capacitance in the model, from 1 to 1.4 $\mu F\,cm^{-2}$ (Figure 2.15). The effects of varying the membrane capacitance is further discussed later in this chapter, when fitting the model to individual neurons.

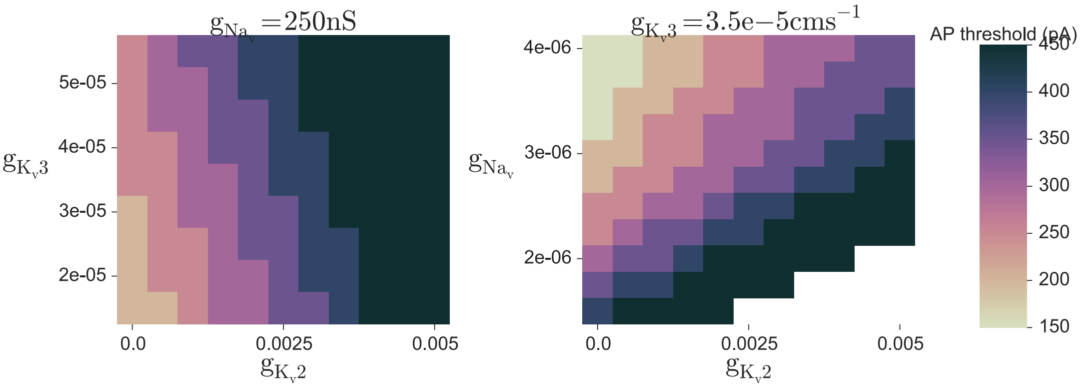

Figure 2.16: AP threshold across the entire range of conductances, as either g_{K_v3} is varied against g_{K_v2} (left), or g_{Na_v} is varied against g_{K_v2} (right). Representative values of g_{Na_v} or g_{K_v3} are fixed as the remaining conductances are varied while generating the respective heatmaps. Areas filled in white correspond to conductance values which do not not fulfill the single-spiking objective (either by not spiking or by spiking multiple times).

The effects of varying each conductance on the AP threshold are relatively robust across our defined range of parameters, as shown in Figure 2.16, although not as smoothly varying as the AP halfwidth and peak.

2.4.3 *Effect of NO on transmission ratio*

Figure 2.17 shows the transmission ratio across the entire range of conductances. The transmission ratio is highest when g_{K_v2}, g_{K_v3}, and g_{Na_v} are relatively large, although the ratio depends more strongly on g_{K_v2} than the other conductances.

The transmission ratio is the most problematic measure used, as pre- and post-synaptic variability and state-dependence which cannot be fully captured by our model will clearly have an impact on the likelihood that an EPSP will elicit an AP in the post-synaptic neuron at a given instance. For this reason we will attempt to fit our model to the relative change in transmission ratio across the naive and NO-activated state instead of their absolute value in each state. An alternative approach would be to introduce additional variability to our model which could be tuned to give a closer fit to the absolute values.

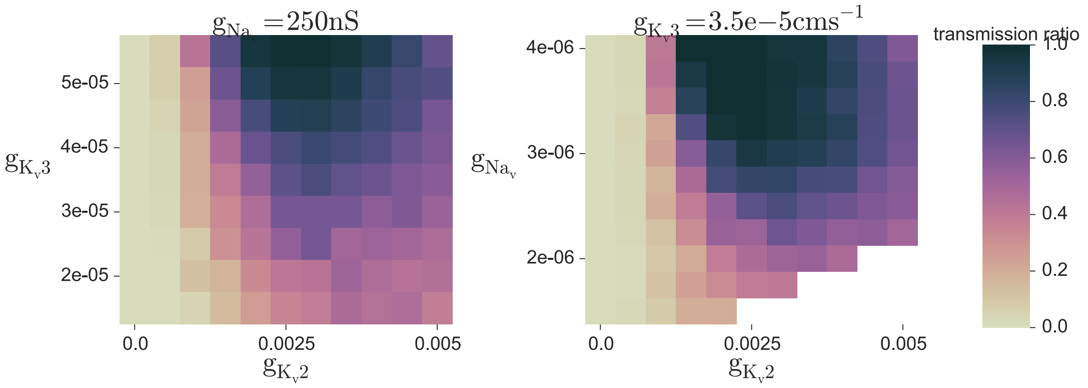

Figure 2.17: Transmission ratio of EPSPs at across the entire range of conductances, as either g_{K_v3} is varied against g_{K_v2} (left), or g_{Na_v} is varied against g_{K_v2} (right). Representative values of g_{Na_v} or g_{K_v3} are fixed as the remaining conductances are varied while generating the respective heatmaps. Areas filled in white correspond to conductance values which do not fulfill the single-spiking objective (either by not spiking or by spiking multiple times).

2.4.4 *Evaluating the model fitness*

The fitness of our model can be evaluated according to the above objectives by simply combining the individual errors into a single value. We use the sum of squares of the relative errors, such that

$$\text{model error} = \sum_{x} \left(\frac{x_{\text{error}}}{x_{\text{resolution}}} \right)^2, \tag{2.26}$$

where x represents each objective, and the resolutions of x are 100 pA, 0.05 ms, 5 mV and 0.1 for the AP threshold, AP halfwidth, AP peak and transmission ratio respectively. The purpose of these resolutions are to set the desired precision of each objective when evaluating model fitness.

Figure 2.18 shows the model errors across the entire range of conductances. The best fits for the naive condition are models with intermediate values for g_{K_v3}, g_{K_v2}, and g_{Na_v}. The best fits for the NO-activated condition are models with high values for g_{K_v2} and low values for g_{Na_v}. The centre-of-mass of the best fits are $g_{K_v2} = 0.0025\,\text{cms}^{-1}$, $g_{K_v3} = 2.35 \times 10^{-5}\,\text{cms}^{-1}$ and $g_{Na_v} = 300\,\text{nS}$ for the naive state and $g_{K_v2} = 0.0045\,\text{cms}^{-1}$, $g_{K_v3} = 3.2 \times 10^{-5}\,\text{cms}^{-1}$ and $g_{Na_v} = 260\,\text{nS}$ for the NO-activated state, which correspond to model errors of 5.6 and 2.8 respectively for each state. These results are in broad agreement with what was observed by Steinert et al.

(2011, 2008); namely that g_{K_v2} increases and g_{Na_v} decreases following NO modulation. Additionally, the behaviour of the fitness of the model as either g_{K_v3} or g_{Na_v} is varied against g_{K_v2} is not strongly dependent on whether the third channel is in a low (left column) or high (right column) conductance regime. As such we can be confident of the robustness of these observations to changes in the particular conductance values. The low and high conductance values are $g_{Na_v} = 200\,nS$, $g_{K_v3} = 2.5 \times 10^{-5}\,cms^{-1}$ and $g_{Na_v} = 350\,nS$, $g_{K_v3} = 5.5 \times 10^{-5}\,cms^{-1}$ respectively.

2.5 METABOLIC EFFICIENCY

The brain uses up to 20 % of the total metabolic energy of the human body at resting state, even though it only makes up 2 % of human bodyweight (Attwell and Laughlin, 2001; Kety, 1957). This enormous disparity is explained by the unusually expensive processes involved in neuronal signalling, with AP generation and post synaptic glutamatergic signalling using the majority of the brains' metabolic energy budget. Estimates range from 22-47 % for AP generation and 34-44 % for EPSP generation, although high-frequency firing tends to increase the proportion of metabolic energy used during AP generation (Attwell and Laughlin, 2001; Howarth et al., 2012; DiNuzzo and Giove, 2012).

The high precision and firing frequency required by neurons in auditory brainstem nuclei make these regions one of the most metabolically expensive in the brain (Brownell and Manis, 2014), and the MNTB has particularly high levels of metabolic markers such as GLUT3, mitochondria , and Na^+/K^+-ATPase, compared with other auditory brainstem nuclei (Trattner et al., 2013).

A number of theoretical and experimental studies have explored the influence of ion channel properties on the metabolic cost of AP generation (Hasenstaub et al., 2010; Alle et al., 2009; Sengupta et al., 2010; Hallermann et al., 2012; Fohlmeister, 2009). These studies use proxies of ATP consumption in order to asses the metabolic efficiency of AP generation. ATP is not consumed directly by the Na_v and K_v channels responsible for depolarisation and repolarisation, as active currents are driven by the potential differences present due to a neuron's Na^+ and K^+ gradients. However, these gradients are reduced by Na^+ influx and K^+ efflux during an AP, and must be restored by an ion pump, which consumes ATP (Figure 2.19). As the number of ATP

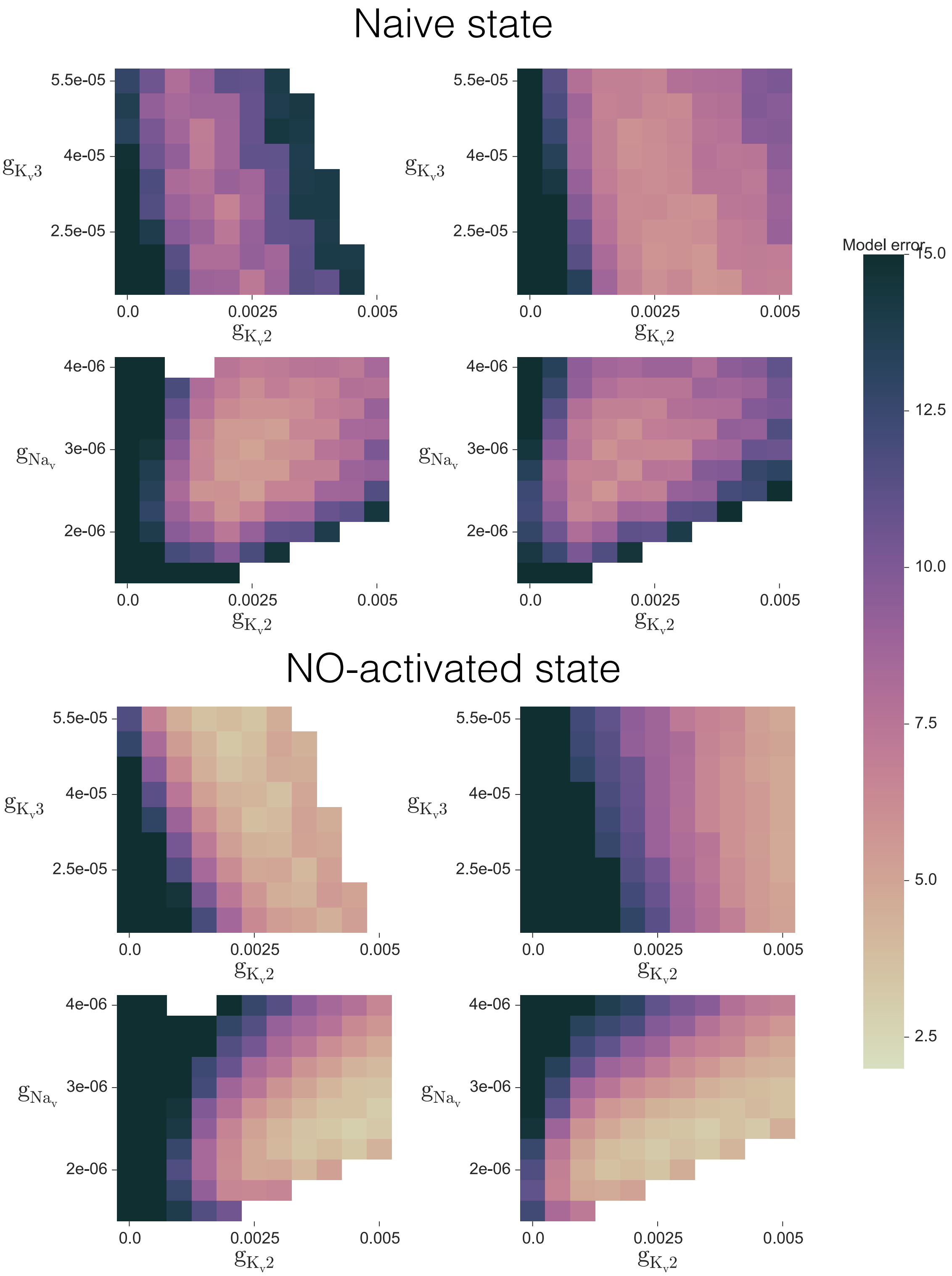

Figure 2.18: Model errors across the entire range of conductances, as either g_{K_v3} or g_{Na_v} is varied against g_{K_v2}, for the naive (top four panels) and NO-activated (bottom four panels) state. Representative values of g_{Na_v} or g_{K_v3} are fixed as the remaining conductances are varied while generating the respective heatmaps, with low conductances in the left column and high conductances in the right column.

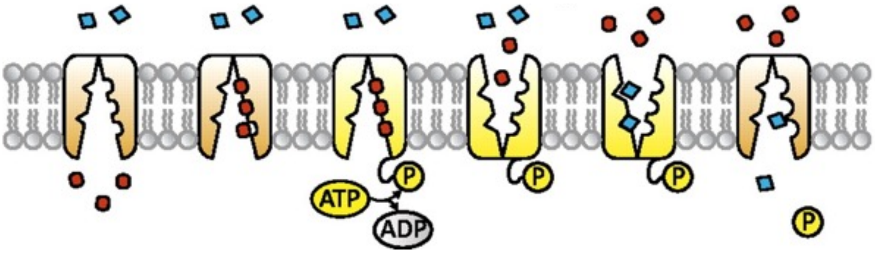

Figure 2.19: Illustration of the action of the Na^+/K^+-ATPase. Each phosphorylation cycle of the pump, triggered by the hydrolysis of an ATP molecule, causes an exchange of 3 intracellular Na^+ ions (red ovals) with 2 extracellular K^+ ions (blue diamonds), thus reversing the Na^+ influx and K^+ efflux due to AP generation. Figure from (Hasenstaub et al., 2010).

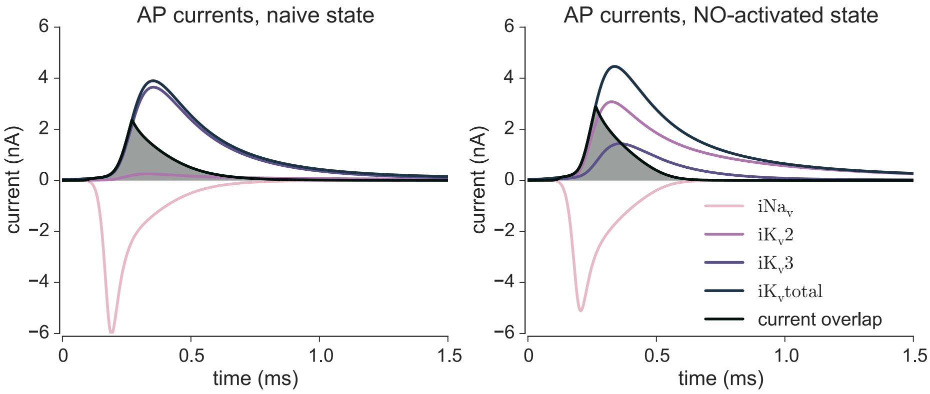

Figure 2.20: The effect of simulating NO modulation on the current overlap (shaded region) during an AP. Stimulus is a conductance based synaptic input given by the **Exp2Syn** function in NEURON (Carnevale and Hines, 2006) with a rise-time of 0.1 ms, decay-time of 2 ms, and reversal potential of 0 mV. The naive (left) and NO-activated (right) states are shown.

molecules required to restore the ion gradients depends on the magnitude of the ion fluxes during an AP, measures of metabolic efficiency are related to these ion fluxes.

Any temporal overlap of Na^+ and K^+ currents during an AP (illustrated in Figure 2.20) is metabolically inefficient, as it will have little impact on the depolarisation of a neuron due to incoming K^+ currents, while contributing to a decrease of ion gradients. This gradient will then have to be reversed by Na^+/K^+-ATPase, therefore consuming ATP. Sengupta et al. (2010) have shown that the current overlap between Na^+ and K^+ is closely related to the overall metabolic efficiency of an AP, measured by the ratio of Na^+ used in an AP compared to the theoretical minimum required to charge the membrane capacitance.

2.5.1 *Simulating the effect of NO on metabolic efficiency*

Figure 2.20 shows the effect that NO modulation has on the current overlap during an AP in our MNTB model. The overlap is 5.7 % higher in the NO-activated state, primarily due to the increased g_{K_v2}. However, K_v2 activates slightly earlier than K_v3 (its peak is at 0.33 ms in comparison with 0.36 ms for K_v3) due to its lower voltage activation, which also contributes to the increase in current overlap in the NO-activated state.

Figure 2.21 shows the charge overlap ratio across the entire range of conductances. The charge overlap ratio is defined as $\frac{\int \min(|iNa_v|,|iK_v|)dt}{\int |iNa_v|dt}$. A ratio of 0 indicates that there is no charge overlap between the Na^+ and K^+ currents, and that the AP has perfect metabolic efficiency. A ratio of 1 indicates that there is maximal charge overlap and that the AP is extremely inefficient. The charge overlap ratio depends largely on g_{K_v2}, and is relatively invariant with respect to the remaining conductances. This indicates that metabolic efficiency is 10 - 20 % lower for those models which best fit the NO-activated state (i. e. those with with high values for $g_{K_v2} \sim 4 \times 10^{-3}\,cms^{-1}$, see Figure 2.18) compared with models which best fit the naive state ($g_{K_v2} \sim 1.5 \times 10^{-3}\,cms^{-1}$).

2.5.2 *The effect of NO on K^+ efflux*

In addition to decreasing the metabolic efficiency of AP generation, NO also increases the overall flux of K^+ ions during an AP. This is demonstrated in Figure 2.20, in which K^+ efflux (area under the iK_vtotal curve) is 31 % higher in the NO-activated state than in the naive state. Since Na^+/K^+-ATPase consumes one ATP molecule while exchanging 3 Na^+ ions for 2 K^+ ions, the metabolic cost, in number of ATP molecules, can be easily calculated from the K^+ efflux. In Figure 2.20, the K^+ efflux in the naive condition is 4.62×10^{-12} C, which can be converted as follows,

$$4.62 \times 10^{-12}\,C = 4.62 \times 10^{-12}\,\frac{N_A}{F}\,e, \text{ which corresponds to } 2.88 \times 10^{7}\,K^{+}\text{ions} \quad (2.27)$$

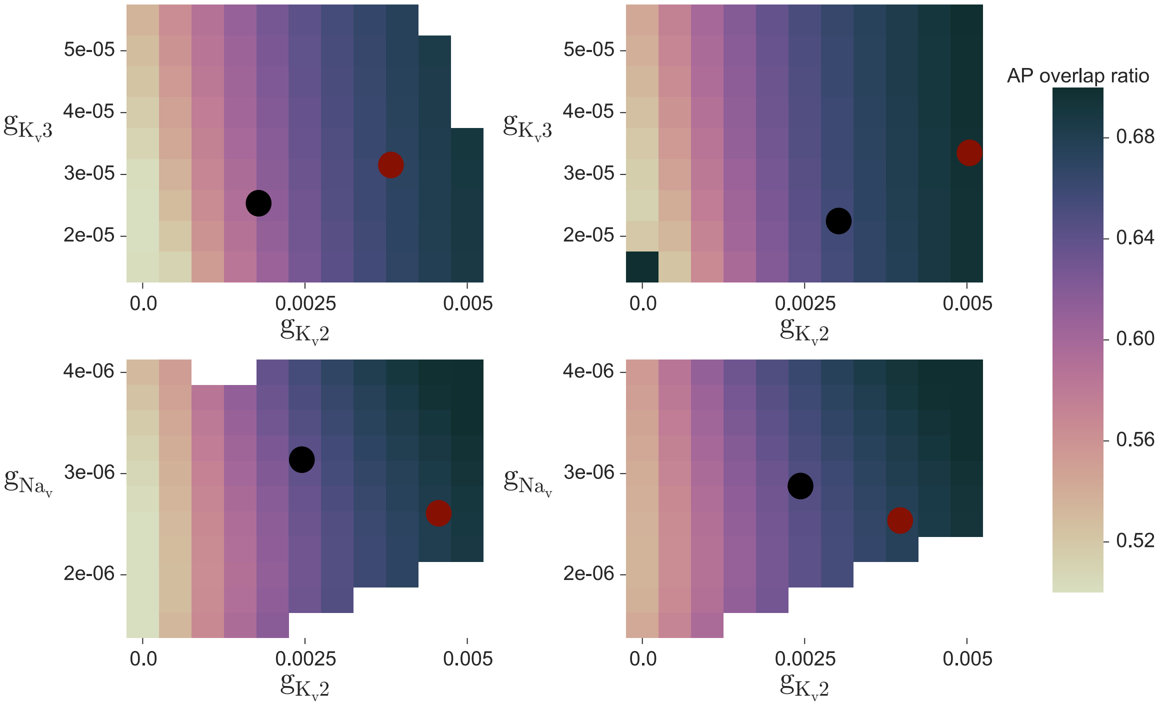

Figure 2.21: The charge overlap ratio, a proxy of metabolic efficiency, across the entire range of conductances, as either g_{K_v3} or g_{Na_v} is varied against g_{K_v2}. Representative values of g_{Na_v} or g_{K_v3} are fixed as the remaining conductances are varied while generating the respective heatmaps, with low conductances in the left column and high conductances in the right column. Black circles show the centre-of-mass of best fits for the naive state, and red circles show the centre-of-mass of best fits for the NO-activated state (see Figure 2.18).

where F is the Faraday constant, N_A is the Avogadro constant and e is the charge of a single electron. (McNaught and Wilkinson, 1997). Since two K^+ ions are exchanged for each molecule of ATP consumed, this corresponds to 1.44×10^7 ATP molecules consumed per AP. In the NO-activated state, a similar calculation leads to a value of 1.85×10^7 ATP molecules consumed per AP, 28 % higher than in the naive state. Note that these values only take into account the ion flux at the soma and the AIS, and ignore any flux which occurs further along the axon or in dendrites during an AP, which must also be reversed by Na^+/K^+-ATPase. Attwell and Laughlin (2001) perform this calculation for an average cortical pyramidal cell, arriving at values of 0.41×10^7 ATP molecules per AP for the cell body, and 3.3×10^8 for the entire pyramidal cell.

Although Na^+ influx is slightly higher in the naive state than in the NO-activated state, this does not affect the final ATP consumption, as the action of Na^+/K^+-ATPase in restoring the K^+ gradient will also restore the Na^+ gradient, by exchanging 3 Na^+ ions for 2 K^+ during each cycle (the K^+ efflux is ~ 2 times larger than the Na^+ influx in Figure 2.20). Note that this situation differs from those discussed by Attwell and Laughlin (2001), in which Na^+ influx is larger than K^+ efflux during an AP, and Na^+ is used to estimate ATP consumption in those cases as a consequence.

2.5.3 *NO mediates a tradeoff between metabolic efficiency and transmission fidelity*

Although the properties and function of ion channels in the MNTB are relatively well-characterised, it is not entirely clear why the coexistence of two different K_v channels which mediate AP repolarisation (that is, K_v3 and K_v2) is necessary in the MNTB, and why NO signalling is present as a mechanism which determines the dominant K_v conductance. Since maintaining K_v2 as the dominant channel during periods of both high and low synaptic activity confers no obvious disadvantage in terms of the transmission ratio of incoming EPSPs, an open question remains as to why there is a transition to K_v3 as the dominant conductance during periods of low synaptic activity.

The results discussed above present a plausible explanation for the NO-mediated transition between K_v3 and K_v2. Since AP generation is more metabolically expensive in the NO-activated state, both in terms of efficiency and in actual ATP consumption, this can explain why K_v2 is only active during periods of high synaptic activity. During periods of low synaptic activity, in the naive state, AP repolarisation which is dominated by K_v3 channels is sufficient to maintain a high EPSP transmission ratio. As a consequence, maintaining higher levels of K_v2 conductances would be a waste of metabolic resources.

Although an increase in metabolic cost of around 20 % might not seem like an especially large amount, the significance is apparent if we consider recent theoretical studies that demonstrate how finely optimised some brain mechanisms are towards metabolic efficiency (Niven et al., 2007; Hasenstaub et al., 2010). For example, Alle et al. (2009) have shown that the metabolic cost of AP generation in hippocampal mossy fibres is only 1.3 times the theoretical minimum (compared with a factor of 4 times the theoretical minimum obtained from studies on the squid giant axon by Hodgkin (1975)).

Taken together, these results suggest that a tradeoff exists between EPSP transmission ratio and the metabolic cost of AP generation, and that this tradeoff is mediated by NO modulation of K_v2 and K_v3 channels. We next wish to determine whether this hypothesis is sufficiently testable as to merit empirical investigation.

2.5.4 *Blocking Na^+/K^+-ATPase in the MNTB*

A fairly direct experimental test of this hypothesis would be to somehow block the action of Na^+/K^+-ATPase in MNTB neurons, and observe the consequences of this in both the naive and NO-activated state. We can simulate this in our model by simply adjusting the intracellular concentrations $[K^+]_{in}$ and $[Na^+]_{in}$. Since the reversal potential E_{Na} is explicitly defined in our model of the Na_v channel (Equation 2.2), and is determined by $[Na^+]_{in}$, we actually end up modifying this parameter by an appropriate amount instead of directly modifying $[Na^+]_{in}$. By decreasing $[K^+]_{in}$ and E_{Na} we can demonstrate the consequence of continued AP generation after blocking Na^+/K^+-ATPase, since ion gradients would no longer be restored. Figure 2.22 shows the effect on AP shape after $[K^+]_{in}$ has been reduced from $148\,mML^{-1}$ to $50\,mML^{-1}$, and E_{Na} has been reduced from $55\,mV$ to $5\,mV$. The AP halfwidth is significantly increased by both K^+ depletion and Na^+ accumulation. The AP peak, on the other hand, increases following K^+ depletion but decreases following Na^+ accumulation.

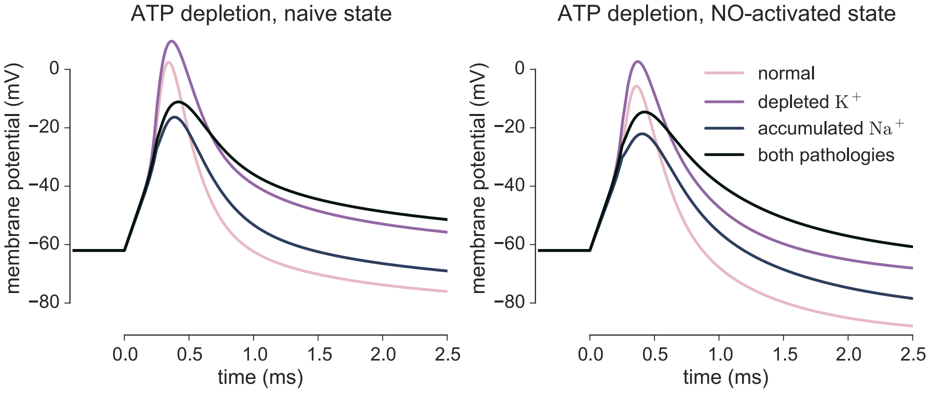

Figure 2.22: The effect of blocking Na^+/K^+-ATPase on AP dynamics in both the naive (left) and NO-activated (right) state. Stimulus is a square current pulse of 1500 pA for 0.25 ms, starting at 0 ms. The naive and NO- activated states are shown, and the effects of only K^+ depletion and Na^+ accumulation are illustrated separately, as well as the effect of ATP depletion (i. e. both of these).

We are assuming that changes in the extracellular concentrations $[K^+]_{ex}$ and $[Na^+]_{ex}$ are negligible due to the relatively small volume of a cell body compared with extracellular space, and that there are no differences in ion concentrations between different cellular compartments such as the soma and AIS (i. e. that these ion gradients balance instantaneously through ionic diffusion compared with the timescales we are interested in). Note that in Figure 2.22 the magnitude of K^+ depletion and Na^+ accumulation are the same in both the naive and NO-activated state; this is to illustrate that the effect of ATP depletion is consistent across both states - our hypothesis claims that this change would occur faster in the NO-activated state.

After further decreases in reversal potential than shown in Figure 2.22, the membrane potential would eventually drift towards a constant depolarised state, in which AP generation completely fails. This transition is discussed by Le Masson et al. (2014), who also show that neurons with a higher ATP demand (such as MNTB neurons in the NO-activated state) are more susceptible to this transition. By calculating the change that one AP has on the $[K^+]_{in}$, we can estimate how many APs a neuron can sustain before K^+ is completely depleted, and therefore how long we would expect a neuron to maintain AP generation under a given stimulus protocol before AP failures occur. With an initial $[K^+]_{in}$ of 148 mML^{-1}, this corresponds to $\sim 3.4 \times 10^{11}$ K^+ ions for a cell volume of $\sim 4.5 \times 10^{-12}$ L (this value is in broad agreement with a volume of $\sim 3.4 \times 10^{-12}$ L obtained from three-dimensional reconstruction of electron microscopy scans by Sätzler et al. (2002)). Compared with the efflux per AP of

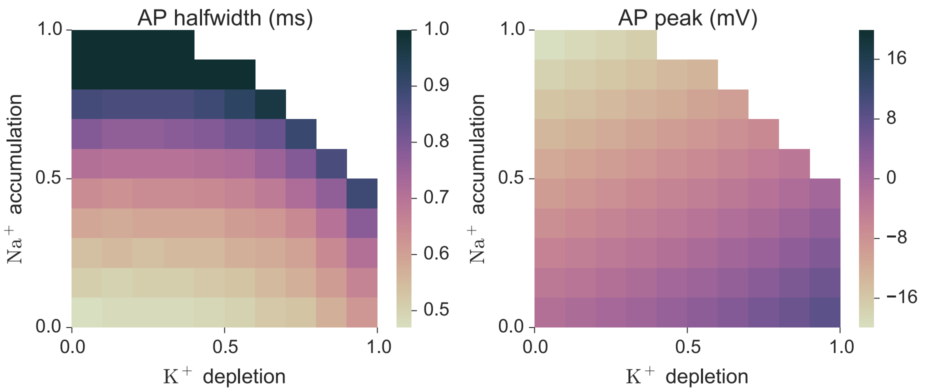

Figure 2.23: The effects of K^+ depletion and Na^+ accumulation on AP halfwidth (left) and AP peak (right). Stimulus is a square current pulse of 450 pA for 200 ms. K^+ depletion and Na^+ accumulation both contribute to an increase in AP halfwidth, but affect AP peak in opposite directions. Areas filled in white correspond to values in which no AP occurs.

2.88×10^7 K^+ions in the naive state and 3.68×10^7 K^+ions in the NO-activated state, this gives us estimates of ~ 11800 APs and ~ 9200 APs in the naive and NO-activated state respectively before $[K^+]_{in}$ is completely depleted. By evoking APs at a rate of 100 Hz, we would therefore expect AP failures to occur after a matter of minutes, even accounting for the fact that a lower ion gradient as K^+ is depleted could lead to a decreased K^+ efflux per AP.

2.6 TESTING THE METABOLIC TRADEOFF HYPOTHESIS IN AN EXPERIMENT

The scenario discussed above, in which Na^+/K^+-ATPase is blocked in order to elicit changes in AP properties and eventual AP failures, can be tested using an experimental protocol similar to that described in Steinert et al. (2011). 2-deoxyglucose is a pharmacological agent which blocks glycolysis, a process responsible for ATP production (Bacallao et al., 1994). Using this in the experimental preparation will induce ATP depletion, therefore blocking Na^+/K^+-ATPase action. We would expect AP failures to occur in both the naive and NO-activated state when ATP depletion is induced. Crucially, AP failures would occur earlier in the NO-activated state compared to the naive state if our hypothesis is correct.

Since K^+ depletion and Na^+ accumulation have opposite effects on the AP peak, it is best to use AP halfwidth as a measure of ATP depletion, as it is increased by both K^+ depletion and Na^+ accumulation (see Figure 2.23). A number of pilot recordings

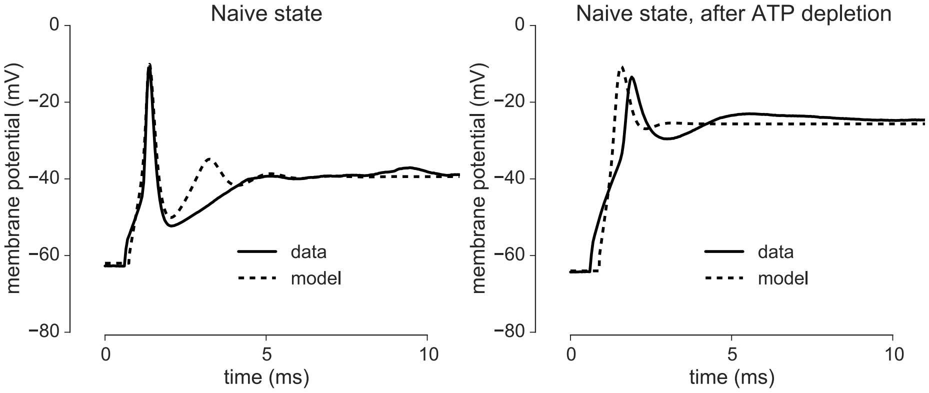

Figure 2.24: A fit of the MNTB model to an intracellular recording of the membrane potential in the naive state (left), and in the same neuron after ATP is depleted by the application of 2-deoxyglucose (right). Stimulus in both the experiment and in the model is a 480 pA current pulse lasting for the entire duration shown. For the model after ATP depletion (right), the same conductances that achieved the fit in the original recording (left) were used, but $[K^+]_{in}$ is reduced from 148 mML^{-1} to 40 mML^{-1}, and E_{Na} is reduced from 55 mV to 5 mV.

have been completed by our experimental collaborators in the lab of Ian Forsythe, using the above protocol in the naive state. APs are evoked via current injections at 100 Hz in the presence of 2-deoxyglucose, leading to eventual AP failures as expected. These AP failures are not due to vesicle release failure as the injected current does not depend on synaptic activity. The responses of these neurons to injected step currents of different amplitudes are recorded periodically. These stimuli have been shown to be effective in constraining conductance-based neuron models by Druckmann et al. (2011), and we will attempt to individually fit our existing model to these recordings.

2.7 FITTING TO INDIVIDUAL NEURONS

We will again use the multi-objective optimisation method (subsection 2.3.3, Druckmann et al. (2007)), although we will use different objectives which are more suited to the experimental stimulus protocol, and an optimisation algorithm instead of simply performing a brute force parameter sweep. The objectives used are the AP halfwidth, AP peak, and the steady-state membrane potential after an AP (i. e. the membrane potential at 10 ms in Figure 2.24).

Figure 2.24 shows the the result of fitting our model to a recording. The downhill simplex algorithm implemented in SciPy was used (Wright, 1996; Van Der Walt et al.,

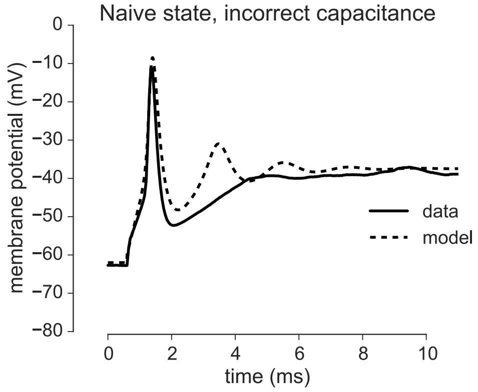

Figure 2.25: A fit of the MNTB model to an intracellular recording of the membrane potential in the naive state. Stimulus in both the experiment and in the model is a 480 pA current pulse lasting for the entire duration shown. The specific membrane capacitance used in the model is $1.0\,\mu\mathrm{F cm}^{-2}$, as opposed to the value of $0.63\,\mu\mathrm{F cm}^{-2}$ used in Figure 2.24.

2011) to minimise the RMS error of the objectives. A good agreement between the data and the model can be achieved. Future attempts at fitting the model could explore using the LM algorithm, as this is generally more robust, but slower, than the downhill simplex algorithm (Levenberg, 1944; Marquardt, 1963).

Interestingly, using the conductance values acquired from fitting to the recording in the naive state, we can achieve reasonable agreement with the recording performed after ATP depletion by only changing $[K^+]_{in}$ and E_{Na} (as demonstrated in Figure 2.22) in the original fit. The right plot in Figure 2.24 demonstrates how our model correctly predicts the effect of ATP depletion in the experiment; a broader AP, slightly lower AP peak, and a higher membrane potential after AP recovery.

Figure 2.25 illustrates a benefit of fitting neuron models to individual recordings as opposed to the average of a population of neurons. We can use extra information such as the capacitance of the neuron at the time of recording and insert it into our model. This gives a more accurate fit; the AP halfwidth of the model is much closer to that of the data in Figure 2.24 than in Figure 2.25, since the recorded specific membrane capacitance of $0.63\,\mu\mathrm{F cm}^{-2}$ used instead of the default value of $1.0\,\mu\mathrm{F cm}^{-2}$ from the population average allows for a narrower AP. Fitting to the properties of an individually recorded neuron is also important as it avoids the problem of the 'failure of averaging', cogently illustrated by Golowasch et al. (2002).

2.8 DISCUSSION

We have constructed a multicompartmental conductance-based model of the MNTB, which can reproduce AP and stimulus response features observed in both the naive and NO-activated state. Since our model has successfully captured a broad range of the effects of NO modulation, and since these effects are quite robust across the range of physiological parameters which we have defined, we can be fairly confident that it achieves a faithful representation of the underlying conductances we have chosen to vary. In this sense, the MNTB can be thought as a good model system, as there is relatively little cell-to-cell variability in conductances compared to, for example, cortical areas, and the simple morphology allows us to precisely investigate the importance of a handful of parameters compared with more complex neuron morphologies (Toledo-Rodriguez et al., 2004; Brew and Forsythe, 2005). We found that whether a model best matched the naive or NO-activated state is determined primarily by K_v2 conductances (Figure 2.18), as expected from experiment (Steinert et al., 2011).

Our model allowed us investigate the metabolic efficiency of AP generation in both the naive and NO-activated state, something which cannot be achieved with the original experimental data used to constrain the model. We found that the charge overlap ratio, a proxy of metabolic efficiency, is consistently higher for neurons in the NO-activated state compared to the naive state (Figure 2.21). This is also the case for a more direct measure of metabolic cost; a model neuron with a high match to the naive state consumes 1.44×10^7 ATP molecules in order to reverse the K^+ efflux during an AP, compared with 1.85×10^7 ATP molecules consumed per AP in the NO-activated state. This corresponds to an increase in metabolic cost of 28 %. This effect is present across the entire range of conductances identified as physiologically realistic, with the metabolic efficiency consistently decreasing as g_{K_v2} increases.

These results provide a plausible explanation for the existence of a signalling pathway which switches from K_v3 to K_v2 as the dominant potassium channel only after periods of high synaptic activity. Since a significant metabolic cost is associated with this transition, we propose that there is a tradeoff between the ability of a neuron to maintain high-frequency synaptic transmission, and the metabolic efficiency of AP generation. Although the concept of a tradeoff between metabolic efficiency and performance has been discussed previously in the context of ion channel combinations (Niven et al., 2007; Hasenstaub et al., 2010; Sengupta et al., 2010), this is to our knowledge the first example of a mechanism which may dynamically mediate the balance of this tradeoff by modulating ion channel combinations in response to electrical activity. Preliminary experiments are now underway in order to test this metabolic tradeoff hypothesis. We have simulated the effects of ATP depletion in our model in order to aid the design of suitable experimental stimuli and best define appropriate experimental measures.

Since nNOS, the protein responsible for NO synthesis, is widely expressed in other brain regions in addition to the MNTB, it is likely that its potential role in regulating metabolic efficiency is widespread (Garthwaite, 2008; Pape and Mager, 1992). Both K_v3 and K_v2 channels are also widely expressed across different neuron types, most prominently in the hippocampus, but also in other cortical and cerebellar areas (Weiser et al., 1995; Rudy and McBain, 2001; Trimmer and Rhodes, 2004; Murakoshi and Trimmer, 1999). Although we have focused primarily on the MNTB throughout this chapter, Steinert et al. (2011) also observed similar NO-mediated modulation of K_v3 and K_v2 in CA3 pyramidal neurons in the hippocampus. We therefore investigated the metabolic efficiency of action potential generation in an existing model of the CA3 pyramidal neuron, described by Meeks and Mennerick (2007). This model is a reduced version of previous CA3 pyramidal neuron models constructed by Mainen et al. (1995); Traub et al. (1991). As expected, and in agreement with our previous results from modelling the MNTB, the current overlap was 0.60 in the naive state, where K_v3 is the dominant repolarising current, and 0.66 in the NO-activated state, where K_v2 is the dominant repolarising current (Figure 2.26). This corresponds to an increase of 12 % in current overlap, and therefore a decrease in metabolic efficiency.

An intriguing property of NO which we have neglected thus far is that, as a small and non-polar gaseous molecule, it can diffuse freely across cell membranes (Gally et al., 1990). This raises the possibility that the concentration of NO could be used as a signal, not only of the activity levels of an individual neuron, but of the average activity levels of a population of neurons. As nitric oxide has also been implicated as a vasodilator, increasing blood flow and the supply of oxygen to brain regions, it is likely that it plays a multifaceted role in regulating the supply and demand of metabolic resources (Dirnagl et al., 1993; Gally et al., 1990; Philippides et al., 2005).

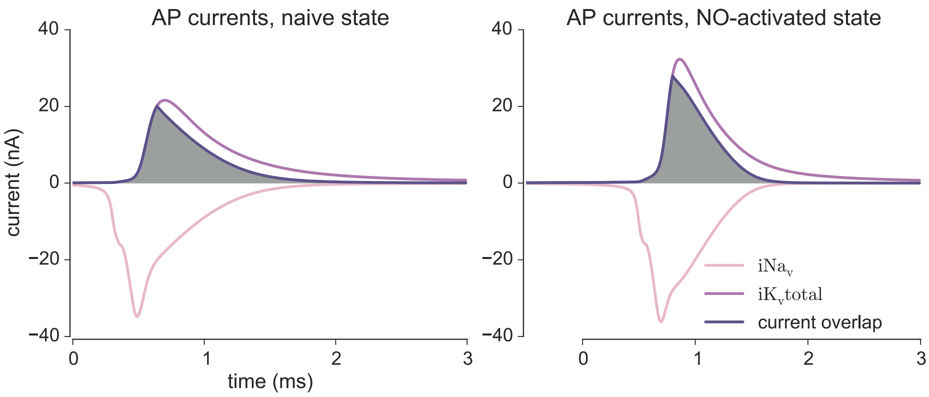

Figure 2.26: The effect of simulating NO modulation on the current overlap (shaded region) during an AP, in a reduced model of a CA3 pyramidal neuron (Meeks and Mennerick, 2007). Stimulus is a square current pulse of 1000 pA for 2 ms. The naive (left) and NO-activated (right) states are shown.

This could be especially relevant in the hippocampus, a brain region that is particularly vulnerable to metabolic strain, where it was recently demonstrated by Lourenço et al. (2014) that diffusion of nNOS-derived NO couples glutamatergic activity and vasodilation (Osborne et al., 2015).

The consequences of a diffusive activity-dependent signal which can be shared by a population of neurons, called a *volume transmitter* (Gally et al., 1990), will be explored further in the next chapter.

3

DIFFUSIVE HOMEOSTASIS IN CORTICAL NETWORKS

CHAPTER SUMMARY

Neural firing rates must be maintained within a stable range in the face of ongoing fluctuations in synaptic connectivity. Existing cortical network models achieve this through various homeostatic mechanisms which constrain the excitability of individual neurons according to their recent activity. Here, we propose a new mechanism, *diffusive homeostasis*, in which neural excitability is modulated by nitric oxide, a gas which can flow freely across cell membranes. Information about a neurons' firing rate can be carried by nitric oxide, meaning that an individual neurons' excitability is affected by neighboring neurons' firing rates as well as its own. We find that this allows a neuron to deviate from the target population activity, as its neighbors will counteract this deviation, thus maintaining stable average activity. This form of neural heterogeneity is more flexible than assigning different target firing rates to individual neurons. Consequently, networks endowed with this diffusive mechanism have an improved representational capability compared to canonical, local homeostatic mechanisms, and allow for more efficient use of neural resources.

The results discussed in this chapter have been published as a research article in PLOS Computational Biology (Sweeney et al., 2015).

3.1 INTRODUCTION

Nitric oxide (NO) is a diffusive neurotransmitter which is widely synthesized in the central nervous system, from the retina to the hippocampus (Garthwaite, 2008; Pape and Mager, 1992). Its properties as a small nonpolar gas molecule allows rapid and unconstrained diffusion across cell membranes, a phenomenon often called *volume transmission* (Gally et al., 1990). An important role of NO signaling is to regulate neural excitability through the modulation of potassium conductances in an activity-dependent manner, effectively mediating a form of homeostatic intrinsic plasticity (HIP). Experiments characterizing this effect also demonstrated that NO-synthesizing neurons can induce changes in the excitability of neurons located up to 100 µm away (Steinert et al., 2008, 2011). These findings are corroborated by a recent study demonstrating neurovascular coupling mediated through activity-dependent NO diffusion (Lourenço et al., 2014). We build upon these observations, postulating a general form of HIP mediated by a diffusive neurotransmitter such as NO which we will refer to as *diffusive homeostasis*. This contrasts with canonical models of HIP, here referred to as *non-diffusive homeostasis*, which assume that each neuron has access to only its own activity (LeMasson et al., 1993).

Theoretical studies of HIP have generally focused on its role in maintaining stable network dynamics (Lazar et al., 2009; Olypher and Prinz, 2010). It has also been recently demonstrated that HIP can improve the computational performance of recurrent networks by increasing the complexity of network dynamics (Naudé et al., 2013). However, little is known about the effects of HIP on the heterogeneity typically observed in cortical networks; in particular, a growing body of evidence supports the finding that even neurons of the same type have a broad and heavy-tailed distribution of firing rates (Wohrer et al., 2013). Rather than an epiphenomenon of biological noise, neural heterogeneity has been proposed to improve stimulus encoding by broadening the range of population responses (Marsat and Maler, 2010; Tripathy et al., 2013). However, this form of heterogeneity is difficult to reconcile with canonical models of HIP, which generally suppress cell-to-cell variability (Zenke et al., 2013). While some degree of heterogeneity in populations of the same type of neuron may emerge naturally (O'Leary et al., 2013), we found that such independent sources of variability will generally limit the responsiveness of a network through neuronal saturation.

Using network models and dynamic mean field analysis, here we show that networks with HIP mediated by diffusive neurotransmission exhibit a very different and unexpected behavior. Firstly, we report that diffusive homeostasis provides a natural substrate for flexibly maintaining substantial heterogeneity across a network. Secondly, the resulting population heterogeneity enables linear network responses over a wide range of inputs. This not only improves population coding, but enables a good use of available resources by ensuring that all neurons remain functionally responsive to changes in network dynamics.

3.2 METHODS

3.2.1 *Network model*

We simulated a spiking network of leaky integrate-and-fire (LIF) model neurons with conductance-based synapses and injected Ornstein-Uhlenbeck noise, as described by

$$\frac{dv}{dt} = \frac{1}{\tau_m}(E_l - v) + g_e J_e (E_e - v) + g_i J_i (E_i - v) + \sigma_{OU}\eta(t) + J_{ext}(E_e - v)\big(\delta(t - t^{ext})\big) \tag{3.1}$$

$$\frac{dg_e}{dt} = -\frac{g_e}{\tau_e} + \sum_k \delta(t - t^k), \qquad \frac{dg_i}{dt} = -\frac{g_i}{\tau_i} + \sum_k \delta(t - t^k) \tag{3.2}$$

where v is the membrane potential, τ_m the membrane time constant, E_l the leak conductance reversal potential, and σ_{OU} the variance of the injected noise. $\eta(t)$ is an Ornstein-Uhlenbeck process with zero mean, unit variance, and correlation time $\tau_{OU} = 1$ ms (Uhlenbeck and Ornstein, 1930). g_e and g_i are the excitatory and inhibitory synaptic currents respectively, given by Equation (3.2), where t_k denotes the time of all k incoming spikes. The reversal potential of the synapses are denoted by E_e and E_i, the synaptic conductances by J_e and J_i, and the synaptic time constants by τ_e and τ_i. The external input conductance is given by J_{ext}, and t^{ext} denotes the arrival time of external input, modeled as an independent homogeneous Poisson process for each neuron i with rate μ_i. A spike is emitted whenever the membrane potential v exceeds the firing threshold θ, and the membrane potential is then reset to the resting potential value, v_r, after a refractory period, τ_{ref}.

The network was made up of N neurons; $0.8N$ excitatory and $0.2N$ inhibitory, with excitatory and inhibitory synaptic conductances scaled so that the network was in a balanced state (Brunel, 2000). Recurrent connections were random and sparse, with connection probability $\epsilon = \frac{C}{N}$ independent of neuron type, where C defines the mean number of synapses per neuron. The balanced state was achieved in the network through scaling the inhibitory synaptic conductances by a factor of g, such that $J_i = gJ_e$.

3.2.2 *NO synthesis and diffusion*

We assumed that neuronal NO synthase (nNOS) is activated by Ca^{2+} influx following a spike (3.3) and describe the relationship through the Hill equation (3.4), which results in a sigmoidal concentration dependence, where n and K are parameters of the Hill equation (Hill, 1910) and $\tau_{Ca^{2+}}$ and τ_{nNOS} are the timescales of Ca^{2+} decay and nNOS activation respectively.

$$\frac{d[Ca^{2+}]}{dt} = -\frac{[Ca^{2+}]}{\tau_{Ca^{2+}}} + [Ca^{2+}_{spike}]\delta(t_{spike}) \tag{3.3}$$

$$\frac{d[nNOS]}{dt} = -\frac{[nNOS]}{\tau_{nNOS}} + \frac{1}{\tau_{nNOS}} \frac{[Ca^{2+}]^n}{[Ca^{2+}]^n + K^n} \tag{3.4}$$

Throughout this paper we considered the case where all neurons, inhibitory and excitatory, express nNOS. The 2D diffusion equation (3.5) was solved numerically using a spatial resolution ds, diffusion coefficient D and a decay term λ (Philippides et al., 2000).

$$\frac{d[NO]}{dt} - D\nabla^2[NO] = [nNOS] - \lambda[NO] \tag{3.5}$$

Neurons were represented by a point source according to their activated nNOS concentration. This is a reasonable simplification, in particular as the networks we study are assumed to be large compared to the dimensions of individual somata. Periodic boundary conditions were used, as we assume we are simulating a subsection of a cortical network embedded in a larger cortical network with similar network activity. This resulted in a 2D toroidal surface on which diffusion was simulated. Boundary conditions with fixed concentration or fixed zero gradient were also tested, with no appreciable differences in the spatial distribution of NO. However, boundary conditions with nonzero fixed gradients of NO, approximating a large NO sink or source, can affect the spatial distribution of NO, and could hinder the ability of NO to act as a homeostatic readout. For further discussions of the diffusive properties of nitric oxide in neural tissue, see Philippides et al. (2005). Assuming the simulated area represents 1 mm^2 of cortex and contains 5000 neurons, this corresponds to each neuron being separated by a distance of 14μm.

The homeostatic effect of NO was represented in neuron i by an increase in θ_i, the firing threshold, according to the relative difference in intracellular NO concentration [NO] and a target concentration $[\text{NO}]_0$;

$$\frac{d\theta_i}{dt} = \frac{1}{\tau_{\text{HIP}}} \frac{[\text{NO}] - [\text{NO}]_0}{[\text{NO}]}, \tag{3.6}$$

where τ_{HIP} is the timescale of homeostasis.

3.2.3 *Non-diffusive homeostasis*

For simplicity, the implementation of non-diffusive homeostasis is almost identical to that of diffusive homeostasis, in that the putative non-diffusive neuromodulator $[\text{NO}_{\text{non-diffusive}}]$ is synthesized through equations (3.3) and (3.4), and modulates firing thresholds through equation (3.6). The only difference is that the diffusion term in equation (3.5) is removed, so that $[\text{NO}_{\text{non-diffusive}}]$ is entirely determined by the rate of intracellular synthesis and decay;

$$\frac{d[\text{NO}_{\text{non-diffusive}}]}{dt} = [\text{nNOS}] - \lambda[\text{NO}_{\text{non-diffusive}}] \tag{3.7}$$

3.2.4 *Dynamic mean-field analysis*

For a detailed derivation of equations used in our dynamic mean-field analysis, see Brunel (2000) and Roxin et al. (2011). Briefly, under the assumptions that the network is in an asynchronous regime and that a single EPSP is sufficiently small compared to the voltage required to elicit a spike from resting membrane potential, we can extract the mean firing rate of a LIF neuron in a recurrent network by solving a pair of equations under the condition of self-consistency. The synaptic current for a neuron i in a time interval τ can be described by its mean μ_i and standard deviation σ_i as follows:

$$\mu_i = JC\nu\tau, \qquad \sigma_i = J\sqrt{C\nu\tau}, \tag{3.8}$$

where J is the synaptic efficacy, C the number of synapses per neuron and ν the average population firing rate. The expected mean firing rate $\phi_i(\mu_i, \sigma_i)$ of an LIF neuron with this synaptic current is given by

$$\phi_i(\mu_i, \sigma_i) = \left[\sqrt{\pi}\tau_m \int_{\frac{\nu_r - \mu_i}{\sigma_i}}^{\frac{\theta_i - \mu_i}{\sigma_i}} dv e^{v^2} \mathrm{erfc}(-v) \right]^{-1}, \tag{3.9}$$

where erfc is the complementary error function. Since the firing rate described by (3.9) is determined by the synaptic current parameters μ_i and σ_i, which are in turn determined by the population firing rate ν, self-consistency requires that the rate which determines the synaptic current parameters must also be equal to the rate which is produced by these parameters, that is:

$$\nu = \phi_i(\mu_i(\nu), \sigma_i(\nu)). \tag{3.10}$$

We simulated a non-interacting population of neurons described by the mean-field theory, in which all neurons are identical except for their threshold θ_i. Although there is no recurrent excitation within the population, the synaptic current statistics are comparable to that which a neuron within a recurrent network would receive. This enabled us to consider the firing rate distributions arising from presenting single neurons with distributions of synaptic currents, similar to the approach by Roxin et al. (2011).

We assumed that a neuron embedded in a homogeneous network receiving a diffusive homeostatic signal is analogous to a neuron using a combination of its own firing rate and the average population firing rate as a signal. The network can then be reduced to a population in which the firing threshold θ_i of each neuron i is modulated according to

$$\frac{d\theta_i}{dt} = \frac{1}{\tau_{HIP}} \left((1-\alpha)\frac{\phi_i - \phi_0}{\phi_i} + \alpha\frac{\bar{\phi} - \phi_0}{\bar{\phi}} \right), \tag{3.11}$$

where ϕ_0 is the target firing rate and ϕ_i and $\bar{\phi}$ are the firing rate of the neuron i and the population respectively. α was varied between 0 and 1 and can be thought of as the proportion of NO which a neuron receives due to diffusion from other neurons, with $\alpha = 0$ indicating that each neuron senses only its own activity and $\alpha = 1$ indicating that all neurons share an identical population-wide signal.

In order to implement homeostasis in this setup, we iterated through (3.8)-(3.9) until (3.10) is satisfied to a precision of 10^{-4} Hz, where (3.9) returns ϕ_i for each neuron in the population, and $\overline{\phi} = \frac{\sum \phi_i}{N}$ is used as ν in (3.8). At each timestep the thresholds θ_i of each neuron were modulated according to (3.11), and rates ϕ_i were subsequently recalculated from (3.9).

Although the mean field approximation ignores NO dynamics, it is a reasonable approximation for situations in which diffusion of NO occurs much slower than fluctuations in firing rates, and much faster than the homeostatic modulation of neural excitability, ie there is a separation of timescales.

3.2.5 *Investigating the homeostatic steady state.*

External input rates μ_i for each neuron i were randomly drawn from a Gaussian distribution such that $\mu_i \sim \mathcal{N}(10, 10^2)$ Hz. $\mathcal{N}(\mu, \sigma^2)$ denotes a Gaussian distribution, truncated so that there are only positive values, with mean μ and variance σ^2. Since the mean NO concentration takes time to reach a steady state in the recurrent network simulations, we ran the network for 100 s without homeostasis and with all neurons receiving 5 Hz input, defining the target NO concentration $[NO]_0$ to be the mean NO concentration across all neurons at 100 s.

For the dynamic mean field analysis, we chose parameters which roughly match the rate statistics of the recurrent network simulations. Inputs to each neuron were drawn from a Gaussian distribution such that $\mu_i \sim \mathcal{N}(5.7, \delta^2)$, $\sigma_i = \sqrt{\mu_i}$. $\delta = 0.4$ is the width of the distribution of mean inputs to the population. Note that the parameter δ referred to here differs from the δ in (3.1)-(3.3).

3.2.6 *Adding target variability.*

In order to match the distribution of effective targets observed during diffusive homeostasis for networks with non-diffusive homeostasis, we assigned each neuron in the non-diffusive network a different homeostatic target, $[NO_0]_i$. A network without any homeostasis is presented with input statistics ($\mu_i \sim \mathcal{N}(2, 5^2)$ Hz), tuned such that the firing rate distribution match that of the network with diffusive homeostasis. $[NO_0]_i$ for each neuron i can then be drawn from the distribution of steady-state intracellular concentrations of NO for this network. This results in a broad and heavy-tailed distribution of homeostatic targets, as opposed to the single homeostatic target which is used in networks with diffusive homeostasis and the unmodified non-diffusive homeostasis.

A similar approach was adopted in the dynamic mean-field analysis, with each neuron assigned a target firing rate $\phi_{0,i}$ from the steady-state firing rate distribution of a network with $\alpha = 0.8$.

3.2.7 *Investigating homeostatic response to input heterogeneity.*

External input for each neuron i was $\mu_i = 2.5$ Hz ($N = 2500$). NO_0 was set as described previously, although with an input rate of 2.5 Hz. 2 groups of 250 excitatory neurons each were randomly chosen, independent of neuron position, and stimulated with $\mu_{green} = 5$ Hz and $\mu_{blue} = 10$ Hz, keeping the inputs to the remaining neurons unchanged. Firing rates plotted in Figs. 3.4A-C were smoothed with a uniform time window of 20 s. Persistence of input differences were calculated by measuring the length of time it took for the signal-to-noise ratio between the two groups receiving elevated inputs to fall below 0. The signal-to-noise ratio is defined as $(\mu_1 - \mu_2)/(\sigma_1 + \sigma_2)$, where μ_i and σ_i correspond to the mean and standard deviation of the firing rates of group i.

3.2.8 *Investigating network response to changes in input after homeostasis.*

Figs. 3.5A-D were generated using the same simulation setup as described previously. After the network has reached the homeostatic target firing rate, we froze homeostasis. Input rates to each neuron were then regenerated from the same original input distribution, such that $\mu_i^{\text{after}} \sim \mathcal{N}(10, 10^2)$ Hz. $\Delta\mu_i = \mu_i^{\text{after}} - \mu_i^{\text{before}}$ is the difference in input rate each neuron experiences upon this change, and $\Delta\nu_i = \nu_i^{\text{after}} - \nu_i^{\text{before}}$ is the corresponding change in output rate for each neuron. The black lines in Figs. 3.5A-C are from least-squares linear regression, and the R^2 values given were derived from this fit. A similar approach was used in the dynamic mean-field analysis, while varying δ, the width of the input distribution.

3.2.9 *Simultaneous diffusive and non-diffusive homeostasis.*

In networks with both diffusive and non-diffusive homeostasis active, (3.6) is replaced with (3.12), where $\tau_{\text{diffusive}}$ and $\tau_{\text{non-diffusive}}$ represent the timescales of diffusive and non-diffusive homeostasis respectively, and the dynamics of [NO] and $[\text{NO}_{\text{non-diffusive}}]$ are as described in (3.5) and (3.7) respectively.

$$\frac{d\theta_i}{dt} = \frac{[\text{NO}] - [\text{NO}]_0}{\tau_{\text{diffusive}}[\text{NO}]} + \frac{[\text{NO}_{\text{non-diffusive}}] - [\text{NO}_{\text{non-diffusive}}]_0}{\tau_{\text{non-diffusive}}[\text{NO}_{\text{non-diffusive}}]} \tag{3.12}$$

Fig. 3.8A was generated using the same simulation parameters as in Fig. 3.1, while varying $\tau_{\text{non-diffusive}}$ from 1000 to 15000 ms and keeping $\tau_{\text{diffusive}}$ fixed at 2500 ms. These networks were run for 350 s in order to ensure they reached a steady state. Likewise, Fig. 3.8B was generated using the same simulation parameters as in Figs. 3.5A-D, while varying the ratio of timescales.

3.2.10 *Time-varying input.*

In addition to the external input μ_i previously described, the network was randomly separated into groups of 250 neurons. Each group j was stimulated with external Poisson input with a rate given by $\mu_{j,t} \sim \mathcal{N}(0, 25^2)$ Hz. These inputs were regenerated at each timestep t of length 1 s. The time-varying input $\mu_{j,t}$ was also presented during homeostasis. The dotted black line in Fig. 3.9A shows the normalized $\mu_{j,t}$, while colored lines show the normalized rate deviation of a randomly chosen group j from the mean population firing rate.

3.2.11 *Decoding stimulus orientation.*

Each excitatory neuron was randomly assigned a preferred orientation. After the network reached a steady state, homeostasis was frozen. For each trial, each neuron i with preferred orientation θ_i was stimulated with external Poisson input at a rate given by $\mu_b + \mathcal{M}(\theta_s, \sigma_s, \theta_i)$, where $\mu_b = 20$ Hz is the base input rate and $\mathcal{M}(\theta_s, \sigma_s, \theta_i)$ is the amplitude at θ_i of a Gaussian tuning curve centered around the stimulus orientation θ_s, with a width given by $\sigma_s = 90°$ and a peak amplitude of 2.5 Hz. The angle decoded using the population vector method is the angle of the vector sum of all neural responses.

3.2.12 *Model parameters.*

Unless explicitly defined, the parameters used throughout the paper are given in Table 3.1. For synthesis, diffusion, and decay of NO we have attempted to match data when available (Philippides et al., 2000; Salerno and Ghosh, 2009), although the dearth of experimental measurements does not permit for great precision (Hall and Garthwaite, 2009; Batchelor et al., 2010). Additionally, parameters were chosen such that the timescale of homeostasis is separated from that of firing rate fluctuations. This is a reasonable assumption, given that activity-dependent NO modulation likely acts within 10 minutes or slower (Steinert et al., 2011), although NO diffusion occurs on the order of 10 seconds. τ_{HIP} was chosen to be long enough so as to avoid oscillations but short enough so as to allow feasible large scale simulations. This is a common assumption in computational studies (Naudé et al., 2013). Larger simulations, up to $N = 25000$, were run with no discernible difference in results.

All numerical simulations were implemented using the Brian simulator, v1.4.1 (Goodman and Brette, 2008), and the mean-field analysis was implemented using IPython Notebook (Pérez and Granger, 2007). The 2D diffusion equation was solved numerically using an explicit finite difference equation method, using the numpy python package (Van Der Walt et al., 2011). Data analysis was performed with the numpy Python package and plotting with the matplotlib package and seaborn library (Van Der Walt et al., 2011; Hunter, 2007). Simulation code and IPython Notebooks which perform the data analysis and plotting are available at `https://github.com/yannaodh/sweeney-2015`.

Table 3.1: Simulation Parameters.

Neuron		**NO synthesis and diffusion**		**Network**	
E_l	-80 mV	$[\mathrm{Ca}^{2+}_{\mathrm{spike}}]$	1	N	5000
ν_r	-60 mV	$\tau_{\mathrm{Ca}^{2+}}$	10 ms	N_e	0.8N
c_m	0.2 nF	τ_{nNOS}	100 ms	J_e	5.5 nS
τ_m	20 ms	n	3	J_i	64.0 nS
τ_{ref}	5 ms	K	1	C	100
θ_0	-50 mV	D	$1000\ \mu\mathrm{m}^2\mathrm{s}^{-1}$	J_{ext}	80.0 nS
τ_e	3 ms	λ	$0.1\ \mathrm{s}^{-1}$	τ_{OU}	1 ms
τ_i	7 ms	Grid size	$1\ \mathrm{mm}^2$	σ_{OU}	1 mV
E_e	0 mV	ds	2 μm	**Dynamic mean-field analysis**	
E_i	-70 mV	dt (diffusion)	1 ms	θ_0	10 mV
dt	0.1 ms	τ_{HIP}	2500 ms	ν_r	0 mV

3.3 RESULTS

We investigated the effects of diffusive homeostasis in a recurrent neural network (Fig. 3.1A, see Methods) with sparse and random connectivity, based on conventional models of cortical networks giving rise to asynchronous irregular spiking activity (Brunel, 2000). Each neuron received external input with a rate randomly drawn from a normal distribution. Ca^{2+} influx during a spike triggered NO synthesis through nNOS activation (Fig. 3.1B, see Methods). Periodic boundary conditions were used to simulate NO diffusion, as we are simulating a subsection of a cortical network embedded in a larger section with similar activity. This resulted in a 2D toroidal surface on which diffusion was simulated. Boundary conditions with concentration gradients fixed at zero were also tested, with no appreciable differences in the outcome. Each neuron's firing threshold θ_i underwent modulation through negative feedback mediated by the concentration of NO (Equation 3.6 in Methods).

The effect of a diffusive neurotransmitter mediating HIP within the network was investigated by comparing two cases: first where NO was allowed to diffuse freely across cell membranes as observed experimentally (Steinert et al., 2008), and second without diffusion such that intracellular NO concentration was affected only by a neuron's own recent activity (Fig. 3.2). The latter corresponds to a canonical model of HIP as investigated before (Lazar et al., 2009; Olypher and Prinz, 2010).

3.3.1 *Diffusive homeostasis enables a broad firing rate distribution*

Fig. 3.1C illustrates that both forms of homeostasis stabilized network activity following an increase in input. There was however a crucial difference in how the neurons reacted to this change. While for non-diffusive homeostasis each neuron simply returned to its target firing rate, diffusive homeostasis caused each neuron to sense a mixture of its own activity level and that of the rest of the network. This can be seen in the spatial concentration profiles in Fig. 3.1C. It is important to note that the spatial position of each neuron was random and independent of its connections, meaning that there was no explicitly defined structure in the NO concentrations.

As a result, these networks exhibited a very different steady state behavior. The firing rate distribution was narrow as expected for non-diffusive homeostasis, but broad and heavy-tailed for diffusive homeostasis (Fig. 3.1D). The latter is consistent with recent experimental results indicating that firing rate distributions in cortex are generally heavy-tailed, approximating log-normal distributions (Wohrer et al., 2013). There were no noticeable differences in inter-spike interval statistics between networks with diffusive and non-diffusive homeostasis (not illustrated).

We investigated the difference in firing rate distributions by modeling the relation between activity read-out and homeostatic compensation in these two cases using a dynamic mean-field model (see Methods). This approach considered an unconnected population of neurons with random inputs, where each of the two scenarios was simulated by using an appropriate activity read-out. HIP was implemented as in the full spiking model, but the degree of diffusive signaling was now controlled by a single parameter, α (Equation 3.11 in Methods), which determined the balance

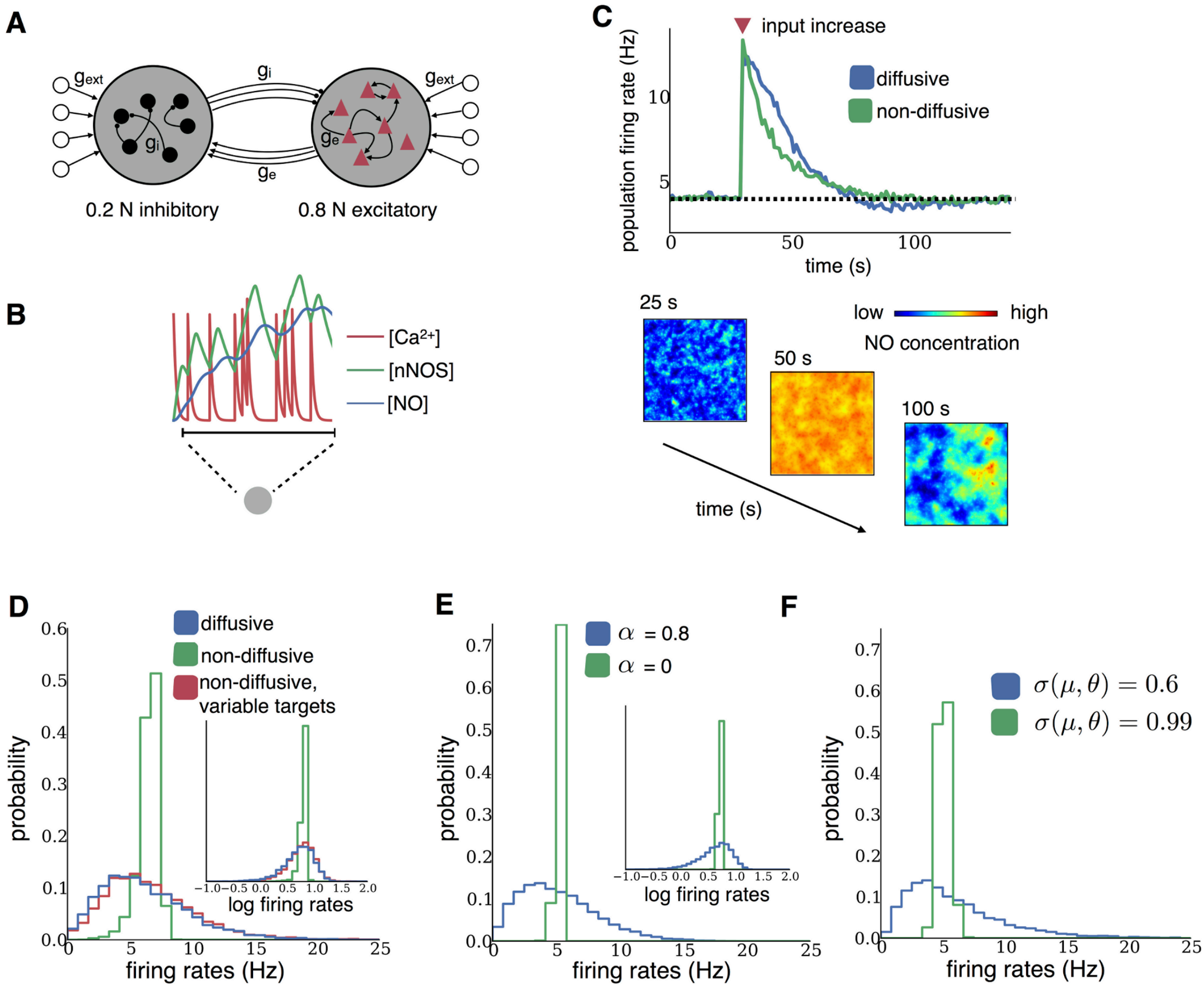

Figure 3.1: Steady-state behavior of diffusive and non-diffusive homeostasis. **(A)** Schematic of the sparsely connected recurrent network model. Neurons received homogeneous random spiking input (g_{ext}). **(B)** Intracellular homeostatic signals in a model neuron (grey circle). Each spike triggers calcium influx, which leads to nNOS activation and NO synthesis. **(C)** Mean population firing rates for networks with diffusive or non-diffusive homeostasis after an increase in external input (red triangle). Spatial distribution of NO concentrations at different times across the network with diffusion are shown below. (**D**-**E**) Distributions of firing rates and log firing rates (insets) after homeostasis from network simulations (D) and mean-field analysis (E), both receiving independent Poisson inputs drawn from a Gaussian distribution. **(F)** Distributions of firing rates in the mean-field analysis for low and high covariance of threshold and input rate.

between local and global activity read-out. If small, neurons used primarily their own activity to modulate their firing threshold, while increasing α caused the firing threshold to depend more strongly on the average population activity. Setting, for instance, $\alpha = 0.8$ led to a broad and heavy-tailed rate distribution similar to the full

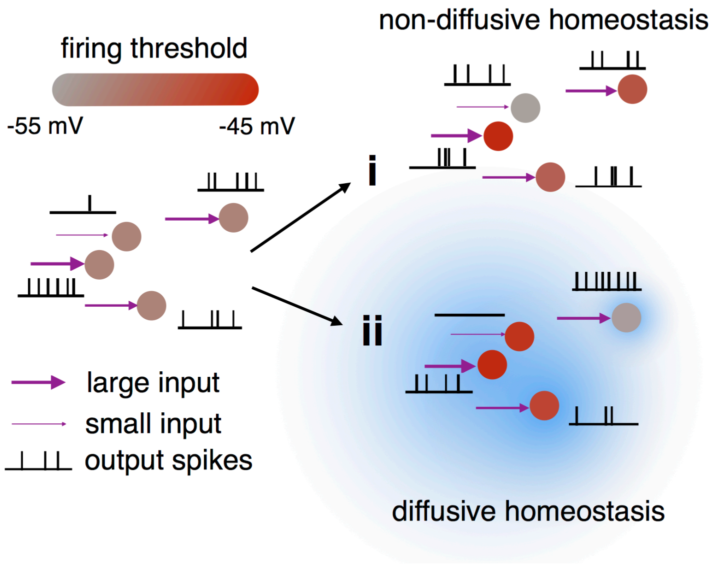

Figure 3.2: Illustration of the effects of non-diffusive (i) and diffusive (ii) homeostasis. Non-diffusive homeostasis adjusts each neuron's threshold (red color bar) according to its input to give identical firing rates, while diffusive homeostasis induces correlations (blue cloud) in the thresholds of neighboring neurons, thereby maintaining diverse firing rates.

model, while $\alpha = 0$ yielded a narrow distribution as in the non-diffusive case (Fig. 3.1E).

This model provides a simple and intuitive explanation for this effect. For a non-interacting population, non-diffusive homeostasis can be thought of as precisely matching a neuron's input μ_i and its threshold θ_i to maintain the target firing rate. We can imitate this by introducing a covariance $\text{cov}(\mu, \theta)$ between μ_i and θ_i, such that a high input rate implies a high firing threshold and a low input rate a low firing threshold. Since setting $\alpha > 0$ (analogous to diffusive homeostasis) introduces a correlation between a neuron's threshold θ_i and the average population threshold $\overline{\theta}$, this effectively results in a decorrelation of μ_i and θ_i in comparison with setting $\alpha = 0$ (analogous to non-diffusive homeostasis). In line with the previous results, populations with for instance $\text{cov}(\mu, \theta) = 0.6$ yielded a broader and more heavy-tailed distribution of firing rates than populations with $\text{cov}(\mu, \theta) = 0.99$ (Fig. 3.1F).

Since non-diffusive homeostasis directly relates the firing threshold of a neuron to its input, we observed a wider distribution of firing thresholds, which in turn ensured that all neurons assumed similar firing rates. Diffusive homeostasis, on the other hand, yielded similar firing thresholds across the population (Figs. 3.3A-B). When combined with the nonlinear input-output relation of neurons (Roxin et al., 2011), this gave rise to the broad firing rate distributions we observed (see also Discussion). This result was robust to changes in the rate of NO diffusion. While decreasing the rate of diffusion, D, did result in slightly narrower firing rate distributions, they were broader than in networks with non-diffusive homeostasis across a wide range of values (Fig. 3.3C). A similar trend was observed when varying the width of the external input rate distribution. While decreasing this width led to a decrease in the width of the firing rate distribution, they were consistently broader in networks with diffusive homeostasis (Fig. 3.3D).

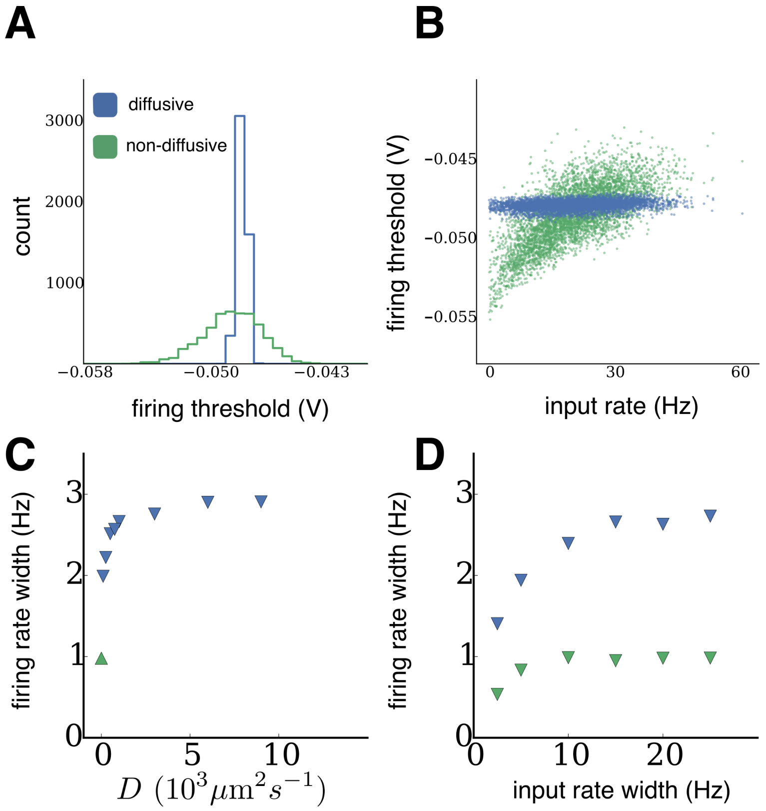

Figure 3.3: Steady-state firing thresholds of diffusive and non-diffusive homeostasis. **(A)** Distributions of firing thresholds after homeostasis from network simulations, receiving independent Poisson input drawn from a Gaussian distribution. **(B)** Steady-state firing thresholds plotted against external inputs received during homeostasis. **(C)** Standard deviation of the steady-state firing rate distribution as the diffusion coefficient D is varied ($D = 1000 \mu m^2 s^{-1}$ in panels A-B). **(D)** Standard deviation of the steady-state firing rate distribution as the input rate width is varied, for networks with diffusive ($D = 1000 \mu m^2 s^{-1}$) and non-diffusive homeostasis (input rate width = 10 Hz in panels A-B).

Since one may argue that diffusive homeostasis is merely adding variability to each neuron's homeostatic signal due to the influence of neighboring neurons' activity, we now ask whether it is possible to achieve broad firing rate distributions with non-diffusive homeostasis. Indeed, by introducing variability of homeostatic targets (see Methods), we could produce a distribution of firing rates similar to that observed with diffusive homeostasis (Fig. 3.1D, red histogram). However, as we will show next, the effect of diffusive homeostasis is quite distinct from that of activity-independent, 'quenched' heterogeneity arising from randomly distributed homeostatic targets.

3.3.2 *Diffusive homeostasis retains input heterogeneity*

To investigate the functional consequences of heterogeneity caused by a diffusive homeostatic process, we next simulated specific changes in external input. First, we stimulated small random groups of neurons at higher input rates of 5Hz and 10Hz (versus a baseline of 2.5 Hz), as illustrated in Fig. 3.4. Such inputs may, for instance, reflect developmental or other plastic changes that lead to a long-lasting change in network input. In these simulations, the average network firing rate was reliably brought back to the original target firing rate by both forms of homeostasis (Figs. 3.4A-C, black traces). As above, in networks with non-diffusive homeostasis this was achieved by returning the rate of each neuron to the target firing rate regardless of their external input (Fig. 3.4A, colored traces). In contrast, for networks with diffusive homeostasis, we found that the separability of firing rates of individual groups are maintained according to their input, while the firing rates of all groups were simultaneously reduced so that the average network firing rate again reached the target (Fig. 3.4B, colored traces). Introducing variability in homeostatic targets for the non-diffusive case, as described previously, did not maintain separability of individual groups as in the diffusive case. Instead, the different groups returned to their mean firing rates that existed before inputs were elevated (Fig. 3.4C).

The distribution of final firing thresholds explains these differences (Figs. 3.4D-F). For non-diffusive homeostasis, neurons in the group receiving 10 Hz input had the highest thresholds since they needed to reduce their firing rate the most, followed by the 5 Hz and 2.5 Hz groups respectively. This led to the final threshold of each neuron reflecting its input. Note that the distribution of firing thresholds is broader in this setup than in (Figs. 3.3A-B), as a broader range of inputs is given to the network. For a diffusive signal, a neuron's firing threshold is modulated by the activity of nearby

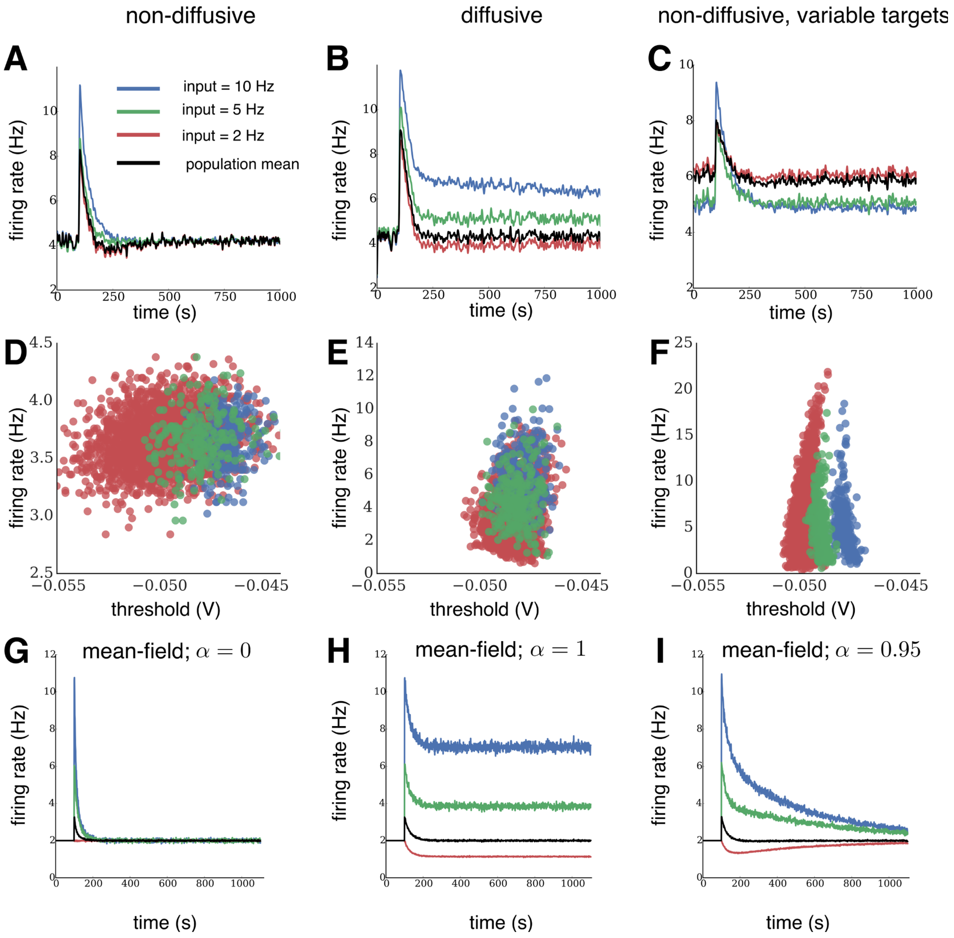

Figure 3.4: Relative differences between inputs are preserved during diffusive homeostasis. **(A-C)** Evolution of firing rates in a recurrent network for each input group under diffusive and non-diffusive homeostatic control, and for variable homeostatic targets. Black traces show average population activity. Independent Poisson input at the target rate was given to 2000 neurons (red), while two groups of 250 neurons each received elevated Poisson input. The relative rate differences of the groups were only preserved for diffusive homeostasis. **(D-F)** Final distributions of firing rates versus firing thresholds. **(G-I)** Evolution of firing rates in a dynamic mean-field population for each input group for purely local ($\alpha = 0$), purely global ($\alpha = 1$), and mixed local and global activity read-out ($\alpha = 0.95$). Black traces show average population activity. Input which leads to a target rate of 2 Hz is given to 2000 neurons (red), while two groups of 250 neurons each receive elevated input.

neurons. Since group membership of a neuron is independent of its position, this effect again introduced a correlation between each neuron's threshold and the mean threshold of the entire network, resulting in a distribution of final thresholds which are less segregated according to their input compared to a network with non-diffusive homeostasis. Thus, firing thresholds in neurons undergoing diffusive homeostasis were more weakly related to their external input. This in turn preserves local firing rate differences in input groups while maintaining constant average network activity. Introducing variable targets for non-diffusive homeostasis caused the thresholds to depend more strongly on their external input, similar to the original non-diffusive case.

We could broadly reproduce the distinctions between diffusive and non-diffusive homeostasis in the dynamic mean-field approach by varying α. For $\alpha = 0$, modeling non-diffusive homeostasis, we obtained identical firing rates in input groups, as in the recurrent network (Fig. 3.4G). Note that changing the input of groups of neurons in the recurrent network also affects the activity of neurons with fixed input (Fig. 3.4B, red traces) due to recurrent connections, an effect that is obviously absent in the dynamic mean-field description. Increasing α led to local firing rate differences persisting for longer periods of time. However, these differences eventually decay very slowly, only remaining stable for the case where $\alpha = 1$ (Figs. 3.4H-I). The reason this occurs is, even after the population activity has quickly reached its homeostatic target, the deviations of the input groups still exert a small homeostatic force when $\alpha < 1$. For example, if $\alpha = 0.95$, there will be a relatively fast change in thresholds as the population activity reaches its target, followed by much slower changes, at $1 - \alpha = 0.05$ times the speed (Fig. 3.4I). This does not happen to the same extent in the spiking network simulations with diffusive homeostasis, as diffusion of NO ensures that deviations from the population activity are directly compensated for by neighboring neurons. Differences persist for 3245 ± 440 s, compared with 115 ± 6 s and 140 ± 40 s for non-diffusive homeostasis with uniform and variable homeostatic targets, respectively (± symbol denotes standard error of the mean of 6 independent network realizations in each case, see Methods). Since we have increased the speed of homeostasis in order to reduce simulation time (see Methods), a more realistic time course of 15 minutes for NO modulation would cause input differences to persist in networks with diffusive homeostasis for many hours to days (Steinert et al., 2011).

Taken together, this shows that diffusive homeostasis can retain input heterogeneity due to the influence of neighboring neurons' activity on an individual neuron's firing threshold.

3.3.3 *Population heterogeneity during diffusive homeostasis enables linear network responses*

In the simulations shown so far, each neuron received a static input throughout since we were interested in the final network states. We now investigate how these networks respond to fast changes in input; specifically how faithfully each neuron represents its change in input. Since networks with diffusive homeostasis simultaneously maintain constant average network activity and firing rate heterogeneity, we expected that this should allow input modulations to be followed more precisely due to a greater representational capability.

After the network reached steady state under an initial distribution of external inputs, we froze homeostasis so as to simulate fast changes in activity, since we assume that homeostasis is not active over these time scales. We then regenerated the external inputs to each neuron from the same distribution presented during homeostasis. This can be thought of as a re-configuration of inputs due to external fluctuations. To best represent such changes in a simple population coding paradigm, each neuron should respond linearly to a change in input; non-linear transformations may lead to an information loss and hence affect neural computations, although this may indeed be desirable in some brain regions. We interpreted the range of changes in input over which this response is linear, or non-saturating, as the range over which homeostasis does not interfere with the network response.

Figs. 3.5A-C show the change in input rate versus change in output rate of each neuron. A highly nonlinear response was observed in networks with non-diffusive homeostasis, with rectification for large decreases in input and superlinear responses for large increases in input. This effect was quantified by an R^2 value of 0.57 from a linear regression. Conversely, networks with diffusive homeostasis exhibited a linear response across the entire range of input changes, with an R^2 value of 0.85. Population heterogeneity can also be achieved, as discussed before, by introducing target variability during non-diffusive homeostasis. This yielded a similar non-linear response as in the non-diffusive network with homogeneous targets, with an R^2 value of 0.38.

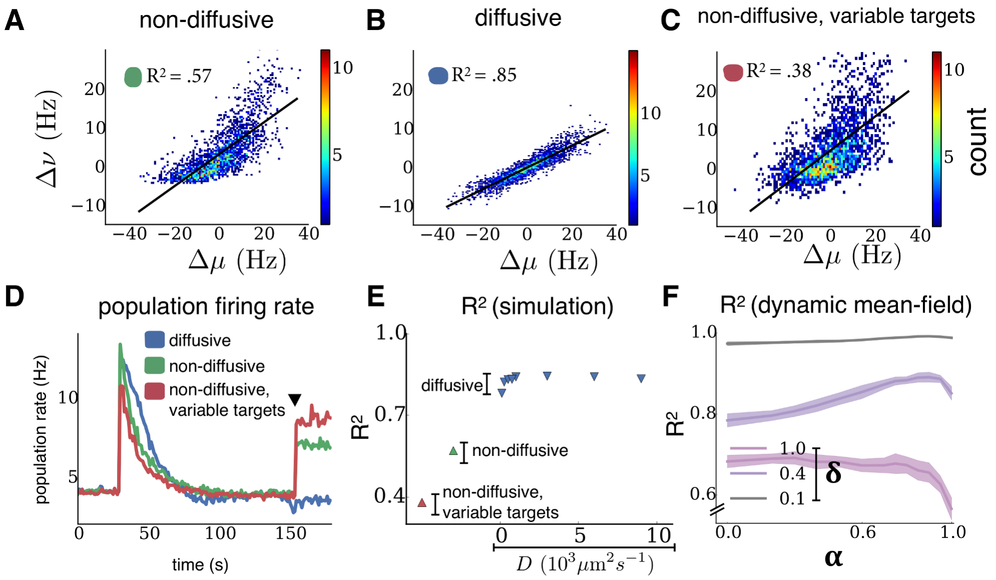

Figure 3.5: Diffusive homeostasis enables linear network responses. **(A-C)** Firing rate changes $\Delta\nu$ of all neurons following input changes $\Delta\mu$. Black lines show linear fits, with corresponding R^2 values inset. **(D)** Population activity before and after input change (black triangle). **(E)** Linearity of the population response to a change of inputs as the diffusion coefficient D is varied ($D = 1000 \mu m^2 s^{-1}$ in panel B). **(F)** Linearity of the population response to a change of inputs in the mean-field analysis as α is varied, shown for different input distribution widths δ. Shaded regions correspond to one standard deviation, averaged over 25 independent network trials for each value of δ.

A consequence of the asymmetry in responses to input changes for networks with non-diffusive homeostasis was that the population rate increases upon regenerating inputs, despite the fact that mean input to the network remained unchanged (Fig. 3.5D). This did not occur for networks with diffusive homeostasis, suggesting that these networks are more adept at maintaining a target level of activity in conditions where external inputs are dynamic and fast-changing. Crucially, the benefits of a diffusive homeostatic signal can be achieved by a relatively broad range of values for the rate of diffusion, D, indicating that the effects we describe are robust to precise parameter choices (Fig. 3.5E). Increasing the rate of NO decay, λ (see Methods), has a similar effect to decreasing D (Fig. 3.6)

This difference in responses to input changes could again be reproduced in the dynamic mean-field approach. This allowed us to characterize population responses

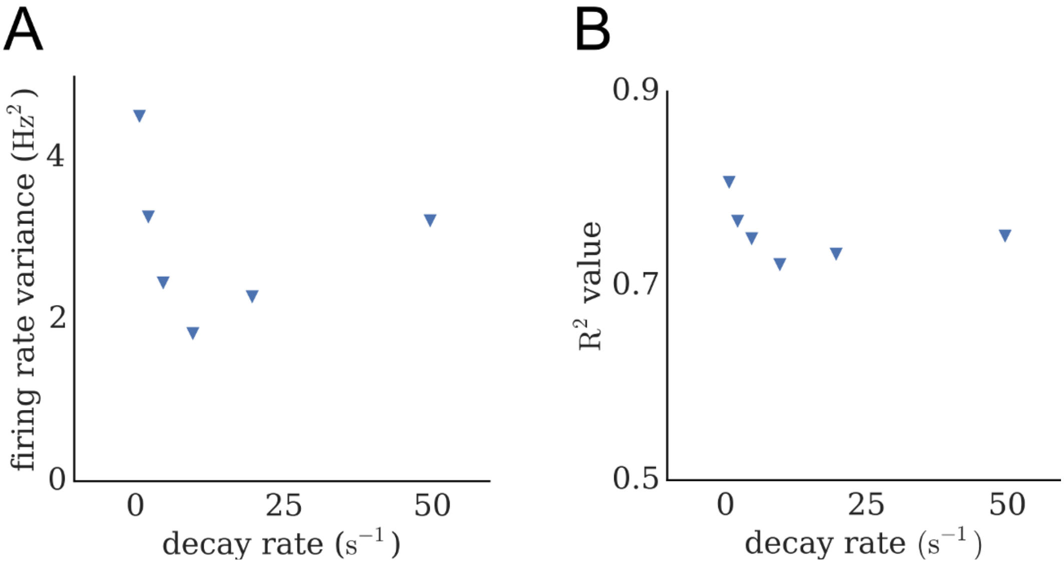

Figure 3.6: Network response properties as the rate of NO decay is varied. **(A)** Variance of the steady-state firing rate distribution as the rate of NO decay, λ, is varied. **(B)** Linearity of the population response to a change of inputs as the rate of NO decay is varied.

across different effective diffusive ranges, using the R^2 value from a linear regression as a measure of response linearity. Fig. 3.5F shows R^2 values across a range of different input distribution widths, δ, as α is varied to model different diffusion coefficients (see Methods). This revealed a dependency on δ: While values of $\alpha \sim 1$ exhibited the best response for smaller δ, hence cases where the inputs are rather narrow, the optimal α decreased as δ increased, as well as the overall response linearity. This dependence on input width can be explained by considering the manner in which a population of neurons with a distribution of dynamic ranges span a range of inputs. If this range of inputs is small, then all neurons will span it regardless of their dynamic range (determined by their firing threshold), hence the high values of R^2 for $\delta = 0.1$. For an intermediate range of inputs, neurons whose dynamic range is best adapted to the average input are most responsive. Note that this does not mean that they have the highest firing rate, but that they change their firing rate more in response to a change in input. This is achieved by increasing α. If the range of inputs is very large ($\delta = 1.0$), R^2 values are low since the dynamic ranges of the population cannot span the inputs. This effect is stronger at high α, as firing thresholds are more correlated, and the dynamics range of most neurons cannot capture the full input variance.

Since connection probability falls off with spatial distance in cortical networks (Holmgren et al., 2003), we additionally simulated recurrent networks featuring such connectivity profiles. These networks exhibited qualitatively similar behavior under diffusive and non-diffusive homeostasis compared to networks without any spatial dependence in connectivity (Fig. 3.7). Spatial dependence in the connection probability between two neurons was introduced as $P_c(d) = \epsilon\, e^{\frac{-d^2}{2s^2}}$, where d is the Euclidean distance between the neurons and s is a constant defining the connectivity range of the network. 2D positions on the torus are bounded such that $x, y \in (0, 1)$. Given a diffusive range of 0.1 mm, values for s were therefore set as 0.05, 0.1, and 0.5. The ratio of s and the diffusive range was defined as ρ, which had values of 0.5, 1.0 and 5.0.

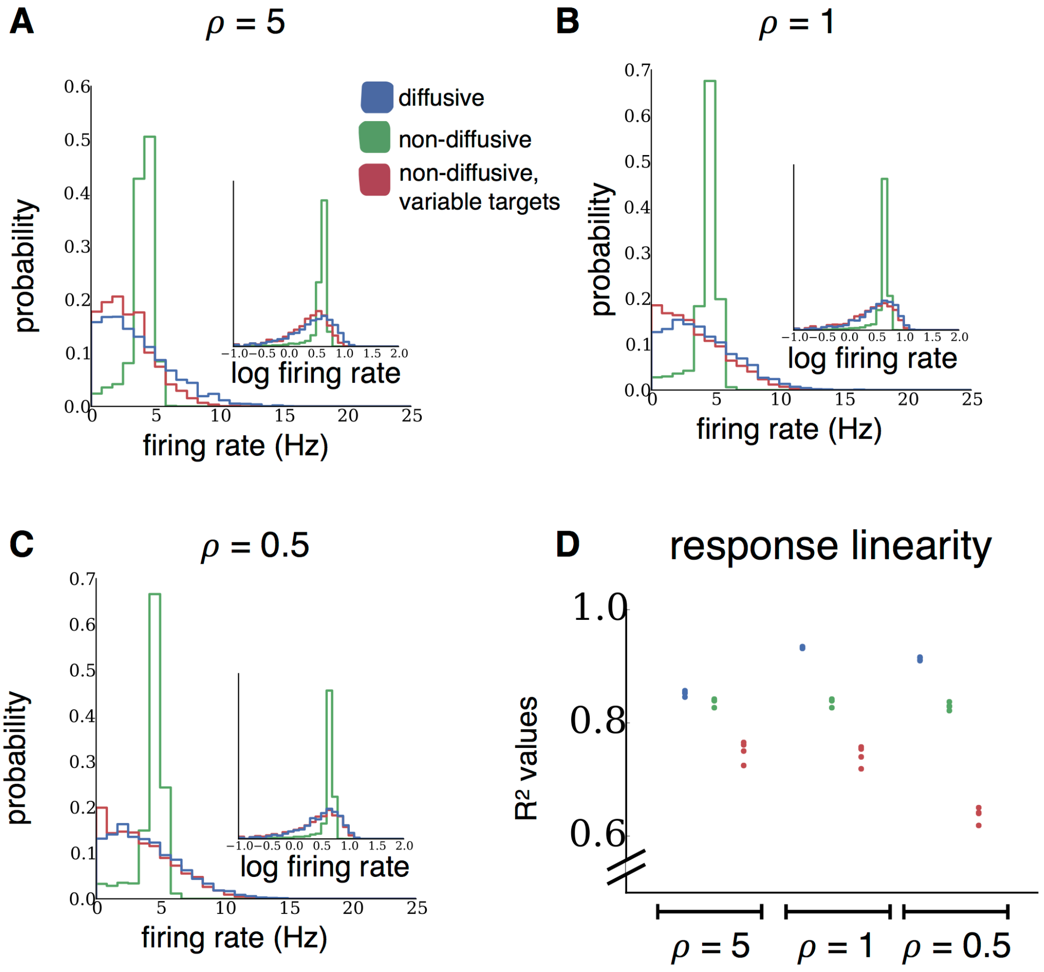

Figure 3.7: Linearity of network responses in networks with spatially restricted connection probabilities. **(A-C)** ρ, the ratio of the connectivity range and the diffusive range, is varied across a wide range of values (ρ = 5.0, 1.0, 0.5). **(D)** Each point represents the R^2 value of a linear fit as in 3.5A-C, for one network.

Up until this point we have presented diffusive and non-diffusive homeostatic mechanisms as dichotomies, which has enabled a clear investigation of their distinct effects on network properties. However, it is more biologically relevant to investigate networks in which both mechanisms are simultaneously active. Fig. 3.8 shows that the increased neural heterogeneity and response linearity observed in networks with diffusive homeostasis are also present in networks with both diffusive and non-diffusive homeostasis, and that the degrees of neural heterogeneity (Fig. 3.8A) and response linearity (Fig. 3.8B) are determined by the relative timescales of these mechanisms (see Methods). As the ratio of timescales of non-diffusive homeostasis to diffusive homeostasis is increased (i.e. as non-diffusive homeostasis becomes slower than diffusive homeostasis), the network goes from narrow steady state firing rate distributions to broad, and exhibits an increase in response linearity, thus becoming more similar to networks with only diffusive homeostasis.

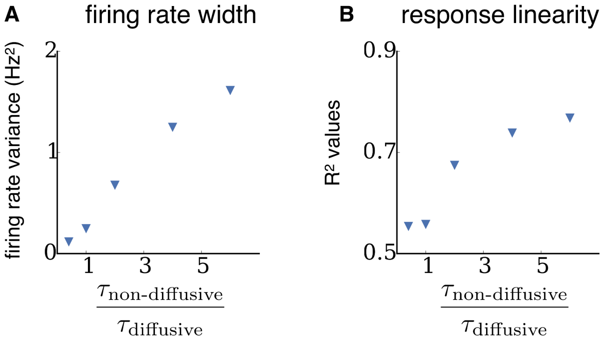

Figure 3.8: Properties of networks with simultaneous diffusive and non-diffusive homeostasis are determined by relative timescales.**(A)** Variance of the steady-state firing rate distribution as the ratio of the non-diffusive homeostasis timescale ($\tau_{\text{non-diffusive}}$) to the diffusive homeostasis timescale ($\tau_{\text{diffusive}}$) is increased in networks with both of these mechanisms simultaneously active. **(B)** Linearity of the population response to a change of inputs as the ratio of the $\tau_{\text{non-diffusive}}$ to $\tau_{\text{diffusive}}$ is increased.

Overall, these results suggest that networks undergoing diffusive homeostasis are better suited to linearly represent a range of inputs. We investigated this by presenting the networks with time-varying inputs after freezing homeostasis. Groups of excitatory neurons received additional inputs which were randomly and independently generated after fixed time intervals (see Methods). Fig. 3.9A shows the representation of such a time-varying input pattern (dotted black line) for each network (colored lines). Networks which have undergone diffusive homeostasis were capable of tracking this input significantly better than their non-diffusive counterparts, as characterized by the RMS error between the network response and input pattern (0.12 for diffusive homeostasis; 0.23 and 0.19 for non-diffusive homeostasis with uniform and variable targets, respectively; Fig. 3.9B).

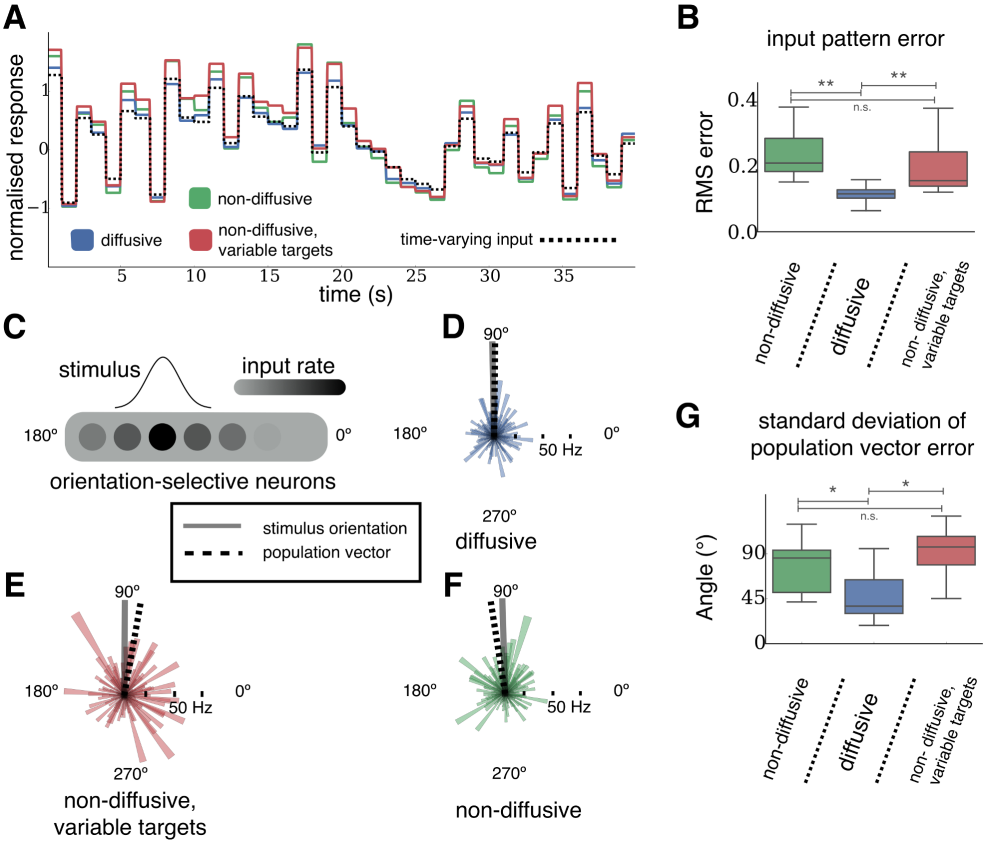

Figure 3.9: Performance advantages of networks with diffusive over non-diffusive homeostasis **(A)** Response of each network to a time-varying input pattern (dotted black line). Colored lines show normalized firing rate deviations from the mean population rate of those neurons receiving inputs. **(B)** RMS errors between the normalized input pattern and normalized response of each network (1000 s pattern presentation and 11 networks in each case). $^{**}p < 0.01$ from a two-sided Kolmogorov-Smirnov test. **(C)** Diagram showing network inputs during an orientation decoding trial. Each neuron is randomly assigned a preferred orientation, and receives external input at a rate given by the stimulus. **(D-F)** Example response of a population of orientation-selective neurons to a stimulus at an orientation of $90°$ (grey line), for networks with each type of homeostasis. Individual neural responses and their preferred orientation are given by the radii and direction of the colored areas respectively. Orientation decoded using the population vector is shown by the dashed line. **(G)** Standard deviation of errors in the orientation of the population vector in response to a stimulus (100 trials for 24 networks in each case). $^{*}p < 0.05$ from a two-sided Kolmogorov-Smirnov test. The box encompasses the inter-quartile range and the whiskers extend to 1.5 times the inter-quartile range in all boxplots.

We can explore these differences further by constructing a simplified task in which a population of orientation-selective neurons respond to the orientation of a stimulus (see Fig. 3.9C-F , Methods). This is not intended to represent circuits which perform this task in the brain, but to serve purely as a demonstration of the relative merits of linear and non-linear network responses.

Neurons in the network are randomly assigned a preferred stimulus orientation, independent of their spatial position. A stimulus of a certain orientation can then be presented to the network by varying the external input rates of each neuron, with neurons whose preferred orientation is closest to the stimulus orientation receiving the highest input rate. The stimulus orientation can be decoded from the network by taking the vector average of the stimulus response across all neurons. The orientation of this vector average, or population vector, is the decoded stimulus orientation. Networks with linear responses perform better than those with non-linear responses in decoding stimulus orientation, as measured by the standard deviation of errors in the orientation of the population vector compared to the stimulus orientation (41°, 63° and 72° for diffusive homeostasis, non-diffusive, and non-diffusive with variable targets respectively, Fig. 3.9G).

3.4 DISCUSSION

Neural homeostasis is commonly thought of as a local process, where neurons individually sense their activity levels and respond with a compensatory change if activity changes. Here we investigated a complementary mechanism, where homeostasis is mediated by a diffusive molecule such as NO that acts as a non-local signal. Using a generic recurrent network model, we show that this form of homeostasis can have unexpected consequences. First, we found that it enables and maintains substantial population heterogeneity in firing rates, similar to that observed experimentally in intact circuits (Wohrer et al., 2013), and that input heterogeneities can be preserved in the population activity. Second, the specific form of neural heterogeneity brought about by diffusive homeostasis is particularly suited to support linear network responses over a broad range of inputs. It is important to note that this behavior differs from that of networks where heterogeneity is simply introduced by randomly assigning a different target to each neuron. These results predict that disrupting neural diffusive NO signaling can affect perceptual and cognitive abilities through changes of neural population responses. While other non-diffusive homeostatic mechanisms would continue to stabilize neural activity, the lack of a signal related to the average population activity may disrupt the flexible maintenance of firing rate heterogeneity, and as a result the ability to represent network inputs.

Mean-field analysis revealed that these differences are essentially due to the diffusive messenger providing each neuron with a combination of the average network activity and its own activity as the homeostatic signal. Diffusion of the signal from highly active neurons causes a reduction in the activity of their neighbors, such that firing rates of highly active neurons do not have to be completely reduced in order for the population to achieve a target rate. As a consequence, diffusive homeostasis furnishes a network with an efficient way of flexibly maintaining heterogeneity of firing rates. These effects can also be understood by considering the neural transfer functions, as illustrated in Figs. 3.10A-B, which provides an intuitive explanation for the differences in firing rate distributions observed under diffusive homeostasis (Roxin et al., 2011; Ermentrout, 1998). For non-diffusive homeostasis the transfer function of each neuron is brought to center around its input, leading to a narrowing of the firing rate distribution. Diffusive homeostasis decorrelates the input and threshold of individual neurons, resulting in a population of neurons residing along the entire transfer function. This preserves the non-linear shape of the transfer function, causing broad and heavy-tailed firing rate distributions.

Narrow firing rate distributions are an obvious consequence of local homeostatic processes, as for instance shown recently with homeostasis implemented as local synaptic metaplasticity (Zenke et al., 2013). This is in apparent conflict with the growing body of experiments documenting broad and heavy-tailed distributions of firing rates in cortex (Wohrer et al., 2013). One could argue that a straightforward explanation is a process, for example genetic or developmental, which randomly assigns neurons heterogeneous homeostatic targets. While we show here that this can result in broader firing rate distributions, we also found that this generally leads to networks with a mismatch between the neural dynamic ranges and input statistics, which in turn limits the responsiveness of the network.

A striking feature of diffusive homeostasis is the lack of requirement for any such distribution of homeostatic targets, as the diffusive signal can be effectively exploited

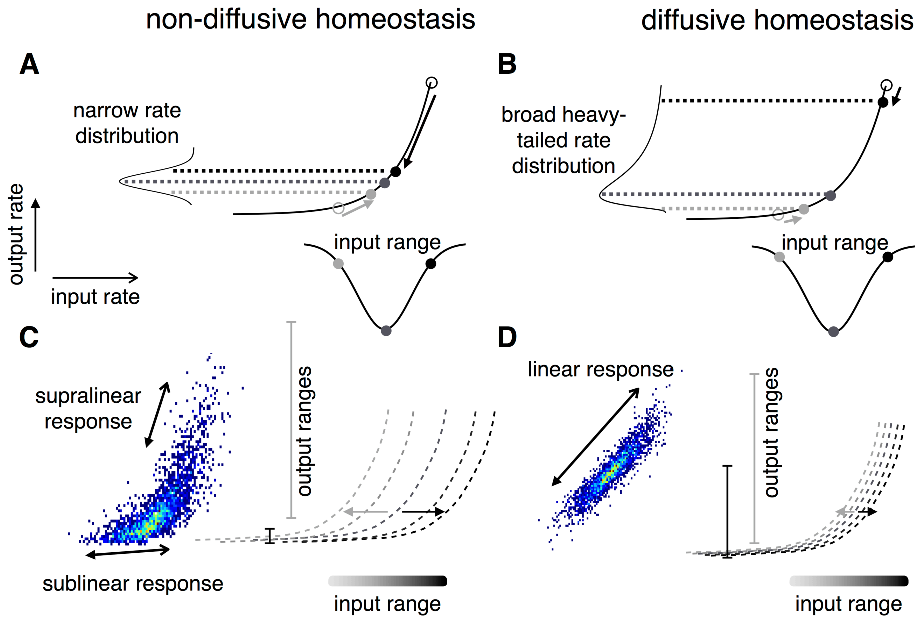

Figure 3.10: Comparison of the effects of diffusive and non-diffusive homeostasis on neural transfer functions. **(A)** For non-diffusive HIP the transfer function of each neuron is brought to center around its input in order to avoid response saturation or runaway excitation. Arrows show the action of HIP on neurons (circles) with a given input (adapted from Roxin et al. (2011)). **(B)** Diffusive homeostasis decorrelates the input and threshold of individual neurons, resulting in a population of neurons residing along the entire transfer function. The non-linear shape of the transfer function causes broad and heavy-tailed rate distributions observed with diffusive homeostasis. **(C-D)** Transfer functions following homeostasis of neurons receiving small (light grey) to large (dark grey) input are shown by the dotted lines. Following an instantaneous input change, the output ranges across the entire range of inputs are shown as vertical grey lines, with the shade of grey corresponding to the neuron's previous input. Networks with non-diffusive homeostasis (C) exhibit response saturation (dark grey line) and superlinear responses (light grey line), while diffusive homeostasis (D) causes transfer functions to shift towards the center of the input distribution, leading to approximately linear responses.

through providing a context for heterogeneity - neurons which maintain a significantly higher firing rate than the rest of the network also synthesize a higher level of the diffusive signal, thus ensuring that their deviation from the average firing rate is counterbalanced by lowering neighboring neurons' firing rates. This mechanism essentially allows neurons to differ in activity from the population as long as the population as a whole provides some compensation for these deviations. Moreover, this mechanism is compatible with the recent finding that a minority of cells were found to consistently be the most highly active and informative across brain states (Mizuseki and Buzsáki, 2013). While non-diffusive homeostasis would have a disruptive effect on such a 'preserved minority' of neurons by reducing their activity towards those of the less active majority, diffusive homeostasis provides a substrate for maintaining their differentiated activity.

A significant distinction between the effects of diffusive and non-diffusive homeostasis appears when network responses to rapidly changing input are considered (Fig. 3.5). We show that networks with diffusive homeostasis represent input changes more faithfully than those with non-diffusive homeostasis. Saturation of neurons' responses to large changes are observed in networks without diffusion - this effect is further illustrated in Fig. 3.10C-D.

Across a spatially homogeneous network, diffusing signals act to effectively shift the transfer function of each neuron towards the average network input, ensuring that neurons are responsive across the entire range of inputs presented to a network. This is in contrast to networks with non-diffusive homeostasis, in which individual neurons are only responsive in a range around their current input. Moreover, the asymmetric response of networks with non-diffusive homeostasis causes the average network activity to increase after fast input changes, while it is constant for a network with diffusive homeostasis (Fig. 3.5D). The latter case is consistent with observations that mean population firing rates are preserved across novel and familiar environments and across different episodes of slow-wave sleep (Hirase et al., 2001; Slomowitz et al., 2015)

Networks with diffusive homeostasis have an improved ability to accurately track time varying inputs (Fig. 3.9A-B) as a direct consequence of their linear responses. Beneficial effects of neural heterogeneity for population coding have been suggested before (Tripathy et al., 2013; Shamir and Sompolinsky, 2006), but here we find that the broad linear response regime maintained by diffusive homeostasis further improves network performance. This improvement in network performance is also observed in a simplified stimulus orientation decoding task (Fig. 3.9C-G). Networks with diffusive homeostasis perform better than those with non-diffusive homeostasis when a population vector is constructed from the neural responses in order to decode stimulus orientation (Figure 3.9G-H). Although there exist alternative methods for decoding stimuli, the population vector has been shown to exhibit performance close to the optimal maximum likelihood procedure for broad tuning, as was used in our example (Seung and Sompolinsky, 1993).

The consequences of diffusive and non-diffusive homeostasis coexisting were also explored, by implementing these mechanisms simultaneously in a single network (Fig. 3.8). Stable homeostatic activity could be robustly maintained, with the resulting network behavior depending on the relative timescales of the non-diffusive and diffusive mechanisms. If non-diffusive homeostasis acted faster than diffusive homeostasis, the network exhibited a narrow rate distribution and a low responsiveness to input changes. Conversely, if diffusive homeostasis acted faster than non-diffusive homeostasis, the network exhibited broad firing rate distributions and linear responses to input changes. This is a plausible scenario, as NO modulation of ion channels occurs over a timescale of 15 minutes (Steinert et al., 2011), while other homeostatic processes which require transcriptional changes occur over a timescale of hours to days (O'Leary et al., 2014). These results reflect what is observed as α is varied in the dynamic mean-field analysis, as local and global homeostatic mechanisms are simultaneously active for values in the range $0 < \alpha < 1$.

It is important to note that modeling HIP as a force acting on the threshold of an integrate-and-fire neuron in order to achieve a target firing rate is a significant simplification. More physiologically realistic descriptions of homeostatic processes reveal the complex relationship between ion channel concentrations and the regulation of a wide range of neural activity (O'Leary et al., 2014). Moreover, a number of previous studies have explored the effects of volume transmission on network dynamics, including its potential in implementing a winner-take-all function (Kohonen, 1993), the ability of a diffusive signal to reflect the average activity of a group of neurons (Ott et al., 2007), and the role of another diffusive neurotransmitter, TNFα, in epileptogenesis (Savin et al., 2009). Here, we add a functional interpretation by exploring its effects on neural heterogeneity and responsiveness within a network.

While NO is involved in a wide variety of neural processes throughout development and learning (Nikonenko et al., 2013; Tamagnini et al., 2013; Son et al., 1996), these were ignored throughout for the sake of simplicity and tractability. Nonetheless, the impaired performance of nNOS knock-out mice in cognitive tasks (Weitzdoerfer et al., 2004) and the prevalence of epilepsy following nNOS inhibition (Del-Bel et al., 1997) could be linked to diminished homeostatic control of neural excitability. Finally, the outcome of this study is not necessarily confined to NO, and could equally apply to other diffusive neurotransmitters observed in the brain such as hydrogen sulfide and carbon monoxide (Wang, 2002). Indeed, we conclude that it demonstrates the potential role of diffusive neurotransmitters as an economical and reliable signal of activity across a population of neurons.

A logical avenue of investigation to pursue from our current results is how Hebbian synaptic plasticity might interact with the different homeostatic mechanisms in the networks we have implemented. This will be the subject of the next chapter.

4

INTERACTIONS BETWEEN HOMEOSTATIC AND HEBBIAN PLASTICITY

CHAPTER SUMMARY

Continuing on from our investigation of diffusive homeostasis in recurrent networks, we explore whether the distinctions between diffusive and non-diffusive homeostasis are conserved if Hebbian plasticity is also active in the network. We find that these distinctions are still present when additive STDP is implemented; indeed, the differences in response linearity between diffusive and non-diffusive homeostasis are amplified in networks with plastic synapses. Differences in the synaptic weight dynamics also emerge between networks with diffusive and non-diffusive homeostasis. Non-diffusive homeostasis leads to more fluctuations in synaptic weights during spontaneous activity. Additionally, networks with diffusive homeostasis are more capable of forming distinct memories in response to structured external input, and memories inserted into these networks have a longer lifetime than those in networks with non-diffusive homeostasis.

4.1 INTRODUCTION

4.1.1 *Spike-timing-dependent plasticity*

There is a very broad range of models of STDP, each with their own advantages, disadvantages, and degree of biological realism (Markram et al., 2012). While earlier models of STDP and their dynamics are well-characterised, recent models claim to be more biologically plausible by incorporating a wider range of experimental observations. Early models typically fall into two categories; those in which the synaptic weight update at each spike is independent of the synaptic weight (e. g. additive STDP, Song et al. (2000)), or those in which there is a weight-dependence (e. g. mul-

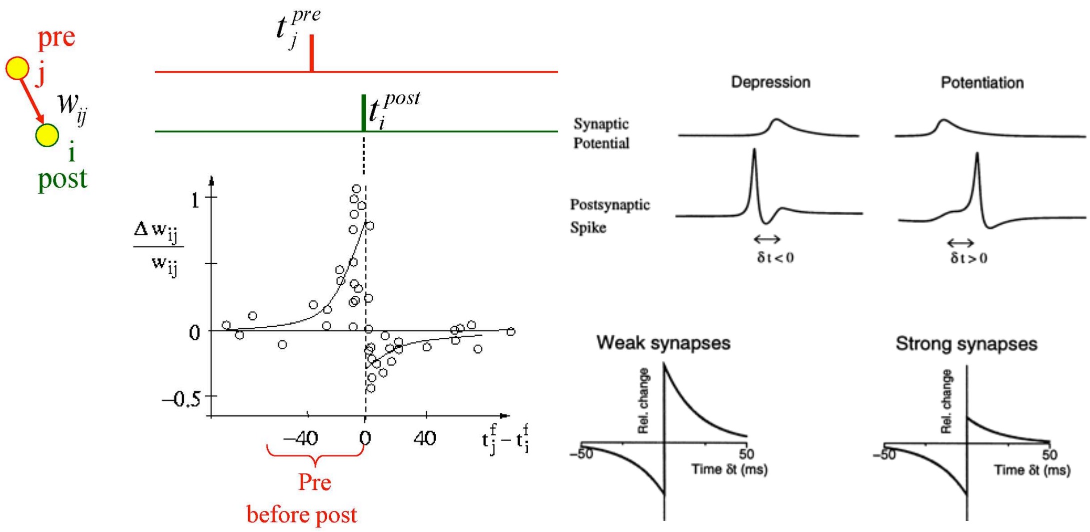

Figure 4.1: Illustration of the relative synaptic weight update following a pre- and post-synaptic spike, and how this depends on the relative timing between both spikes (left). The weight dependence of a multiplicative STDP rule is also shown (right). Diagram from Sjöström and Gerstner (2010) (left) and Van Rossum et al. (2000) (right).

tiplicative STDP, Van Rossum et al. (2000)). Additive STDP leads to synaptic weights which must be bounded in order to prevent ever-potentiating synapses, therefore leading to bimodal synaptic weight distributions (Song et al., 2000). When the multiplicative weight update is designed so that depression becomes stronger compared with potentiation as the synaptic weight increases (see Figure 4.1), this leads to unimodal weight distributions (Van Rossum et al., 2000). These weight distributions are closer to those observed in experiments (Song et al., 2005b), although synaptic weights undergoing multiplicative STDP are less stable than those undergoing additive STDP (Billings and van Rossum, 2009). Tetzlaff et al. (2011) show however that combining an STDP rule with a second-order weight dependence and synaptic scaling guarantees synaptic weight stability. Later models of STDP explain the frequency-dependence of LTP and LTD induction, by introducing voltage-dependence (Clopath et al., 2010), or by using a calcium-based synaptic model (Graupner and Brunel, 2012). Models of STDP have also been used demonstrated to be useful for robust synchronisation and sequence learning (Nowotny et al., 2003; Zhigulin et al., 2003).

4.1.2 *Interactions of homeostatic and Hebbian plasticity in networks*

Studying the interactions of homeostatic plasticity and STDP in recurrent networks is quite problematic as there are multiple timescales involved, and issues arise with stability and firing rate oscillations (Remme and Wadman, 2012; Harnack et al., 2015). Until recently, most theoretical investigations of the effects of plasticity on recurrent network dynamics were conducted using rate-based model neurons (Lazar et al., 2009; Naudé et al., 2013). These studies demonstrated that homeostatic intrinsic plasticity can act in synergy with Hebbian plasticity in order to enhance the dynamic regime of a recurrent network. Zenke et al. (2013) have argued that homeostasis must act on a relatively fast timescale in order to counteract runaway excitation following Hebbian plasticity, although Harnack et al. (2015) demonstrate the potential for oscillatory dynamics arising due to network effects when fast homeostasis is implemented in a recurrent network. Toyoizumi et al. (2014) have proposed that a stable steady state in the synaptic weight and firing rate dynamics may be achieved by a combination of Hebbian and homeostatic processes in which the total synaptic strength is determined through a product of both factors, although in this case the homeostatic mechanism is a form of synaptic metaplasticity which adjusts the threshold between LTP and LTD, much like the BCM rule (Bienenstock et al., 1982).

4.2 DIFFUSIVE HOMEOSTASIS AND STDP

In the networks described in chapter 3, we use static and uniform synaptic weights for recurrent connections. We will now take the networks with the exact same setup and parameters, and consider whether the observed properties of diffusive homeostasis are altered by the presence of plastic synaptic weights, in particular when Hebbian spike-timing-dependent plasticity (STDP) is introduced. We will only study the effect of recurrent excitatory-excitatory plasticity in our network, with external, excitatory-inhibitory, inhibitory-excitatory, and inhibitory-inhibitory synaptic weights remaining static. Inhibitory plasticity does however exist (Castillo et al., 2011), and has been shown to play a role in balancing excitation and inhibition in recurrent networks (Vogels et al., 2011; D'amour and Froemke, 2015).

A spike-timing dependent plasticity rule, as described in Song et al. (2000), is implemented in each recurrent excitatory-excitatory synapse. Both potentiation and depression are additive in this rule, with no weight dependence. For each nearest neighbor pair of pre- and post-synaptic spikes separated by a time Δt (see Figure 4.1), the synaptic weight is updated by a value Δw given by

$$\Delta w = \begin{cases} A_{+}\exp(\Delta t/\tau_{+})g_{\max}, & \text{if } \Delta t < 0. \\ \\ -A_{-}\exp(-\Delta t/\tau_{-})g_{\max}, & \text{if } \Delta t \geqslant 0. \end{cases} \tag{4.1}$$

Above, τ_+ and τ_- denote the timecourse over which potentiation and depression occur respectively, while A_+ and A_- denote the relative strengths of potentiation and depression. Weights are bounded by $0 < w < g_{\max}$, which we expect will result in a bimodal weight distribution. Initial weights are generated from a Gaussian distribution, given by $w_0 \sim \mathcal{N}(7.5, 2.5^2)$ nS, and $g_{\max} = 10$ nS. Depression is set to be slightly stronger than potentiation ($A_+ < A_-$) in order to prevent runaway potentiation, thus ensuring that irregular firing is maintained within a reasonable range of rates. The above equations describing the STDP implementation are solved numerically by the Brian simulator (Goodman and Brette, 2008).

We simulate networks with both STDP and homeostasis active until synaptic weight and firing rate distributions reach a steady state, which takes around 500 s. The mean synaptic weight over time for networks with different types of homeostasis each is shown in Figure 4.2. The external input in networks with STDP are given by $\mu_i \sim \mathcal{N}(10, 10^2)$ Hz, and $J_{\text{ext}} = 40$ nS, $C = 250$. STDP and homeostasis are frozen after 2000 s in order to facilitate measurements of the steady state for Figure 4.3A-B, and to measure the network response linearities in Fig. 4.3C. Steady-state firing rate distributions for Fig. Figure 4.3Bi are obtained as in the procedure for Fig. 3.1D. The autocorrelogram in Fig. 4.3Biv is obtained by measuring the average rate of coincident spikes in a temporal bin of width 2.5 ms at each time lag, averaged across all neurons.

Network response linearities are obtained as in the procedure for Figs. 3.5A-D. The R^2 values for networks with shuffled, static synaptic weights are obtained by taking the steady-state synaptic weight matrix from a network with STDP and without any homeostasis, randomly shuffling this final weight matrix, and using these weight

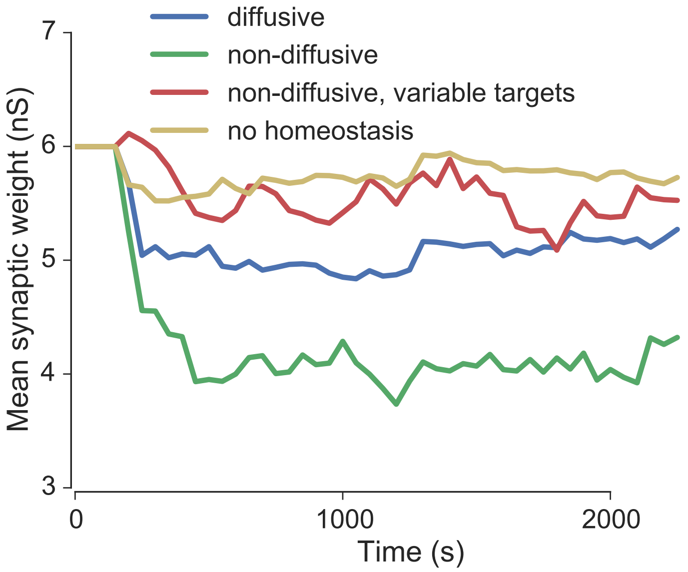

Figure 4.2: Evolution of the mean synaptic weight over time for networks with different forms of homeostasis. Initial weights are generated from a Gaussian distribution and both STDP and homeostasis are turned on after 200 s. External input rates to the network remain constant throughout.

matrices in new networks for each different case of homeostasis, without STDP active. Using shuffled weight matrices obtained from networks with other forms of homeostasis present does not qualitatively affect the results.

4.2.1 *Properties of diffusive homeostasis are conserved in networks with Hebbian plasticity*

As seen previously in chapter 3, firing rate distributions are broader in networks with diffusive homeostasis (Fig. 4.3Bi). Broad distributions can also be achieved by introducing variability in homeostatic targets. Spiking activity remains asynchronous after STDP, as shown by the distribution of inter-spike intervals and the spike autocorrelograms, although STDP causes weakly synchronous activity in networks without any form of homeostasis (Figs. 4.3Bii-iv)(Vogels and Abbott, 2005). The additive STDP rule leads to a bimodal distribution of synaptic weights (Fig. 4.3A), as previously reported (Song et al., 2000).

STDP amplifies the differences in response linearity that was observed between homeostatic cases in chapter 3. Inputs to each neuron are regenerated from the same distribution presented during plasticity, and the corresponding change in output rate is compared to the change in input rate, as in Figs. 3.5A-C. While the response linearity, given by the mean R^2 value, for networks with diffusive homeostasis is 0.16, networks with non-diffusive homeostasis exhibit much lower mean values of 0.01 and 0.02, for uniform and variable homeostatic targets respectively (Fig. 4.3C. Diffusive homeostasis has significantly higher R^2 than non-diffusive homeostasis, $p < 0.01$, independent 2-sample t-test with Bonferroni corrections). Networks without any homeostasis have a mean value of 0.1. These R^2 values are lower than those from networks without any STDP (Fig. 3.5E), which is likely due to a combination of weaker external input given to these networks (g_{ext} of 40 ns compared to 80 ns), and stronger recurrent excitation received by neurons in these networks due to potentiation during STDP. This is tested by assessing response linearity in networks with static weight matrices obtained by shuffling the steady-state weight matrix of a network which has undergone STDP without any homeostasis. These networks are run for each different homeostatic case until a steady state is reached, and inputs to each neuron are regenerated in order to measure response linearity. While shuffling synaptic weights does increase R^2 values across all networks (Fig. 4.3C, crosshatched bars), indicating that STDP plays a role in decreasing response linearity, they remain lower than in networks from Fig. 3.5E, confirming that the reduced influence of external input compared with recurrent input is largely responsible for this difference. Additionally, the mean negative R^2 value for the network with non-diffusive homeostasis in 4.3C demonstrates an overall decrease in firing rates following input regeneration. This is likely due to STDP depressing weights between neurons that are not coactive before input regeneration but are coactive after, meaning that effective recurrent connectivity drops after input regeneration. This effect could be further explored by using network parameters different from those in chapter 3, so that stronger external input is used and higher firing rates are achieved after input regeneration. We observed qualitatively similar retention of broad firing rate distributions and response linearity with diffusive homeostasis when a weight-dependent update rule was used (not illustrated), which has been argued to lead to more realistic weight distributions (Van Rossum et al., 2000).

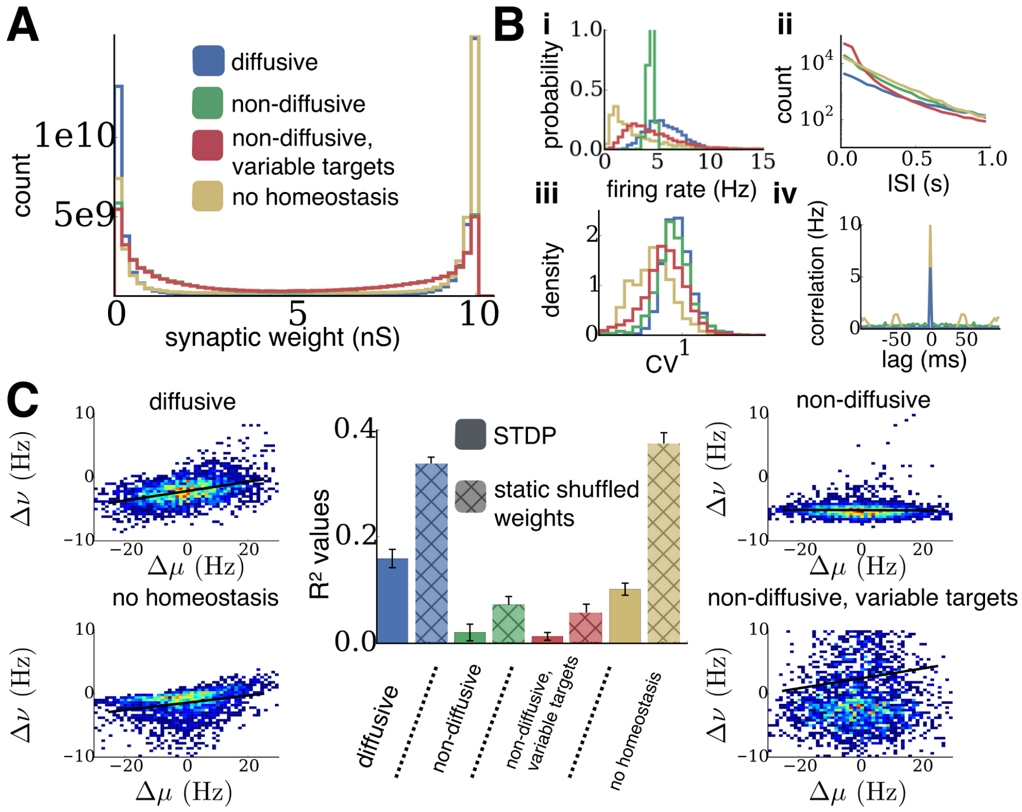

Figure 4.3: Diffusive homeostasis retains its properties in networks with STDP. **(A)** Distributions of steady-state synaptic weights after homeostasis and STDP. **(B)** (i) Distributions of steady-state firing rates after homeostasis and STDP. (ii) Distribution of inter-spike intervals (ISI) at the steady state (log scale). (iii) Distribution of the coefficient of variation (CV) of ISIs at the steady state. (iv) Average autocorrelogram of the network at the steady state, given by the rate of coincident spikes in each time bin. **(C)** Mean response linearity (measured by R^2 values) for networks with STDP and each case of homeostasis (n=9 networks, error bars represent one standard deviation). Crosshatched bars show mean response linearity for networks with each case of homeostasis and without STDP, using weight matrices obtained by shuffling the final weight matrix of networks with STDP and without homeostasis. Surrounding plots show firing rate changes $\Delta\nu$ of all neurons following input changes $\Delta\mu$ for an example network in each case (black line shows linear fit).

4.2.2 *Synaptic weight dynamics*

Since networks with 5000 neurons and 1.25 million plastic synapses requires many days of computational time for each instantiation, we will scale down to networks with 500 neurons, and a recurrent connection probability of 0.2, in order to investigate in detail the dynamics of synaptic weights as STDP interacts with different forms of homeostasis. Note that this computation time is for a 2.3 GHz CPU; a significant speedup to ~ 2X biological real time could be achieved if the simulations were performed on a GPU (Brette and Goodman, 2012; Yavuz et al., 2014). The dynamics of individual synaptic weights and firing rates are shown in Figure 4.4. Synaptic weights are initialised with a uniform value of 5 nS. Networks are run for 250 s initially with only STDP active, after which both homeostasis and STDP is active. Synaptic weights which reach values close to the bounds of 0 nS or 10 nS tend to remain relatively stable for all forms of homeostasis, while synapses with weights in between these two values are less stable. There are no immediately apparent differences in the synaptic weight dynamics for networks with different types of homeostasis.

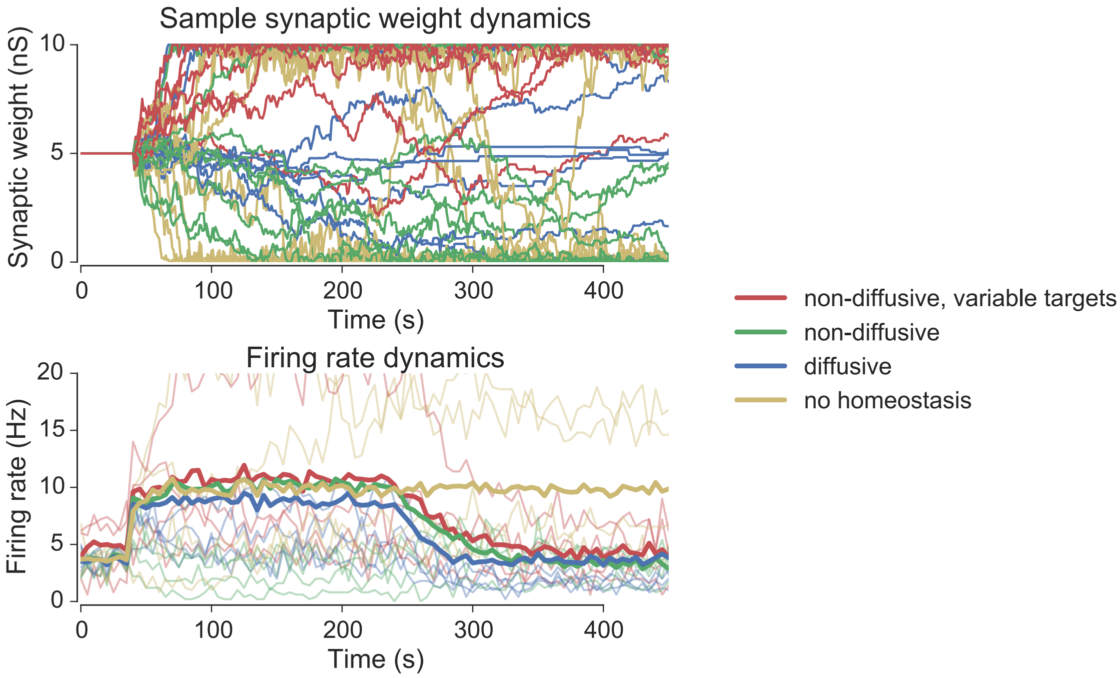

Figure 4.4: The evolution of individual synaptic weights (top) and mean firing rates (bottom, with individual samples shown in lighter colour) in networks with different forms of homeostasis. The network is run with only STDP active from 50 - 250 s, and homeostasis becomes active after this (with STDP remaining active). Synaptic weights are sampled every 1 s, and firing rates every 5 s. Initial weights for all synapses are 5 nS.

However, differences in the stability of synaptic weights under different forms of homeostatic control appear under closer investigation. Figure 4.5 shows the amount of fluctuations in the synaptic weights during homeostatic regulation. Networks with either no homeostasis or diffusive homeostasis have synapses which fluctuate significantly less than those in networks with non-diffusive homeostasis. The fluctuations are measured for each individual synaptic weight by calculating the absolute difference between its value at 250 s, just as homeostasis is turned on, and at 750 s, after the homeostatic steady state has been reached. While just over 6 % of synaptic weights which were in the upper quartile at 250 s (i. e. had values >7.5 nS) fell into a lower quartile by 750 s for networks without homeostasis or with diffusive homeostasis, this proportion increased to 13 % for networks with non-diffusive homeostasis, and 16 % for networks with non-diffusive homeostasis and variable targets (Figure 4.5). This suggests that non-diffusive homeostasis has a destabilising effect on synapses which are expected to be stable otherwise.

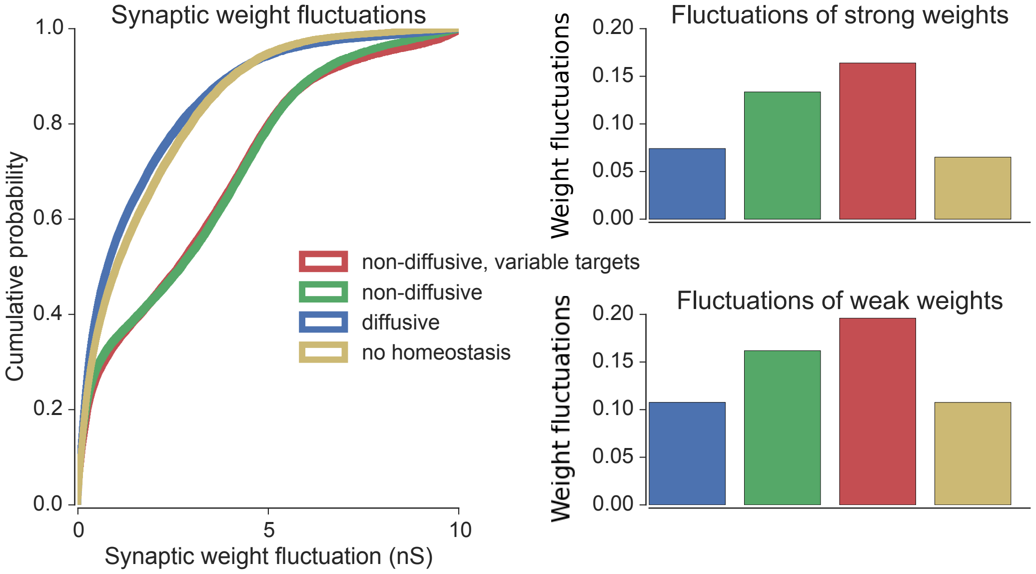

Figure 4.5: Distribution of fluctuations in the synaptic weights during homeostasis (left). Shown is a cumulative distribution of the absolute change between 250 s and 750 s for each synaptic weight. Ratio of synapses with strong (>7.5 nS) weights at 250 s which remain strong at 750 s is shown (right, top), as well as the ratio of synapses with weak (<2.5 nS) weights at 250 s which remain weak at 750 s (right, bottom).

4.2.3 *The effect of homeostasis on memory formation*

We have shown that different forms of homeostasis have varying degrees of influence on synaptic weight fluctuations, with non-diffusive homeostasis causing more interference than diffusive homeostasis. As such it is likely that networks with non-diffusive homeostasis will interfere more than diffusive homeostasis during the formation and maintenance of memories. We now wish to assess the effects of the different forms of homeostasis on networks which have already undergone some form of 'learning'. In order to test this we will increase the rates of external input to a group of 100 excitatory neurons in the network of 500 neurons. Although this is a highly simplified paradigm, the structured differences in the external input should be reflected in the synaptic weights of the two groups within the network; the group which receives elevated external input, and the rest of the network. The elevated input rates are given by $\mu_i \sim \mathcal{N}(30, 10^2)$ Hz, whereas the inputs to the rest of the network remains at $\mu_i \sim \mathcal{N}(10, 10^2)$ Hz. As before, the network is initially run with only STDP active from 50 - 250 s, after which both homeostasis and STDP are active. The elevated input rate to the group of 100 excitatory neurons is maintained from 50 s onwards.

Figure 4.6 shows the effect of this elevated input on the firing rates of neurons within a network, as well as the effect of subsequent homeostasis. As expected from previous results on retaining input group separability discussed in chapter 3, the group with elevated inputs maintained higher firing rates in networks with diffusive homeostasis, but not in networks with non-diffusive homeostasis (Figure 4.6). The differences in the firing rates between the group with elevated input and the rest of the network can be quantified by the signal-to-noise ratio (SNR), $(\mu_{\text{group}} - \mu_{\text{rest}})/(\sigma_{\text{group}} + \sigma_{\text{rest}})$, where μ and σ correspond to the mean and standard deviation of the firing rates of either group of neurons. As shown in the boxplots in Figure 4.6, the SNR is significantly higher for networks without homeostasis or with diffusive homeostasis than for networks with non-diffusive homeostasis. This measurement is taken at the steady state, after homeostasis has acted on the network. As such, this can be thought of as the ability of a network to retain differences in inputs while both homeostatic and Hebbian plasticity is active, which would be required if a network is to learn these differences in input rates.

We will now consider whether the synaptic weight distributions established through STDP are affected by the type of homeostasis active in these networks (Figure 4.7). During the period when only STDP is active, without any homeostasis, the weight distribution for synapses within the group receiving elevated input becomes differentiated from the weight distribution of synapses within the rest of the network. The distribution of weights within the group is bimodal, with a higher proportion of both very small or very large weights than intermediate weights. Synaptic weights for the rest of the network have more intermediate values, and as a consequence have a less bimodal distribution. This is illustrated in the panel of Figure 4.7 which shows

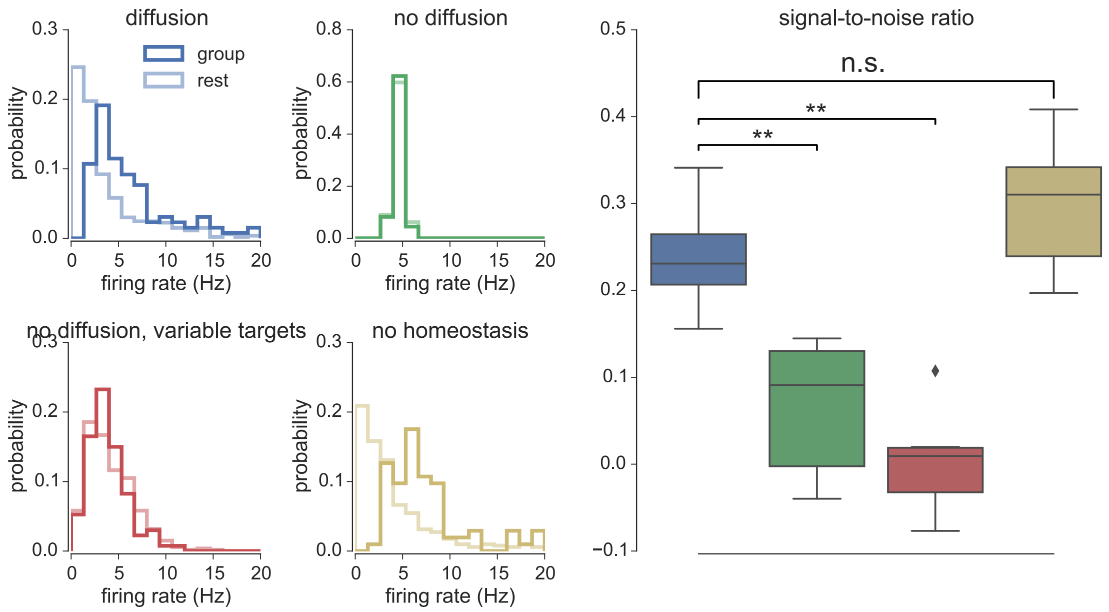

Figure 4.6: Firing rate distributions of neurons which have received elevated external input (dark) compared with neurons from the rest of the network (light). Also shown is the signal-to-noise ratio between the firing rates of these two groups of neurons, for 8 different instantiations of a network in each case (right). ** indicates $p < 0.01$ from a two-sided Kolmogorov-Smirnov test, with Bonferroni correction applied. The box in all boxplots encompasses the inter-quartile range and the whiskers extend to the rest of the distribution, apart from outlier points shown which lie 1.5 times outside the inter-quartile range.

these distributions for a network with no homeostasis, and can be quantified using the bimodality coefficient (BC), defined as $BC = \frac{m_3^2+1}{m_4+3\left(\frac{(n-1)^2}{(n-2)(n-3)}\right)}$ (Pfister et al., 2013; Freeman and Dale, 2013). Here, m_3 is the skewness of the sample distribution, m_4 is the excess kurtosis, and n refers to the number of samples. $BC = 1$ implies a perfectly bimodal distribution, while a uniform distribution has a value of $BC = 0.56$ (Pfister et al., 2013). As can be seen from the boxplots, the BC is significantly higher for synapses within the group receiving elevated input than the rest of the network.

Differences between networks with diffusive and non-diffusive homeostasis can also be observed in the synaptic weight distributions at the homeostatic steady state. While the increased bimodality amongst the group of neurons receiving elevated input is retained for networks with diffusive homeostasis, this difference in bimodality disappears for networks with non-diffusive homeostasis (Figure 4.7). Interestingly, this effect of non-diffusive homeostasis arises due to the synaptic weight distribution of the rest of the network becoming more bimodal with respect to networks without homeostasis, as opposed to synapses in the group receiving elevated inputs becom-

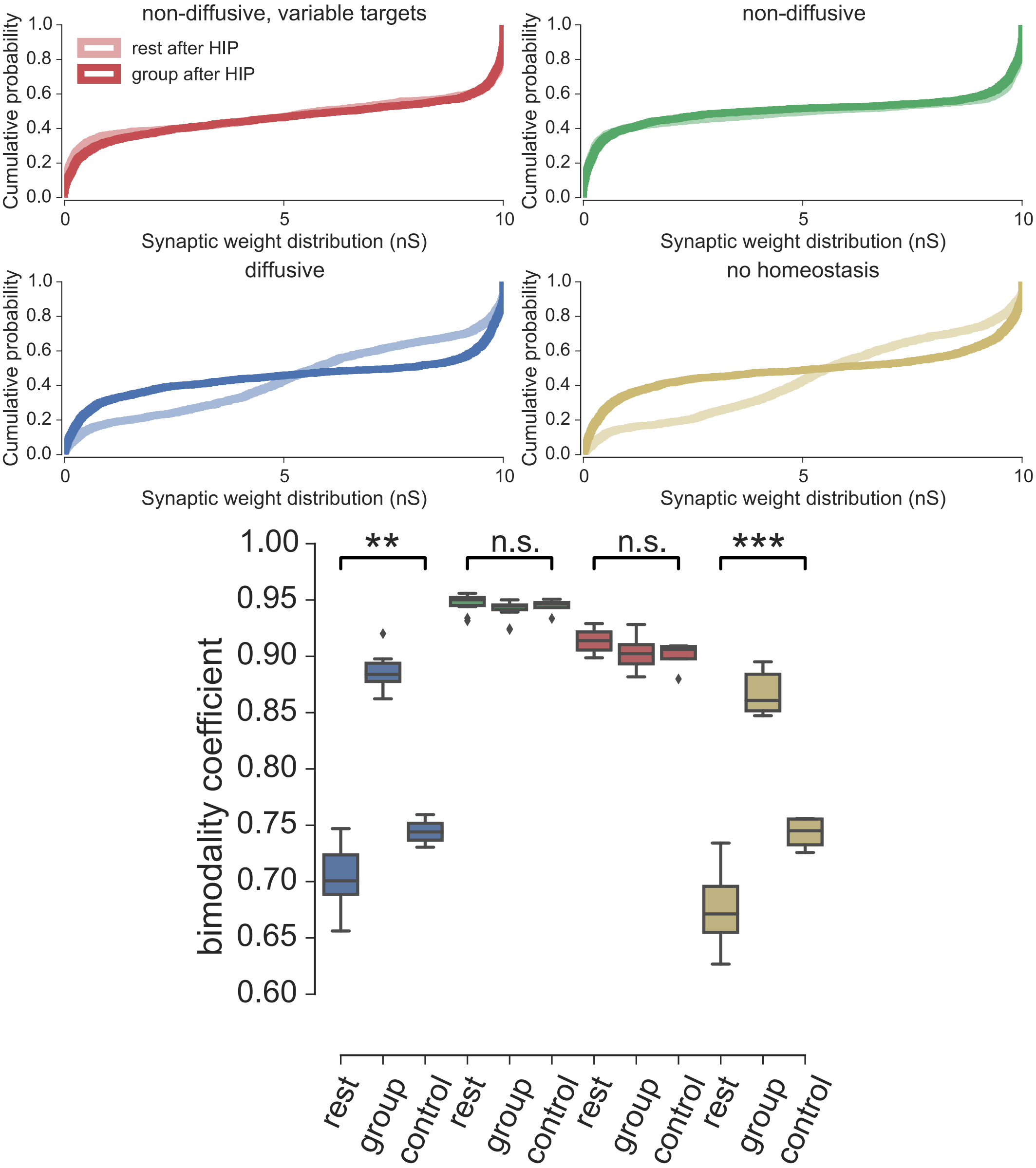

Figure 4.7: The distribution of synaptic weights between neurons which have received elevated external input (dark), and between neurons from the rest of the network (light). Also shown is the bimodality coefficient (BC) of these synaptic weight distributions (below). The different boxplots correspond to BCs for the distribution of synaptic weights between neurons which have received elevated external input ('group'), between neurons from the rest of the network ('rest'), and from a network whose neurons have not received any elevated external inputs ('control'). A uniform distribution has a bimodality coefficient of 0.56 (Pfister et al., 2013; Freeman and Dale, 2013). ** indicates $p < 0.01$ and *** indicates $p < 0.001$ from a two-sided Kolmogorov-Smirnov test, with Bonferroni correction applied. The box in all boxplots encompasses the inter-quartile range and the whiskers extend to the rest of the distribution, apart from outlier points shown which lie 1.5 times outside the inter-quartile range.

ing less bimodal. This results in highly bimodal weight distribution for all synapses in networks with non-diffusive homeostasis ($\mathrm{BC} \gtrsim 0.9$), regardless of whether these neurons are receiving elevated external input. The BCs of these distributions can be compared with the BCs of networks which do not have any structured input (the 'control' boxplots in Figure 4.7). The BC for these control networks without homeostasis or with diffusive homeostasis are lower than the BCs of synapses within groups receiving elevated input in structured networks, and higher than the BCs of synapses within groups which don't receive elevated input in structured networks. This demonstrates the capability that networks with diffusive homeostasis or no homeostasis have to represent structured inputs in their synaptic weight distributions. On the other hand, networks with non-diffusive homeostasis display no significant differences in BCs between networks receiving structured or unstructured inputs Figure 4.7.

These results follow from the inability of networks with non-diffusive homeostasis to retain differences in external input rates, as demonstrated in Figure 4.6. Without any distinctions between the firing rates of neurons which were in the group receiving elevated external input and the rest of the network, distinct synaptic weight distributions which distinguish these groups cannot be learned by the network. This is however possible in networks with no homeostasis or with diffusive homeostasis, as the differences in firing rates can be maintained.

4.2.4 *The effect of homeostasis on memory retention*

We will now consider how different types of homeostasis affect the dynamics of memory retention in these networks. Since STDP is always active, meaning that each spike leads to a small update in the pre- and post-synaptic weights, spontaneous activity in the network will have an impact on the quality of a memory encoded in the synaptic weights.

A simple way of investigating this is to insert a 'memory' into the network by directly perturbing the weights of a group of synapses within the network, and testing how long this perturbation lasts during spontaneous activity, before the perturbed synapses become indistinguishable from the rest of the network. As before, we will choose a group of 100 excitatory neurons within the network of 500. After allowing each network to run for 200 s with only STDP active and 250 s with both STDP and homeostasis active, we set all synapses which recurrently connect within this group of 100 neurons to their maximum value of 10 nS, while leaving the rest of the synapses in the network unchanged. Similar perturbations have been used previously to investigate the dynamics of memory maintenance in neuronal assemblies (Billings and van Rossum, 2009; Litwin-Kumar and Doiron, 2014; Higgins et al., 2014).

The weight matrices of the network immediately after this perturbation, and following 100 s of spontaneous activity after the perturbation, are shown in Figure 4.8. While there is initially a large difference between the synaptic weights within the perturbed group and the synaptic weights within the rest of the network, spontaneous activity slowly causes this difference to decay. This difference can be quantified by the SNR between the perturbed synaptic weights and the rest of the weights.

Interestingly, the SNR decay after the perturbation is slower than exponential (Figure 4.8, note the log-log scale). This is in agreement with empirical results from psychophysical experiments which measure memory retention (Wixted and Ebbesen, 1991, 1997), but is contrary to recent theoretical descriptions of memory lifetimes, which found an exponential decay of SNR in both single neuron models and recurrent network models (Billings and van Rossum, 2009; Higgins et al., 2014). Although other theoretical descriptions of memory retention do have lifetimes which are longer than those expected from exponential decay, and follow a power-law, these require a complex, multi-state description of synaptic weight dynamics (Fusi et al., 2005; Benna and Fusi, 2015). It is important to note that a linear relationship on a log-log scale is not sufficient to establish a power-law, and that distributions with heavy tails such as the stretched exponential or lognormal distribution will also exhibit these properties (Clauset et al., 2009).

While all networks exhibit a slower than exponential decay of SNR regardless of the homeostatic mechanism, there are significant differences in the rate of SNR decay between networks with different forms of homeostasis. Networks with no homeostasis exhibit the slowest SNR decay, with a slope of 0.38 ± 21, while networks with non-diffusive homeostasis have much faster decay timecourses, with slopes of 0.99 ± 08 and 0.79 ± 02 for uniform and variable targets respectively. As expected from previous results, networks with diffusive homeostasis exhibited behaviour closest to networks without any homeostasis at all, and had significantly slower SNR decay with a slope of 0.58 ± 03. Slopes are obtained from linear regression, with ± denoting standard error of the mean of 8 independent network realisations in each case.

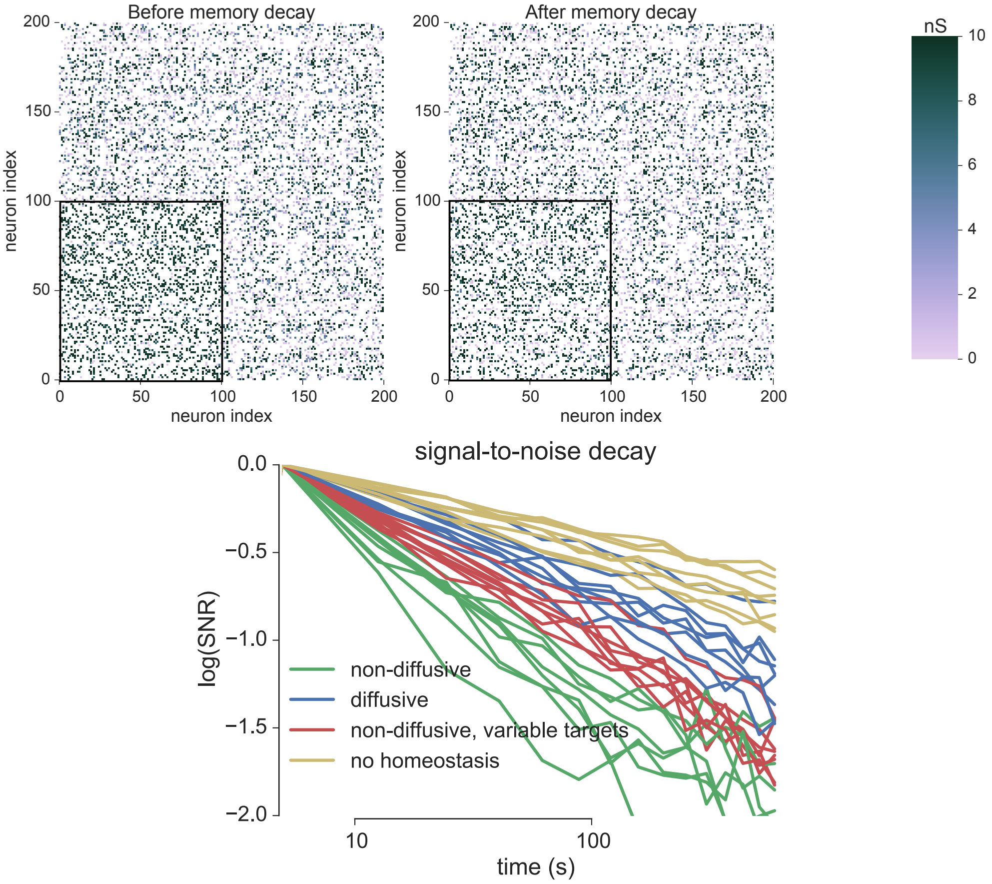

Figure 4.8: A portion of the excitatory weight matrix 10 s after the weights between the neurons with indices from 0 to 100 (those within the black box) are set to their maximum value of 10 nS (top, left), and 150 s after the weights have been changed (top, right). There is no homeostasis active in this network. The decay of the signal-to-noise ratio between the synaptic weights connecting the first 100 neurons, and the rest of the synaptic weights (bottom). Each set of coloured lines shows 8 instantiations of networks with different forms of homeostasis. Note that a log-log scale is used.

We next investigated further the properties of SNR decay, as the finding that it occurs slower than exponential decay was unexpected. We did this by measuring SNR decay over longer timescales of 500 s, although in this case we did not simulate networks with diffusive homeostasis as this proved too computationally intensive. Figure 4.9 plots SNR decay in these longer simulations in both linear-log and log-log scales, showing that there appears to be an exponential relationship in the linear-log scale and a linear relationship in the log-log scale (Figure 4.9, top right and top left). This is demonstrated further by attempting both exponential and linear fits to the

SNR decay in the linear-log scale. As expected, exponential fits provided a better fit to the decay than a linear fit (Figure 4.9 middle and bottom row), implying that SNR decay is slower than exponential, as these fits were performed in the linear-log scale. A model comparison test, the Akaike information criterion (Akaike, 1974), in which the number of parameters in each model is corrected for also accepts the exponential fit as superior to the linear fit in 8/10 network instances. While these results suggest that the SNR decay observed here is indeed slower than exponential decay, simulations over significantly longer timescales would be required to fully investigate the nature of this non-exponential decay. Unfortunately, computational limitations do not currently allow us to investigate this over the required timescales.

4.3 DISCUSSION

We have implemented a standard form of STDP in the spiking recurrent network model previously described in chapter 3. The distinctions between diffusive and non-diffusive homeostasis in the networks with static synaptic weights are conserved in networks with STDP (Fig. 4.3). This demonstrates that the limitations of non-diffusive homeostasis in maintaining neural heterogeneity and responsiveness extend beyond the case of static inputs, towards more realistic situations in which neurons receive ongoing and diverse perturbations. Indeed, networks with non-diffusive homeostasis lose almost all sensitivity to external inputs after STDP, while networks with diffusive homeostasis retain this sensitivity (Fig. 4.3C).

There are significant differences in the synaptic weight dynamics between networks with diffusive or non-diffusive homeostasis. Synaptic weights in networks with non-diffusive homeostasis tend to fluctuate more as HIP acts compared to networks with either diffusive homeostasis or no homeostasis (Figure 4.5). Although we have used very simplified paradigms in order to explore synaptic plasticity dynamics in these networks, our results suggest that non-diffusive homeostasis can interfere during both the formation of memories (Figure 4.7), and during the retention of memories (Figure 4.8). The more flexible nature of diffusive homeostasis seems to go some way to reducing this interference between homeostatic and Hebbian forces, leading to networks which both develops distinct synaptic weight distributions in response to structured inputs. These networks also retains ‘memories’, created by directly setting

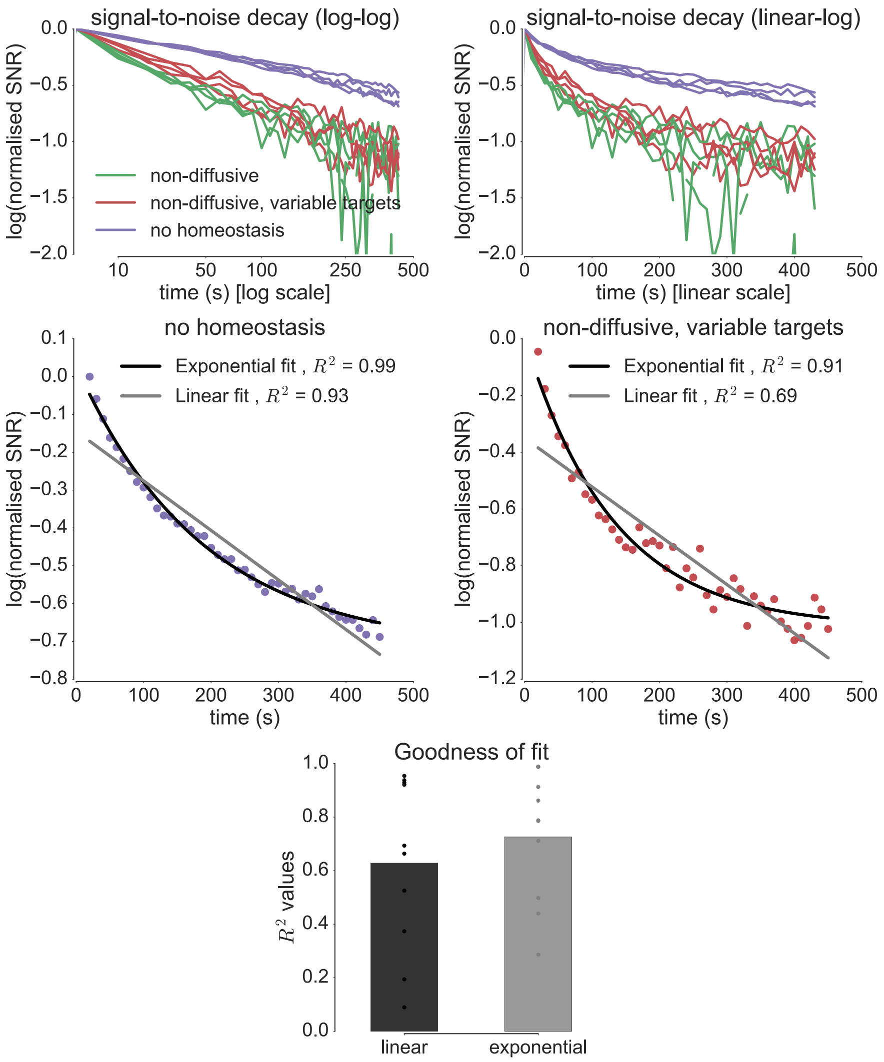

Figure 4.9: The decay of the signal-to-noise ratio between the synaptic weights connecting the first 100 neurons, and the rest of the synaptic weights, plotted in either the log-log scale (top right) or linear-log scale (top left). Each set of coloured lines shows 4 instantiations of networks with different forms of homeostasis. Example fits of the SNR decay on the linear-log scale to both linear and exponential functions (middle left and right, for no homeostasis and non-diffusive homeostasis with variable targets, respectively). Goodness of fit, measured as R^2 values, for both linear and exponential fits to SNR decay in the linear-log scale. Barplots denote the mean values, and points show each individual fit (bottom).

a subset of synaptic weights, for longer periods of time than networks with non-diffusive homeostasis.

4.3.1 *Alternative forms of STDP*

A straightforward question which arises from these results is whether the outcomes are dependant on the specifics of the chosen STDP learning rule. Would the results remain qualitatively similar if, for example, a multiplicative weight update were used instead of an additive weight update?

Preliminary results (not shown) suggest that the broad differences between diffusive and non-diffusive homeostasis outlined in chapter 3 are also conserved when multiplicative STDP, similar to that described by Van Rossum et al. (2000), is implemented instead of additive STDP. However, since synaptic weights are significantly less stable for this rule compared with additive STDP, we would expect different outcomes in the experiments described above, thus meriting further investigation (Billings and van Rossum, 2009). It is worth noting that exponential decay of SNR was observed for both synapses with a double well potential (similar to synaptic dynamics resulting from additive STDP), or synapses with a flat potential (similar to synaptic dynamics resulting from multiplicative STDP) (Billings and van Rossum, 2009; Higgins et al., 2014).

5

GENERAL DISCUSSION

5.1 SUMMARY OF THE THESIS

In this thesis we explored homeostatic intrinsic plasticity (HIP) using two different approaches. We discussed HIP in a model of single neurons in chapter 2, and in a recurrent network model in chapter 3 and chapter 4. While addressing different functional aspects of neuronal homeostasis, these two implementations share the same underlying mechanism: the modulation of potassium ion channel conductances by activity-dependent nitric oxide (NO) signalling.

We first investigated the role of NO-mediated modulation in the Medial Nucleus of the Trapezoid Body (MNTB), where the effect is well characterised (Steinert et al., 2008, 2011). Steinert et al. (2011) demonstrated that K_v2 conductances were increased in the NO-activated state which, as well as decreasing neural excitability, enables fast action potential repolarisation and is crucial for maintaining synaptic transmission fidelity at high frequencies. This is in contrast with the naive state, in which K_v3 conductances dominate during action potential repolarisation.

By constructing a multicompartmental conductance-based model of an MNTB neuron we could vary the conductances in order to reproduce the stimulus response properties recorded intracellularly during experiments. A multi-objective optimisation fitting procedure allowed us to identify the regions of conductance space whose stimulus response features best fit neurons in either the naive state or the NO-activated state. We found that the primary determinant of whether a model neuron exhibited responses typical of either the naive or NO-activated state was the conductance of the K_v2 channel. Increasing this conductance resulted in stimulus response properties more similar to the NO-activated state, confirming experimental observations (Steinert et al., 2011).

Using this classification of conductance space we could then investigate the metabolic efficiency of action potential generation. Models which were fit to the NO-activated state were significantly more metabolically expensive than models which were fit to the naive state. These results therefore identified a tradeoff occurring in MNTB neurons, between the ability to maintain synaptic transmission fidelity at high frequencies, and metabolic efficiency. Activity-dependent NO signalling enables these neurons to transition to the metabolically inefficient state only following periods of sustained synaptic activity, thereby dynamically mediating this tradeoff.

We next investigated the implications of NO acting as a diffusive neurotransmitter in a recurrent network model. We found that homeostasis which is mediated by a diffusive signal enables and maintains substantial population heterogeneity in firing rates, similar to that observed in experiments (Wohrer et al., 2013), and input heterogeneities can be preserved in the population activity. This is in contrast with non-diffusive homeostatic processes, in which heterogeneity is reduced as all neurons achieve their target firing rate. These differences arise due to a conflict in networks with non-diffusive homeostasis. Here, there is a tradeoff between a neurons ability to faithfully represent its external input while also maintaining its target firing rate. Diffusive homeostasis, on the other hand, allows a neuron to deviate from the target population activity, as its neighbours will counteract this deviation, thus maintaining stable population-averaged activity.

The properties of diffusive homeostasis are conserved when an STDP learning rule is implemented in the network. We then tested simplified memory formation and retention paradigms in these networks. Since firing rates may deviate from their target in networks with diffusive homeostasis, this flexibility allows those networks to both form memories from structured inputs, and retain memories for longer periods of time. Non-diffusive homeostasis on the other hand will counteract any representation of structured inputs, thus interfering in both memory formation and in the longevity of inserted memories.

5.2 HOMEOSTATIC CONSTRAINTS

Our results demonstrate the importance of considering multiple constraints which may be in conflict with each other when exploring the effects of homeostatic mechanisms. By evaluating the differences in metabolic efficiency between states of low and high NO signalling in the MNTB, we could identify that the NO-activated state carries a higher metabolic cost than the naive state. This newly introduced metabolic constraint conflicts with the functional constraint of optimising the maximal frequency of post-synaptic transmission, and the balance of NO signalling mediates the tradeoff between both constraints.

There are likely further constraints to be considered in the pre- and post- synaptic system of the calyx of Held and MNTB relay neuron. Synaptic transmission and synaptic vesicle recycling form a significant portion of the metabolic budget (Howarth et al., 2012), and any presynaptic effects of retrograde NO signalling could influence the balance of metabolic cost with function across the system (Kopp-Scheinpflug et al., 2011a; Hardingham et al., 2013). Additionally, the prevalence of short term plasticity at the calyx of Held is well documented, and could influence the outcome of both functional and metabolic constraints (von Gersdorff and Borst, 2002; Hennig et al., 2008; Borst and Soria van Hoeve, 2012). The NO signalling pathway could potentially play a neuroprotective role, as ATP depletion has been implicated with seizure-like activity (Kogure and Schwartzman, 1980; Yamada and Inagaki, 2005; Le Masson et al., 2014). In this scenario, NO signalling would ensure that the more metabolically costly state of high-fidelity synaptic transmission is only transitioned to when required.

Similarly, we later considered the constraints of maintaining a stable firing rate at the single neuron level and maintaining neural heterogeneity and flexibility at the network level. We found that, although these constraints conflict for a canonical non-diffusive homeostatic mechanism, diffusive homeostasis provides a mechanism which may reconcile these conflicting constraints.

5.3 NEURAL HOMEOSTASIS AND FUNCTION

In addition to identifying the importance of multiple constraints, our results from modelling NO signalling at the MNTB demonstrate a mechanism by which either the relaying function of a neuron may be optimised, or its metabolic efficiency, depending on recent electrical activity.

Our investigation of diffusive and non-diffusive homeostatic mechanisms in recurrent networks highlights the conflicts which may arise in optimising network function when a target firing rate is defined as a homeostatic set point. Although it is possible to reconcile optimisation of function and maintenance of an average firing rate at the single neuron level (Stemmler and Koch, 1999), we demonstrate that a canonical, non-diffusive homeostatic mechanism interferes significantly with the performance of a network in flexibly responding to inputs. Diffusive homeostasis on the other hand can counteract this interference, as well as minimising interference in synaptic dynamics during Hebbian plasticity. The potential for interference with Hebbian plasticity was recently observed by Toyoizumi et al. (2014) in the context of homeostatic synaptic scaling; the authors proposed a mechanism whereby both homeostatic and Hebbian factors contribute multiplicatively to the synaptic weights as a solution to this problem. We have proposed an alternative potential solution, in which the interference of a homeostatic mechanism is reduced by a diffusive activity readout, which enables relative flexibility in firing rates.

Additionally, although heterogeneity in the firing rates of neurons are functionally beneficial (Marsat and Maler, 2010; Tripathy et al., 2013), we find that many of the benefits are diminished when this heterogeneity is 'hard-coded' through randomly assigned target firing rates. While it is possible for networks with variable target rates to maintain a certain distribution of firing rates across a network with non-diffusive homeostasis, this constraint conflicts with the ability of individual neurons to flexibly adjust average firing rates, as observed by (Panas et al., 2015; Slomowitz et al., 2015)

5.4 FUTURE RESEARCH

We have explored the metabolic tradeoff hypothesis further in our MNTB neuron model by simulating the effect of ATP depletion. The model predicts that if ATP production is blocked, action potential generation would fail earlier in neurons in the NO-activated state, due to their higher K_v2 conductances. We have also identified measures of interest which are most sensitive to ATP depletion. This hypothesis is testable, and preliminary experiments are underway.

Since the distribution of firing thresholds is significantly different between networks which undergo diffusive homeostasis and networks which undergo non-diffusive homeostasis, this may warrant further empirical investigation. There are now a number of freely available datasets which characterise the heterogeneity of intrinsic neural properties in populations of cortical neurons, for example from Harrison et al. (2015) or from the Allen Institute for Brain Science (2015). Additionally, recent progress in the development of electrochemical NO biosensors and their application to measuring NO concentrations at high spatial and temporal resolution *in vivo* could elucidate the role of extracellular NO diffusion in regulating neural excitability across neural populations (Santos et al., 2008; Deng et al., 2010).

The paradigms we have used to investigate the interactions between Hebbian and homeostatic plasticity in these networks have been very simple, and biologically unrealistic. It would be beneficial to investigate these interactions using more functionally relevant paradigms, such as an input pattern separability task (Naudé et al., 2013), or the ability to form and retrieve memories encoded through cell assemblies (Zenke et al., 2015). It is likely that further distinctions between diffusive and non-diffusive homeostasis would be determined if a model of synaptic consolidation were introduced (Clopath, 2012; Ziegler et al., 2015), as one could hypothesise that networks which exhibit less synaptic weight fluctuations during spontaneous activity would be more capable of successfully consolidating and retaining recently formed memories.

BIBLIOGRAPHY

Abbott, L. F. (1999). Lapicque's introduction of the integrate-and-fire model neuron (1907). *Brain research bulletin*, 50(5):303–304. (Cited on pages 10 and 11.)

Akaike, H. (1974). A new look at the statistical model identification. *Automatic Control, IEEE Transactions on*, 19(6):716–723. (Cited on page 96.)

Alkon, D. L. (1984). Calcium-mediated reduction of ionic currents: a biophysical memory trace. *Science*, 226(4678):1037–1045. (Cited on page 10.)

Alle, H., Roth, A., and Geiger, J. R. (2009). Energy-efficient action potentials in hippocampal mossy fibers. *Science*, 325(5946):1405–1408. (Cited on pages 37 and 43.)

Allen Institute for Brain Science (2015). Allen cell types database. (Cited on page 102.)

Artinian, J., Peret, A., Mircheva, Y., Marti, G., and Crépel, V. (2015). Impaired neuronal operation through aberrant intrinsic plasticity in epilepsy. *Annals of neurology*, 77(4):592–606. (Cited on page 2.)

Attwell, D. and Laughlin, S. B. (2001). An energy budget for signaling in the grey matter of the brain. *Journal of Cerebral Blood Flow & Metabolism*, 21(10):1133–1145. (Cited on pages 3, 37, and 42.)

Bacallao, R., Garfinkel, A., Monke, S., Zampighi, G., and Mandel, L. J. (1994). Atp depletion: a novel method to study junctional properties in epithelial tissues. i. rearrangement of the actin cytoskeleton. *Journal of Cell Science*, 107(12):3301–3313. (Cited on page 45.)

Bahl, A., Stemmler, M. B., Herz, A. V., and Roth, A. (2012). Automated optimization of a reduced layer 5 pyramidal cell model based on experimental data. *Journal of neuroscience methods*, 210(1):22–34. (Cited on page 29.)

Baranauskas, G., Mukovskiy, A., Wolf, F., and Volgushev, M. (2010). The determinants of the onset dynamics of action potentials in a computational model. *Neuroscience*, 167(4):1070–1090. (Cited on page 23.)

Batchelor, A. M., Bartus, K., Reynell, C., Constantinou, S., Halvey, E. J., Held, K. F., Dostmann, W. R., Vernon, J., and Garthwaite, J. (2010). Exquisite sensitivity to subsecond, picomolar nitric oxide transients conferred on cells by guanylyl cyclase-coupled receptors. *P Natl Acad Sci USA*, 107(51):22060–5. (Cited on page 60.)

Bender, K. J. and Trussell, L. O. (2012). The physiology of the axon initial segment. *Annual review of neuroscience*, 35:249–265. (Cited on page 8.)

Benna, M. K. and Fusi, S. (2015). Computational principles of biological memory. *arXiv preprint arXiv:1507.07580*. (Cited on page 94.)

Bernard, C. (1878). Les phenomenes de la vie. *Bailliere, Paris*, 879. (Cited on page 1.)

Berntson, G. G. and Cacioppo, J. T. (2007). 19 integrative physiology: Homeostasis, allostasis, and the orchestration of systemic physiology. *Handbook of psychophysiology*, page 433. (Cited on page 3.)

Bienenstock, E. L., Cooper, L. N., and Munro, P. W. (1982). Theory for the development of neuron selectivity: orientation specificity and binocular interaction in visual cortex. *The Journal of Neuroscience*, 2(1):32–48. (Cited on pages 5 and 83.)

Billings, G. and van Rossum, M. C. (2009). Memory retention and spike-timing-dependent plasticity. *Journal of neurophysiology*, 101(6):2775–2788. (Cited on pages 82, 94, and 98.)

Blaise, G. A., Gauvin, D., Gangal, M., and Authier, S. (2005). Nitric oxide, cell signaling and cell death. *Toxicology*, 208(2):177–192. (Cited on page 7.)

Borst, J. G. G. and Soria van Hoeve, J. (2012). The calyx of held synapse: from model synapse to auditory relay. *Annual review of physiology*, 74:199–224. (Cited on pages 15, 16, 30, and 101.)

Brette, R. and Goodman, D. F. (2012). Simulating spiking neural networks on gpu. *Network: Computation in Neural Systems*. (Cited on page 88.)

Brew, H. M. and Forsythe, I. D. (1995). Two voltage-dependent k+ conductances with complementary functions in postsynaptic integration at a central auditory synapse. *The Journal of neuroscience*, 15(12):8011–8022. (Cited on page 17.)

Brew, H. M. and Forsythe, I. D. (2005). Systematic variation of potassium current amplitudes across the tonotopic axis of the rat medial nucleus of the trapezoid body. *Hearing research*, 206(1):116–132. (Cited on pages 16 and 48.)

Brickley, S. G., Revilla, V., Cull-Candy, S. G., Wisden, W., and Farrant, M. (2001). Adaptive regulation of neuronal excitability by a voltage-independent potassium conductance. *Nature*, 409(6816):88–92. (Cited on page 6.)

Brownell, W. E. and Manis, P. B. (2014). Structures, mechanisms, and energetics in temporal processing. In *Perspectives on Auditory Research*, pages 9–44. Springer. (Cited on page 37.)

Brunel, N. (2000). Dynamics of sparsely connected networks of excitatory and inhibitory spiking neurons. *J Comput Neurosci*, 8(3):183–208. (Cited on pages 53, 55, and 61.)

Burkitt, A. N. (2006). A review of the integrate-and-fire neuron model: I. homogeneous synaptic input. *Biological cybernetics*, 95(1):1–19. (Cited on pages 10 and 12.)

Cannon, W. B. (1926). Physiological regulation of normal states: some tentative postulates concerning biological homeostatics. *A Charles Richet: ses Amis, ses Colleges, ses Eleves*. (Cited on page 1.)

Carnevale, N. T. and Hines, M. L. (2006). *The NEURON book*. Cambridge University Press. (Cited on pages 9, 19, and 39.)

Castillo, P. E., Chiu, C. Q., and Carroll, R. C. (2011). Long-term plasticity at inhibitory synapses. *Current opinion in neurobiology*, 21(2):328–338. (Cited on page 83.)

Chandrasekaran, A. R., Shah, R. D., and Crair, M. C. (2007). Developmental homeostasis of mouse retinocollicular synapses. *The Journal of neuroscience*, 27(7):1746–1755. (Cited on page 4.)

Clauset, A., Shalizi, C. R., and Newman, M. E. (2009). Power-law distributions in empirical data. *SIAM review*, 51(4):661–703. (Cited on page 94.)

Clopath, C. (2012). Synaptic consolidation: an approach to long-term learning. *Cognitive neurodynamics*, 6(3):251–257. (Cited on page 103.)

Clopath, C., Büsing, L., Vasilaki, E., and Gerstner, W. (2010). Connectivity reflects coding: a model of voltage-based stdp with homeostasis. *Nature neuroscience*, 13(3):344–352. (Cited on page 82.)

D'amour, J. A. and Froemke, R. C. (2015). Inhibitory and excitatory spike-timing-dependent plasticity in the auditory cortex. *Neuron*, 86(2):514–528. (Cited on page 83.)

Daoudal, G., Hanada, Y., and Debanne, D. (2002). Bidirectional plasticity of excitatory postsynaptic potential (epsp)-spike coupling in ca1 hippocampal pyramidal neurons. *Proceedings of the National Academy of Sciences*, 99(22):14512–14517. (Cited on page 6.)

Debanne, D. and Poo, M.-M. (2010). Spike-timing dependent plasticity beyond synapse–pre-and post-synaptic plasticity of intrinsic neuronal excitability. *Frontiers in synaptic neuroscience*, 2. (Cited on page 6.)

Del-Bel, E., Oliveira, P., Oliveira, J., Mishra, P., Jobe, P., and Garcia-Cairasco, N. (1997). Anticonvulsant and proconvulsant roles of nitric oxide in experimental epilepsy models. *Braz J Med Biol Res*, 30(8):971–979. (Cited on page 79.)

Deng, X., Wang, F., and Chen, Z. (2010). A novel electrochemical sensor based on nano-structured film electrode for monitoring nitric oxide in living tissues. *Talanta*, 82(4):1218–1224. (Cited on page 103.)

Desai, N. S., Cudmore, R. H., Nelson, S. B., and Turrigiano, G. G. (2002). Critical periods for experience-dependent synaptic scaling in visual cortex. *Nature neuroscience*, 5(8):783–789. (Cited on page 4.)

Desai, N. S., Rutherford, L. C., and Turrigiano, G. G. (1999). Plasticity in the intrinsic excitability of cortical pyramidal neurons. *Nature neuroscience*, 2(6):515–520. (Cited on pages 5, 6, and 18.)

DiNuzzo, M. and Giove, F. (2012). Activity-dependent energy budget for neocortical signaling: Effect of short-term synaptic plasticity on the energy expended by spiking and synaptic activity. *Journal of neuroscience research*, 90(11):2094–2102. (Cited on page 37.)

Dirnagl, U., Lindauer, U., and Villringer, A. (1993). Role of nitric oxide in the coupling of cerebral blood flow to neuronal activation in rats. *Neuroscience letters*, 149(1):43–46. (Cited on page 49.)

Dodson, P. D., Barker, M. C., and Forsythe, I. D. (2002). Two heteromeric kv1 potassium channels differentially regulate action potential firing. *The Journal of neuroscience*, 22(16):6953–6961. (Cited on page 17.)

Druckmann, S., Banitt, Y., Gidon, A., Schürmann, F., Markram, H., and Segev, I. (2007). A novel multiple objective optimization framework for constraining conductance-based neuron models by experimental data. *Frontiers in neuroscience*, 1(1):7. (Cited on pages 29 and 46.)

Druckmann, S., Berger, T. K., Schürmann, F., Hill, S., Markram, H., and Segev, I. (2011). Effective stimuli for constructing reliable neuron models. *PLoS Comput Biol*, 7(8):e1002133–e1002133. (Cited on page 46.)

Eguchi, K., Nakanishi, S., Takagi, H., Taoufiq, Z., and Takahashi, T. (2012). Maturation of a pkg-dependent retrograde mechanism for exoendocytic coupling of synaptic vesicles. *Neuron*, 74(3):517–529. (Cited on page 18.)

Ermentrout, B. (1998). Linearization of FI curves by adaptation. *Neural Comput*, 10(7):1721–1729. (Cited on page 76.)

Fohlmeister, J. F. (2009). A nerve model of greatly increased energy-efficiency and encoding flexibility over the hodgkin–huxley model. *Brain research*, 1296:225–233. (Cited on page 37.)

Fourcaud-Trocmé, N., Hansel, D., Van Vreeswijk, C., and Brunel, N. (2003). How spike generation mechanisms determine the neuronal response to fluctuating inputs. *The Journal of neuroscience*, 23(37):11628–11640. (Cited on page 11.)

Freeman, J. B. and Dale, R. (2013). Assessing bimodality to detect the presence of a dual cognitive process. *Behavior research methods*, 45(1):83–97. (Cited on pages 91 and 92.)

Fusi, S., Drew, P. J., and Abbott, L. (2005). Cascade models of synaptically stored memories. *Neuron*, 45(4):599–611. (Cited on page 94.)

Gally, J., Montague, P., Reeke, G., and Edelman, G. (1990). The NO hypothesis: possible effects of a short-lived, rapidly diffusible signal in the development and function of the nervous system. *P Natl Acad Sci USA*, 87(9):3547–3551. (Cited on pages 49, 50, and 51.)

Garthwaite, J. (2008). Concepts of neural nitric oxide-mediated transmission. *Eur J Neurosci*, 27(11):2783–2802. (Cited on pages 7, 49, and 51.)

Gerstner, W. and Brette, R. (2009). Adaptive exponential integrate-and-fire model. *Scholarpedia*, 4(6):8427. (Cited on page 11.)

Gittelman, J. X. and Tempel, B. L. (2006). Kv1. 1-containing channels are critical for temporal precision during spike initiation. *Journal of neurophysiology*, 96(3):1203–1214. (Cited on page 17.)

Giugliano, M., Bove, M., and Grattarola, M. (1999). Activity-driven computational strategies of a dynamically regulated integrate-and-fire model neuron. *Journal of computational neuroscience*, 7(3):247–254. (Cited on page 11.)

Golowasch, J., Abbott, L., and Marder, E. (1999a). Activity-dependent regulation of potassium currents in an identified neuron of the stomatogastric ganglion of the crab cancer borealis. *Journal of Neuroscience*, 19:RC33–1. (Cited on page 10.)

Golowasch, J., Casey, M., Abbott, L., and Marder, E. (1999b). Network stability from activity-dependent regulation of neuronal conductances. *Neural Computation*, 11(5):1079–1096. (Cited on page 11.)

Golowasch, J., Goldman, M. S., Abbott, L., and Marder, E. (2002). Failure of averaging in the construction of a conductance-based neuron model. *Journal of Neurophysiology*, 87(2):1129–1131. (Cited on pages 6, 10, 27, and 47.)

Goodman, D. and Brette, R. (2008). Brian: a simulator for spiking neural networks in python. *Front Neuroinform*, 2:192–7. (Cited on pages 60 and 84.)

Graupner, M. and Brunel, N. (2012). Calcium-based plasticity model explains sensitivity of synaptic changes to spike pattern, rate, and dendritic location. *Proceedings of the National Academy of Sciences*, 109(10):3991–3996. (Cited on page 82.)

Grothe, B., Pecka, M., and McAlpine, D. (2010). Mechanisms of sound localization in mammals. *Physiological Reviews*, 90(3):983–1012. (Cited on page 15.)

Grubb, M. S. and Burrone, J. (2010). Activity-dependent relocation of the axon initial segment fine-tunes neuronal excitability. *Nature*, 465(7301):1070–1074. (Cited on pages 8 and 24.)

Günay, C. and Prinz, A. A. (2010). Model calcium sensors for network homeostasis: sensor and readout parameter analysis from a database of model neuronal networks. *The Journal of Neuroscience*, 30(5):1686–1698. (Cited on page 11.)

Hall, C. and Garthwaite, J. (2009). What is the real physiological NO concentration in vivo? *Nitric Oxide*, 21(2):92–9103. (Cited on page 60.)

Hallermann, S., de Kock, C. P., Stuart, G. J., and Kole, M. H. (2012). State and location dependence of action potential metabolic cost in cortical pyramidal neurons. *Nature neuroscience*, 15(7):1007–1014. (Cited on pages 14 and 37.)

Hardingham, N., Dachtler, J., and Fox, K. (2013). The role of nitric oxide in presynaptic plasticity and homeostasis. *Frontiers in cellular neuroscience*, 7. (Cited on page 101.)

Harnack, D., Pelko, M., Chaillet, A., Chitour, Y., and van Rossum, M. C. (2015). Stability of neuronal networks with homeostatic regulation. *PLoS Comput Biol*, 11(7):e1004357. (Cited on pages 11, 12, and 83.)

Harrison, P. M., Badel, L., Wall, M. J., and Richardson, M. J. E. (2015). Experimentally verified parameter sets for modelling heterogeneous neocortical pyramidal-cell populations. *PLoS computational biology*, 11(8):e1004165. (Cited on page 102.)

Hasenstaub, A., Otte, S., Callaway, E., and Sejnowski, T. J. (2010). Metabolic cost as a unifying principle governing neuronal biophysics. *Proceedings of the National Academy of Sciences*, 107(27):12329–12334. (Cited on pages 3, 12, 37, 39, 43, and 49.)

Hay, E., Hill, S., Schürmann, F., Markram, H., and Segev, I. (2011). Models of neocortical layer 5b pyramidal cells capturing a wide range of dendritic and perisomatic active properties. *PLoS computational biology*, 7(7). (Cited on page 29.)

Hebb, D. (1949). The organization of behavior. *New York Wiley*. (Cited on page 1.)

Hennig, M. H., Postlethwaite, M., Forsythe, I. D., and Graham, B. P. (2008). Interactions between multiple sources of short-term plasticity during evoked and spontaneous activity at the rat calyx of held. *The Journal of physiology*, 586(13):3129–3146. (Cited on pages 15 and 101.)

Higgins, D., Graupner, M., and Brunel, N. (2014). Memory maintenance in synapses with calcium-based plasticity in the presence of background activity. (Cited on pages 94 and 98.)

Hill, A. V. (1910). The possible effects of the aggregation of the molecules of haemoglobin on its dissociation curves. *J Physiol*, 40:4–7. (Cited on page 54.)

Hille, B. et al. (2001). *Ion channels of excitable membranes*, volume 507. Sinauer Sunderland, MA. (Cited on pages 9, 14, and 22.)

Hirase, H., Leinekugel, X., Czurkó, A., Csicsvari, J., and Buzsáki, G. (2001). Firing rates of hippocampal neurons are preserved during subsequent sleep episodes and modified by novel awake experience. *P Natl Acad Sci USA*, 98(16):9386–9390. (Cited on page 78.)

Hodgkin, A. (1975). The optimum density of sodium channels in an unmyelinated nerve. *Philosophical Transactions of the Royal Society of London. Series B, Biological sciences*, pages 297–300. (Cited on page 43.)

Hodgkin, A. L. and Huxley, A. F. (1952). A quantitative description of membrane current and its application to conduction and excitation in nerve. *The Journal of physiology*, 117(4):500–544. (Cited on page 8.)

Holmgren, C., Harkany, T., Svennenfors, B., and Zilberter, Y. (2003). Pyramidal cell communication within local networks in layer 2/3 of rat neocortex. *J Physiol*, 551(1):139–153. (Cited on page 72.)

Howarth, C., Gleeson, P., and Attwell, D. (2012). Updated energy budgets for neural computation in the neocortex and cerebellum. *Journal of Cerebral Blood Flow & Metabolism*, 32(7):1222–1232. (Cited on pages 37 and 101.)

Huang, Y.-Y., Colino, A., Selig, D. K., and Malenka, R. C. (1992). The influence of prior synaptic activity on the induction of long-term potentiation. *Science*, 255(5045):730–733. (Cited on page 5.)

Hunter, J. D. (2007). Matplotlib: A 2d graphics environment. *Comput Sci Eng*, 9(3):0090–95. (Cited on page 61.)

Izhikevich, E. M. (2004). Which model to use for cortical spiking neurons? *IEEE transactions on neural networks*, 15(5):1063–1070. (Cited on pages 11 and 12.)

Izhikevich, E. M. et al. (2003). Simple model of spiking neurons. *IEEE Transactions on neural networks*, 14(6):1569–1572. (Cited on page 11.)

Janowitz, M. K. and Van Rossum, M. C. (2006). Excitability changes that complement hebbian learning. *Network: Computation in Neural Systems*, 17(1):31–41. (Cited on page 6.)

Johnston, J., Forsythe, I. D., and Conny, K. (2010). Going native: voltage-gated potassium channels controlling neuronal excitability. *The Journal of physiology*, 588(Pt 17):3187–3200. (Cited on pages 16, 17, 22, 23, and 31.)

Johnston, J., Griffin, S. J., Baker, C., Skrzypiec, A., Chernova, T., and Forsythe, I. D. (2008). Initial segment kv2.2 channels mediate a slow delayed rectifier and maintain high frequency action potential firing in medial nucleus of the trapezoid body neurons. *The Journal of physiology*, 586(14):3493–3509. (Cited on pages 17, 19, 20, 23, 28, and 32.)

Kety, S. S. (1957). The general metabolism of the brain in vivo. *Metabolism of the nervous system*, pages 221–237. (Cited on page 37.)

Kirkwood, A., Rioult, M. G., and Bear, M. F. (1996). Experience-dependent modification of synaptic plasticity in visual cortex. *Nature*, 381(6582):526–528. (Cited on page 5.)

Kogure, K. and Schwartzman, R. (1980). Seizure propagation and atp depletion in the rat stroke model. *Epilepsia*, 21(1):63–72. (Cited on page 101.)

Kohonen, T. (1993). Physiological interpretation of the self-organizing map algorithm. *Neural Networks*, 6(6):895–905. (Cited on page 79.)

Kole, M. H. and Stuart, G. J. (2012). Signal processing in the axon initial segment. *Neuron*, 73(2):235–247. (Cited on page 23.)

Kopp-Scheinpflug, C., Steinert, J. R., and Forsythe, I. D. (2011a). Modulation and control of synaptic transmission across the mntb. *Hearing research*, 279(1):22–31. (Cited on page 101.)

Kopp-Scheinpflug, C., Tolnai, S., Malmierca, M., and Rübsamen, R. (2008). The medial nucleus of the trapezoid body: comparative physiology. *Neuroscience*, 154(1):160–170. (Cited on page 16.)

Kopp-Scheinpflug, C., Tozer, A. J., Robinson, S. W., Tempel, B. L., Hennig, M. H., and Forsythe, I. D. (2011b). The sound of silence: ionic mechanisms encoding sound termination. *Neuron*, 71(5):911–925. (Cited on pages 15 and 20.)

Kostal, L., Lansky, P., and McDonnell, M. D. (2013). Metabolic cost of neuronal information in an empirical stimulus-response model. *Biological cybernetics*, 107(3):355–365. (Cited on page 12.)

Kuba, H., Oichi, Y., and Ohmori, H. (2010). Presynaptic activity regulates na+ channel distribution at the axon initial segment. *Nature*, 465(7301):1075–1078. (Cited on page 8.)

Lapicque, L. (1907). Recherches quantitatives sur l'excitation électrique des nerfs traitée comme une polarisation. *J. Physiol. Pathol. Gen*, 9(1):620–635. (Cited on page 10.)

Lazar, A., Pipa, G., and Triesch, J. (2009). SORN: a self-organizing recurrent neural network. *Front Comput Neurosci*, 3:23. (Cited on pages 52, 62, and 83.)

Leão, R. M., Kushmerick, C., Pinaud, R., Renden, R., Li, G. L., Taschenberger, H., Spirou, G., Levinson, S., and von Gersdorff, H. (2005). Presynaptic na+ channels: locus, development, and recovery from inactivation at a high-fidelity synapse. *The Journal of neuroscience : the official journal of the Society for Neuroscience*, 25(14):3724–3738. (Cited on page 28.)

Le Masson, G., Przedborski, S., and Abbott, L. (2014). A computational model of motor neuron degeneration. *Neuron*, 83(4):975–988. (Cited on pages 44 and 101.)

Leao, R. N., Naves, M. M., Leao, K. E., and Walmsley, B. (2006). Altered sodium currents in auditory neurons of congenitally deaf mice. *European Journal of Neuroscience*, 24(4):1137–1146. (Cited on page 24.)

LeMasson, G., Marder, E., and Abbott, L. (1993). Activity-dependent regulation of conductances in model neurons. *Science*, 259(5103):1915–1917. (Cited on pages 10, 11, and 52.)

Leo, R. N., Leo, R. M., da Costa, L. F., Levinson, S. R., and Walmsley, B. (2008). A novel role for MNTB neuron dendrites in regulating action potential amplitude and cell excitability during repetitive firing. *European Journal of Neuroscience*, 27(12):3095–3108. (Cited on page 24.)

Levenberg, K. (1944). A method for the solution of certain non–linear problems in least squares. (Cited on page 47.)

Litwin-Kumar, A. and Doiron, B. (2014). Formation and maintenance of neuronal assemblies through synaptic plasticity. *Nature communications*, 5. (Cited on page 94.)

Longtin, A. (2010). Stochastic dynamical systems. *Scholarpedia*, 5(4):1619. (Cited on page 30.)

Lorteije, J. A., Rusu, S. I., Kushmerick, C., and Borst, J. G. G. (2009). Reliability and precision of the mouse calyx of held synapse. *The Journal of Neuroscience*, 29(44):13770–13784. (Cited on page 15.)

Lourenço, C. F., Santos, R. M., Barbosa, R. M., Cadenas, E., Radi, R., and Laranjinha, J. (2014). Neurovascular coupling in hippocampus is mediated via diffusion by neuronal-derived nitric oxide. *Free Radic Biol Med*, 73(0):421–429. (Cited on pages 7, 50, and 52.)

Macica, C. M., von Hehn, C. A. A., Wang, L. Y., Ho, C. S., Yokoyama, S., Joho, R. H., and Kaczmarek, L. K. (2003). Modulation of the kv3.1b potassium channel isoform adjusts the fidelity of the firing pattern of auditory neurons. *The Journal of neuroscience : the official journal of the Society for Neuroscience*, 23(4):1133–1141. (Cited on page 19.)

Mainen, Z. F., Joerges, J., Huguenard, J. R., and Sejnowski, T. J. (1995). A model of spike initiation in neocortical pyramidal neurons. *Neuron*, 15(6):1427–1439. (Cited on page 49.)

Marder, E. and Goaillard, J.-M. (2006). Variability, compensation and homeostasis in neuron and network function. *Nature Reviews Neuroscience*, 7(7):563–574. (Cited on page 6.)

Marder, E. and Taylor, A. L. (2011). Multiple models to capture the variability in biological neurons and networks. *Nature neuroscience*, 14(2):133–138. (Cited on pages 10 and 27.)

Markram, H., Gerstner, W., and Sjöström, P. J. (2012). Spike-timing-dependent plasticity: a comprehensive overview. *Frontiers in synaptic neuroscience*, 4. (Cited on page 81.)

Marquardt, D. W. (1963). An algorithm for least-squares estimation of nonlinear parameters. *Journal of the society for Industrial and Applied Mathematics*, 11(2):431–441. (Cited on page 47.)

Marsat, G. and Maler, L. (2010). Neural heterogeneity and efficient population codes for communication signals. *J Neurophysiol*, 104(5):2543–2555. (Cited on pages 52 and 102.)

Mc Laughlin, M., van der Heijden, M., and Joris, P. X. (2008). How secure is in vivo synaptic transmission at the calyx of held? *The Journal of Neuroscience*, 28(41):10206–10219. (Cited on page 15.)

McCormick, D. A., Shu, Y., and Yu, Y. (2007). Neurophysiology: Hodgkin and huxley model—still standing? *Nature*, 445(7123):E1–E2. (Cited on pages 23 and 26.)

McNaught, A. D. and Wilkinson, A. (1997). *Compendium of chemical terminology*, volume 1669. Blackwell Science Oxford. (Cited on page 42.)

Meeks, J. P. and Mennerick, S. (2007). Action potential initiation and propagation in ca3 pyramidal axons. *Journal of neurophysiology*, 97(5):3460–3472. (Cited on pages 49 and 50.)

Miller, K. D. (1996). Synaptic economics: competition and cooperation in synaptic plasticity. *Neuron*, 17(3):371–374. (Cited on page 2.)

Mizuseki, K. and Buzsáki, G. (2013). Preconfigured, skewed distribution of firing rates in the hippocampus and entorhinal cortex. *Cell Reports*, 4(5):1010–1021. (Cited on page 77.)

Mockett, B., Coussens, C., and Abraham, W. C. (2002). Nmda receptor-mediated metaplasticity during the induction of long-term depression by low-frequency stimulation. *European Journal of Neuroscience*, 15(11):1819–1826. (Cited on page 5.)

Moore, J. W. (2007). Voltage clamp. *Scholarpedia*, 2(9):3060. (Cited on page 27.)

Mori, Y., Matsubara, H., Folco, E., Siegel, A., and Koren, G. (1993). The transcription of a mammalian voltage-gated potassium channel is regulated by camp in a cell-specific manner. *Journal of Biological Chemistry*, 268(35):26482–26493. (Cited on page 18.)

Murakoshi, H. and Trimmer, J. S. (1999). Identification of the kv2. 1 k+ channel as a major component of the delayed rectifier k+ current in rat hippocampal neurons. *The Journal of neuroscience*, 19(5):1728–1735. (Cited on page 49.)

Naudé, J., Cessac, B., Berry, H., and Delord, B. (2013). Effects of cellular homeostatic intrinsic plasticity on dynamical and computational properties of biological recurrent neural networks. *J Neurosci*, 33(38):15032–15043. (Cited on pages 12, 13, 52, 60, 83, and 103.)

Niebur, E. (2008). Neuronal cable theory. *Scholarpedia*, 3(5):2674. (Cited on page 9.)

Nikonenko, I., Nikonenko, A., Mendez, P., Michurina, T., Enikolopov, G., and Muller, D. (2013). Nitric oxide mediates local activity-dependent excitatory synapse development. *P Natl Acad Sci USA*, 110(44):E4142–E4151. (Cited on pages 7 and 79.)

Niven, J. E., Anderson, J. C., and Laughlin, S. B. (2007). Fly photoreceptors demonstrate energy-information trade-offs in neural coding. *PLoS Biol*, 5(4):e116. (Cited on pages 12, 43, and 49.)

Nowotny, T. and Huerta, R. (2003). Explaining synchrony in feed-forward networks. *Biological cybernetics*, 89(4):237–241. (Cited on page 2.)

Nowotny, T., Rabinovich, M. I., and Abarbanel, H. D. (2003). Spatial representation of temporal information through spike-timing-dependent plasticity. *Physical Review E*, 68(1):011908. (Cited on page 82.)

O'Leary, T., Williams, A. H., Caplan, J. S., and Marder, E. (2013). Correlations in ion channel expression emerge from homeostatic tuning rules. *P Natl Acad Sci USA*, 110(28):E2645–E2654. (Cited on pages 10 and 52.)

O'Leary, T., Williams, A. H., Franci, A., and Marder, E. (2014). Cell types, network homeostasis, and pathological compensation from a biologically plausible ion channel expression model. *Neuron*, 82(4):809–821. (Cited on pages 10 and 79.)

O'Leary, T. and Wyllie, D. J. (2011). Neuronal homeostasis: time for a change? *The Journal of physiology*, 589(20):4811–4826. (Cited on page 3.)

O'Leary, T. S. (2008). Homeostatic regulation of intrinsic excitability in hippocampal neurons. (Cited on page 18.)

Olypher, A. and Prinz, A. (2010). Geometry and dynamics of activity-dependent homeostatic regulation in neurons. *J Comput Neurosci*, 28(3):361–374. (Cited on pages 52 and 62.)

Osborne, D. M., Pearson-Leary, J., and McNay, E. C. (2015). The neuroenergetics of stress hormones in the hippocampus and implications for memory. *Frontiers in neuroscience*, 9. (Cited on page 50.)

Ott, S. R., Philippides, A., Elphick, M. R., and O'Shea, M. (2007). Enhanced fidelity of diffusive nitric oxide signalling by the spatial segregation of source and target neurones in the memory centre of an insect brain. *European Journal of Neuroscience*, 25(1):181–190. (Cited on page 79.)

Padmanabhan, K. and Urban, N. N. (2010). Intrinsic biophysical diversity decorrelates neuronal firing while increasing information content. *Nat Neurosci*, 13(10):1276–

82. (Cited on page 13.)

Panas, D., Amin, H., Maccione, A., Muthmann, O., van Rossum, M., Berdondini, L., and Hennig, M. H. (2015). Sloppiness in spontaneously active neuronal networks. *The Journal of Neuroscience*, 35(22):8480–8492. (Cited on pages 13 and 102.)

Pape, H.-C. and Mager, R. (1992). Nitric oxide controls oscillatory activity in thalamocortical neurons. *Neuron*, 9(3):441–448. (Cited on pages 49 and 51.)

Pérez, F. and Granger, B. E. (2007). IPython: a system for interactive scientific computing. *Comput Sci Eng*, 9(3):21–29. (Cited on page 60.)

Pfister, R., Schwarz, K. A., Janczyk, M., Dale, R., and Freeman, J. B. (2013). Good things peak in pairs: a note on the bimodality coefficient. *Frontiers in psychology*, 4. (Cited on pages 91 and 92.)

Philippides, A., Husbands, P., and O'Shea, M. (2000). Four-dimensional neuronal signaling by nitric oxide: a computational analysis. *J Neurosci*, 20(3):1199–1207. (Cited on pages 54 and 60.)

Philippides, A., Ott, S. R., Husbands, P., Lovick, T. A., and O'Shea, M. (2005). Modeling cooperative volume signaling in a plexus of nitric oxide synthase-expressing neurons. *The Journal of neuroscience*, 25(28):6520–6532. (Cited on pages 49 and 55.)

Prinz, A. A., Billimoria, C. P., and Marder, E. (2003). Alternative to hand-tuning conductance-based models: construction and analysis of databases of model neurons. *Journal of Neurophysiology*, 90(6):3998–4015. (Cited on page 31.)

Rall, W. (1959). Branching dendritic trees and motoneuron membrane resistivity. *Experimental neurology*, 1(5):491–527. (Cited on page 9.)

Rall, W. (2009). Rall model. *Scholarpedia*, 4(4):1369. (Cited on page 9.)

Remme, M. W. and Wadman, W. J. (2012). Homeostatic scaling of excitability in recurrent neural networks. (Cited on pages 11, 12, and 83.)

Rothman, J. S. and Manis, P. B. (2003). The roles potassium currents play in regulating the electrical activity of ventral cochlear nucleus neurons. *Journal of neurophysiology*, 89(6):3097–3113. (Cited on page 20.)

Roxin, A., Brunel, N., Hansel, D., Mongillo, G., and van Vreeswijk, C. (2011). On the distribution of firing rates in networks of cortical neurons. *J Neurosci*, 31(45):16217–16226. (Cited on pages 55, 56, 65, 76, and 77.)

Rudy, B. and McBain, C. J. (2001). Kv3 channels: voltage-gated k+ channels designed for high-frequency repetitive firing. *Trends in neurosciences*, 24(9):517–526. (Cited on page 49.)

Salerno, J. C. and Ghosh, D. K. (2009). Space, time and nitric oxide–neuronal nitric oxide synthase generates signal pulses. *FEBS journal*, 276(22):6677–6688. (Cited on page 60.)

Santos, R. M., Lourenço, C. F., Piedade, A. P., Andrews, R., Pomerleau, F., Huettl, P., Gerhardt, G. A., Laranjinha, J., and Barbosa, R. M. (2008). A comparative study of carbon fiber-based microelectrodes for the measurement of nitric oxide in brain tissue. *Biosensors and Bioelectronics*, 24(4):704–709. (Cited on page 103.)

Sätzler, K., Söhl, L. F., Bollmann, J. H., Borst, J. G. G., Frotscher, M., Sakmann, B., and Lübke, J. H. (2002). Three-dimensional reconstruction of a calyx of held and its postsynaptic principal neuron in the medial nucleus of the trapezoid body. *The*

Journal of neuroscience, 22(24):10567–10579. (Cited on page 44.)

Savin, C., Peter, D., and Lengyel, M. (2014). Optimal recall from bounded metaplastic synapses: predicting functional adaptations in hippocampal area ca3. *PLoS Comput. Biol*, 10:e1003489. (Cited on page 6.)

Savin, C., Triesch, J., and Meyer-Hermann, M. (2009). Epileptogenesis due to glia-mediated synaptic scaling. *Journal of The Royal Society Interface*, 6(37):655–668. (Cited on page 79.)

Schatz, C. J. (1992). The developing brain. *Scientific American*, 267(3):60–67. (Cited on page 1.)

Schulz, D. J., Goaillard, J.-M., and Marder, E. (2006). Variable channel expression in identified single and electrically coupled neurons in different animals. *Nature neuroscience*, 9(3):356–362. (Cited on page 10.)

Selverston, A. (2008). Stomatogastric ganglion. *Scholarpedia*, 3(4):1661. (Cited on page 6.)

Sengupta, B., Stemmler, M., Laughlin, S. B., and Niven, J. E. (2010). Action potential energy efficiency varies among neuron types in vertebrates and invertebrates. *PLoS Comput Biol*, 6(7):e1000840. (Cited on pages 37, 39, and 49.)

Seung, H. S. and Sompolinsky, H. (1993). Simple models for reading neuronal population codes. *P Natl Acad Sci USA*, 90(22):10749–10753. (Cited on page 78.)

Shamir, M. and Sompolinsky, H. (2006). Implications of neuronal diversity on population coding. *Neural Comput*, 18(8):1951–1986. (Cited on page 78.)

Sjöström, J. and Gerstner, W. (2010). Spike-timing dependent plasticity. *Scholarpedia*, 5(2):1362. (Cited on page 82.)

Skinner, F. K. (2006). Conductance-based models. *Scholarpedia*, 1(11):1408. (Cited on page 9.)

Slomowitz, E., Styr, B., Vertkin, I., Milshtein-Parush, H., Nelken, I., Slutsky, M., Slutsky, I., and Nelson, S. B. (2015). Interplay between population firing stability and single neuron dynamics in hippocampal networks. *eLife*, 4. (Cited on pages 13, 78, and 102.)

Son, H., Hawkins, R. D., Martin, K., Kiebler, M., Huang, P. L., Fishman, M. C., and Kandel, E. R. (1996). Long-term potentiation is reduced in mice that are doubly mutant in endothelial and neuronal nitric oxide synthase. *Cell*, 87(6):1015–23. (Cited on pages 7 and 79.)

Song, P., Yang, Y., Barnes-Davies, M., Bhattacharjee, A., Hamann, M., Forsythe, I. D., Oliver, D. L., and Kaczmarek, L. K. (2005a). Acoustic environment determines phosphorylation state of the kv3. 1 potassium channel in auditory neurons. *Nature neuroscience*, 8(10):1335–1342. (Cited on page 18.)

Song, S., Miller, K. D., and Abbott, L. F. (2000). Competitive hebbian learning through spike-timing-dependent synaptic plasticity. *Nat Neurosci*, 3(9):919–926. (Cited on pages 81, 82, 84, and 85.)

Song, S., Sjöström, P. J., Reigl, M., Nelson, S., and Chklovskii, D. B. (2005b). Highly nonrandom features of synaptic connectivity in local cortical circuits. *PLoS Biol*, 3(3):e68. (Cited on page 82.)

Steinert, J., Cornelia, K., Baker, C., Challiss, R., Mistry, R., Haustein, M., Griffin, S., Tong, H., Graham, B., and Forsythe, I. (2008). Nitric oxide is a volume transmitter regulating postsynaptic excitability at a glutamatergic synapse. *Neuron*, 60(4):642–656. (Cited on pages 7, 17, 18, 28, 37, 52, 62, and 99.)

Steinert, J. R., Robinson, S. W., Tong, H., Haustein, M. D., Cornelia, K., and Forsythe, I. D. (2011). Nitric oxide is an activity-dependent regulator of target neuron intrinsic excitability. *Neuron*, 71(2):291–305. (Cited on pages 7, 14, 17, 18, 19, 27, 28, 29, 30, 32, 34, 36, 45, 48, 49, 52, 60, 68, 79, and 99.)

Stemmler, M. and Koch, C. (1999). How voltage-dependent conductances can adapt to maximize the information encoded by neuronal firing rate. *Nature neuroscience*, 2(6):521–527. (Cited on pages 3, 13, and 102.)

Sterling, P. (2012). Allostasis: a model of predictive regulation. *Physiology & behavior*, 106(1):5–15. (Cited on page 3.)

Sterling, P. and Eyer, J. (1988). Allostasis: a new paradigm to explain arousal pathology. (Cited on page 3.)

Sun, Y. J., Wu, G. K., Liu, B.-h., Li, P., Zhou, M., Xiao, Z., Tao, H. W., and Zhang, L. I. (2010). Fine-tuning of pre-balanced excitation and inhibition during auditory cortical development. *Nature*, 465(7300):927–931. (Cited on page 12.)

Sweeney, Y., Hellgren Kotaleski, J., and Hennig, M. H. (2015). A diffusive homeostatic signal maintains neural heterogeneity and responsiveness in cortical networks. *PLoS Comput Biol*, 11(7):e1004389. (Cited on page 51.)

Swensen, A. M. and Bean, B. P. (2005). Robustness of burst firing in dissociated purkinje neurons with acute or long-term reductions in sodium conductance. *The Journal of neuroscience*, 25(14):3509–3520. (Cited on page 6.)

Tamagnini, F., Barker, G., Warburton, C., Burattini, C., Aicardi, G., and Bashir, Z. (2013). Nitric oxide-dependent LTD but not endocannabinoid-LTP is crucial for visual recognition memory. *J Physiol*, 591(16):3963–3979. (Cited on pages 7 and 79.)

Tetzlaff, C., Kolodziejski, C., Timme, M., and Wörgötter, F. (2011). Synaptic scaling in combination with many generic plasticity mechanisms stabilizes circuit connectivity. *Frontiers in computational neuroscience*, 5. (Cited on page 82.)

Tetzlaff, C., Okujeni, S., Egert, U., Wörgötter, F., Butz, M., et al. (2010). Self-organized criticality in developing neuronal networks. *PLoS Comput. Biol*, 6(12):e1001013. (Cited on page 12.)

Tobin, A.-E., Cruz-Bermúdez, N. D., Marder, E., and Schulz, D. J. (2009). Correlations in ion channel mrna in rhythmically active neurons. *PloS one*, 4(8):e6742–e6742. (Cited on page 10.)

Toledo-Rodriguez, M., Blumenfeld, B., Wu, C., Luo, J., Attali, B., Goodman, P., and Markram, H. (2004). Correlation maps allow neuronal electrical properties to be predicted from single-cell gene expression profiles in rat neocortex. *Cerebral Cortex*, 14(12):1310–1327. (Cited on page 48.)

Toyoizumi, T., Kaneko, M., Stryker, M. P., and Miller, K. D. (2014). Modeling the dynamic interaction of hebbian and homeostatic plasticity. *Neuron*, 84(2):497–510. (Cited on pages 83 and 102.)

Tozer, A. J., Forsythe, I. D., and Steinert, J. R. (2012). Nitric oxide signalling augments neuronal voltage-gated l-type (ca (v) 1) and p/q-type (ca (v) 2.1) channels in the mouse medial nucleus of the trapezoid body. *PloS one*, 7(2). (Cited on pages 7, 17, and 18.)

Trattner, B., Gravot, C. M., Grothe, B., and Kunz, L. (2013). Metabolic maturation of auditory neurones in the superior olivary complex. (Cited on page 37.)

Traub, R. D., Wong, R., Miles, R., and Michelson, H. (1991). A model of a ca3 hippocampal pyramidal neuron incorporating voltage-clamp data on intrinsic conductances. *Journal of Neurophysiology*, 66(2):635–650. (Cited on page 49.)

Triesch, J. (2007). Synergies between intrinsic and synaptic plasticity mechanisms. *Neural Comput*, 19(4):885–909. (Cited on page 12.)

Trimmer, J. S. and Rhodes, K. J. (2004). Localization of voltage-gated ion channels in mammalian brain. *Annu. Rev. Physiol.*, 66:477–519. (Cited on page 49.)

Tripathy, S. J., Padmanabhan, K., Gerkin, R. C., and Urban, N. N. (2013). Intermediate intrinsic diversity enhances neural population coding. *P Natl Acad Sci USA*, 110(20):8248–53. (Cited on pages 13, 52, 78, and 102.)

Turrigiano, G. (2011). Too many cooks? intrinsic and synaptic homeostatic mechanisms in cortical circuit refinement. *Annual review of neuroscience*, 34:89–103. (Cited on pages 2, 7, 8, and 13.)

Turrigiano, G., Abbott, L., and Marder, E. (1994). Activity-dependent changes in the intrinsic properties of cultured neurons. *Science-AAAS-Weekly Paper Edition-including Guide to Scientific Information*, 264(5161):974–976. (Cited on pages 5, 6, and 10.)

Turrigiano, G. G., Leslie, K. R., Desai, N. S., Rutherford, L. C., and Nelson, S. B. (1998). Activity-dependent scaling of quantal amplitude in neocortical neurons. *Nature*, 391(6670):892–896. (Cited on page 4.)

Turrigiano, G. G. and Nelson, S. B. (2004). Homeostatic plasticity in the developing nervous system. *Nature Reviews Neuroscience*, 5(2):97–107. (Cited on pages 1, 2, and 4.)

Uhlenbeck, G. E. and Ornstein, L. S. (1930). On the theory of the brownian motion. *Phys Rev*, 36(5):823. (Cited on page 53.)

Vacher, H. and Trimmer, J. S. (2012). Trafficking mechanisms underlying neuronal voltage-gated ion channel localization at the axon initial segment. *Epilepsia*, 53(s9):21–31. (Cited on page 18.)

Van Der Walt, S., Colbert, S. C., and Varoquaux, G. (2011). The numpy array: a structure for efficient numerical computation. *Comput Sci Eng*, 13(2):22–30. (Cited on pages 27, 46, and 61.)

Van Geit, W., De Schutter, E., and Achard, P. (2008). Automated neuron model optimization techniques: a review. *Biological cybernetics*, 99(4-5):241–251. (Cited on page 26.)

Van Rossum, M. C., Bi, G. Q., and Turrigiano, G. G. (2000). Stable hebbian learning from spike timing-dependent plasticity. *J Neurosci*, 20(23):8812–8821. (Cited on pages 82, 86, and 98.)

Vogels, T., Sprekeler, H., Zenke, F., Clopath, C., and Gerstner, W. (2011). Inhibitory plasticity balances excitation and inhibition in sensory pathways and memory networks. *Science*, 334(6062):1569–1573. (Cited on pages 12 and 83.)

Vogels, T. P. and Abbott, L. F. (2005). Signal propagation and logic gating in networks of integrate-and-fire neurons. *The Journal of neuroscience*, 25(46):10786–10795. (Cited on page 85.)

von Gersdorff, H. and Borst, J. G. G. (2002). Short-term plasticity at the calyx of held. *Nature Reviews Neuroscience*, 3(1):53–64. (Cited on pages 24 and 101.)

Wang, L., Gan, L., Forsythe, I. D., and Kaczmarek, L. K. (1998). Contribution of the kv3.1 potassium channel to high frequency firing in mouse auditory neurones. *The Journal of Physiology*. (Cited on pages 17, 19, 20, 22, and 31.)

Wang, R. (2002). Two's company, three's a crowd: can H2S be the third endogenous gaseous transmitter? *FASEB J*, 16(13):1792–1798. (Cited on page 80.)

Watt, A. J. and Desai, N. S. (2010). Homeostatic plasticity and stdp: keeping a neuron's cool in a fluctuating world. *Frontiers in synaptic neuroscience*, 2. (Cited on page 13.)

Weiser, M., Bueno, E., Sekirnjak, C., Martone, M., Baker, H., Hillman, D., Chen, S., Thornhill, W., Ellisman, M., and Rudy, B. (1995). The potassium channel subunit kv3. 1b is localized to somatic and axonal membranes of specific populations of cns neurons. *The Journal of neuroscience*, 15(6):4298–4314. (Cited on page 49.)

Weitzdoerfer, R., Hoeger, H., Engidawork, E., Engelmann, M., Singewald, N., Lubec, G., and Lubec, B. (2004). Neuronal nitric oxide synthase knock-out mice show impaired cognitive performance. *Nitric Oxide*, 10(3):130–140. (Cited on page 79.)

Williams, A. H., O'Leary, T., and Marder, E. (2013). Homeostatic regulation of neuronal excitability. *Scholarpedia*, 8(1):1656. (Cited on pages 1, 2, 5, and 7.)

Wixted, J. T. and Ebbesen, E. B. (1991). On the form of forgetting. *Psychological science*, 2(6):409–415. (Cited on page 94.)

Wixted, J. T. and Ebbesen, E. B. (1997). Genuine power curves in forgetting: A quantitative analysis of individual subject forgetting functions. *Memory & cognition*, 25(5):731–739. (Cited on page 94.)

Wohrer, A., Humphries, M., and Machens, C. (2013). Population-wide distributions of neural activity during perceptual decision-making. *Prog Neurobiol*, 103:156–193. (Cited on pages 52, 62, 75, 76, and 100.)

Wright, M. H. (1996). Direct search methods: Once scorned, now respectable. *Pitman Research Notes in Mathematics Series*, pages 191–208. (Cited on pages 27 and 46.)

Wu, S. H. and Kelly, J. B. (1993). Response of neurons in the lateral superior olive and medial nucleus of the trapezoid body to repetitive stimulation: intracellular and extracellular recordings from mouse brain slice. *Hearing research*, 68(2):189–201. (Cited on page 17.)

Xiao, L., Michalski, N., Kronander, E., Gjoni, E., Genoud, C., Knott, G., and Schneggenburger, R. (2013). Bmp signaling specifies the development of a large and fast cns synapse. *Nature neuroscience*, 16(7):856–864. (Cited on page 15.)

Yamada, K. and Inagaki, N. (2005). Neuroprotection by k atp channels. *Journal of molecular and cellular cardiology*, 38(6):945–949. (Cited on page 101.)

Yavuz, E., Turner, J., and Nowotny, T. (2014). Simulating spiking neural networks on massively parallel graphical processing units using a code generation approach with genn. *BMC Neuroscience*, 15(1):1. (Cited on page 88.)

Yu, Y., Shu, Y., and McCormick, D. A. (2008). Cortical action potential backpropagation explains spike threshold variability and rapid-onset kinetics. *The Journal of Neuroscience*, 28(29):7260–7272. (Cited on page 24.)

Zenke, F., Agnes, E. J., and Gerstner, W. (2015). Diverse synaptic plasticity mechanisms orchestrated to form and retrieve memories in spiking neural networks. *Nature communications*, 6. (Cited on pages 12 and 103.)

Zenke, F., Hennequin, G., and Gerstner, W. (2013). Synaptic plasticity in neural networks needs homeostasis with a fast rate detector. *PLoS Comput Biol*, 9(11):e1003330. (Cited on pages 12, 52, 76, and 83.)

Zhigulin, V. P., Rabinovich, M. I., Huerta, R., and Abarbanel, H. D. (2003). Robustness and enhancement of neural synchronization by activity-dependent coupling. *Physical Review E*, 67(2):021901. (Cited on page 82.)

Ziegler, L., Zenke, F., Kastner, D. B., and Gerstner, W. (2015). Synaptic consolidation: from synapses to behavioral modeling. *The Journal of Neuroscience*, 35(3):1319–1334. (Cited on page 103.)

COLOPHON

This document was typeset using the typographical look-and-feel `classicthesis` developed by André Miede. The style was inspired by Robert Bringhurst's seminal book on typography "*The Elements of Typographic Style*". `classicthesis` is available for both LaTeX and LyX:

`http://code.google.com/p/classicthesis/`

Happy users of `classicthesis` usually send a real postcard to the author, a collection of postcards received so far is featured here:

`http://postcards.miede.de/`

Final Version as of 25th May 2016 (`classicthesis` version 4.0).